

University of New Hampshire

University of New Hampshire Scholars' Repository

Doctoral Dissertations

Student Scholarship

Winter 1995

Experiments on transient natural convection in inclined enclosures using calibrated multichannel electronic interferometry and digital particle image velocimetry

Timothy David Upton

University of New Hampshire, Durham

Follow this and additional works at: <https://scholars.unh.edu/dissertation>

Recommended Citation

Upton, Timothy David, "Experiments on transient natural convection in inclined enclosures using calibrated multichannel electronic interferometry and digital particle image velocimetry" (1995). *Doctoral Dissertations*. 1879.

<https://scholars.unh.edu/dissertation/1879>

This Dissertation is brought to you for free and open access by the Student Scholarship at University of New Hampshire Scholars' Repository. It has been accepted for inclusion in Doctoral Dissertations by an authorized administrator of University of New Hampshire Scholars' Repository. For more information, please contact Scholarly.Communication@unh.edu.

INFORMATION TO USERS

This manuscript has been reproduced from the microfilm master. UMI films the text directly from the original or copy submitted. Thus, some thesis and dissertation copies are in typewriter face, while others may be from any type of computer printer.

The quality of this reproduction is dependent upon the quality of the copy submitted. Broken or indistinct print, colored or poor quality illustrations and photographs, print bleedthrough, substandard margins, and improper alignment can adversely affect reproduction.

In the unlikely event that the author did not send UMI a complete manuscript and there are missing pages, these will be noted. Also, if unauthorized copyright material had to be removed, a note will indicate the deletion.

Oversize materials (e.g., maps, drawings, charts) are reproduced by sectioning the original, beginning at the upper left-hand corner and continuing from left to right in equal sections with small overlaps. Each original is also photographed in one exposure and is included in reduced form at the back of the book.

Photographs included in the original manuscript have been reproduced xerographically in this copy. Higher quality 6" x 9" black and white photographic prints are available for any photographs or illustrations appearing in this copy for an additional charge. Contact UMI directly to order.

UMI

A Bell & Howell Information Company
300 North Zeeb Road, Ann Arbor, MI 48106-1346 USA
313:761-4700 800:521-0600

**EXPERIMENTS ON TRANSIENT NATURAL CONVECTION IN INCLINED
ENCLOSURES USING CALIBRATED MULTICHANNEL ELECTRONIC
INTERFEROMETRY AND DIGITAL PARTICLE IMAGE VELOCIMETRY**

by

Timothy David Upton
Bachelor of Science, University of New Hampshire, 1989

DISSERTATION

Submitted to the University of New Hampshire
in partial fulfillment of the requirements for the degree of

Doctor of Philosophy

in

Engineering

December, 1995

UMI Number: 9617078

UMI Microform 9617078
Copyright 1996, by UMI Company. All rights reserved.

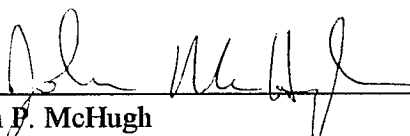
**This microform edition is protected against unauthorized
copying under Title 17, United States Code.**

UMI
300 North Zeeb Road
Ann Arbor, MI 48103

This dissertation has been examined and approved.



Dissertation Director, David W. Watt
Associate Professor of Mechanical Engineering



John P. McHugh
Associate Professor of Mechanical Engineering



John A. Wilson
Associate Professor of Mechanical Engineering



Dale P. Barkey
Associate Professor of Chemical Engineering



Allen D. Drake
Associate Professor of Electrical Engineering



Date

**A spirit with a vision is a dream with a mission.
Neil Peart, RUSH**

ACKNOWLEDGEMENTS

To Professor David W. Watt for his special blend of motivation, enthusiasm, skepticism, and support. We have worked together for so long that our relationship has the flavor of an old married couple. This work was funded in part by the Mavis Foster Research Fellowship.

TABLE OF CONTENTS

DEDICATION	iii
ACKNOWLEDGEMENTS	iv
LIST OF TABLES	viii
LIST OF FIGURES	ix
ABSTRACT	xi
CHAPTER	PAGE
I INTRODUCTION	1
1.1 Overview	1
1.2 Calibrated multichannel electronic interferometry	2
1.3 Digital particle image velocimetry	2
1.4 Transient natural convection in inclined enclosures	3
II CALIBRATED MULTICHANNEL ELECTRONIC INTERFEROMETRY	4
2.1 Optical flow visualization	4
2.2 Interferometry	5
2.2.1 Phase shifting	6
2.2.2 Multichannel phase shifting	7
2.3 Calibrated multichannel phase shifting	9
2.3.1 Optical design	10

2.3.2 Alignment	16
2.3.3 Calibration	21
2.3.4 Phase computation	25
2.4 Experiment	27
2.5 Conclusions	29
References	31
III DIGITAL PARTICLE IMAGE VELOCIMETRY	33
3.1 Spatial correlation techniques	33
3.2 Speckle photography	33
3.3 Digital particle image velocimetry	35
3.3.1 Optical design	38
3.3.2 Timing signals	39
3.3.3 Particle size	39
3.4 Conclusions	47
References	47
IV TRANSIENT NATURAL CONVECTION IN INCLINED ENCLOSURES	49
4.1 Transient natural convection in enclosures	49
4.1.1 Previous work	50
4.1.2 Classification	51
4.1.3 Transient and periodic oscillations	52
4.1.4 Problem description	56
4.1.5 Scale analysis	59

4.2 Simultaneous quantitative measurements of both the temperature and velocity fields	63
4.2.1 Experimental design	64
4.2.2 Analysis	68
4.2.3 Results and discussion	74
4.3 Conclusions	97
4.4 Future work	97
References	98
LIST OF REFERENCES	101

LIST OF TABLES

TABLE	PAGE
4.1 Time and length scales estimated by scaling and experiment.	91

LIST OF FIGURES

FIGURE	PAGE
2.1 Schematic of a calibrated multichannel electronic interferometer.	10
2.2 Optimum distance from the gratings to the camera.	12
2.3 Displacement of the diffracted orders in a flat beamsplitter.	13
2.4 Imaging using a negative meniscus lens.	15
2.5 Displacement of the diffracted orders for a misaligned beam.	17
2.6 Common types of misalignment determined using spatial crosscorrelation with $2 \times$ magnification in the Fourier domain: (a) a one pixel error both in the pixel correspondence and in the alignment of the diffraction plane, (b) a one pixel error in the pixel correspondence, (c) a one pixel error in the alignment of the diffraction plane, (d) a well aligned beam.	20
2.7 Calibration of multichannel electronic interferometer: (a) phase, (b) modulation, (c) bias.	24
2.8 Typical multichannel interferogram.	27
2.9 Sequential phase maps of transient buoyant thermal plume.	28
2.10 Unwrapped phase of plume shown in Fig. 2.9.	29
2.11 Sequential phase maps with phase errors.	30
3.1 Velocity determined using spatial crosscorrelation with $2 \times$ magnification in the Fourier domain: (a) particle image, (b) particle image Δt later, (c) crosscorrelation, (d) velocity vector.	37
3.2 Schematic of a digital particle image velocimeter.	38

3.3	Timing signals for a VHS video cassette recorder: (a) timing signal, (b) recorded signal, (c) amplifier circuit, (d) output signal.	40
3.4	Timing signals for a Hi8 video cassette recorder: (a) timing signal, (b) recorded signal, (c) amplifier circuit, (d) output signal.	41
3.5	Approximation of Airy distribution using Gaussian function.	42
4.1	Geometry of two-dimensional inclined rectangular enclosure.	57
4.2	Two-layer flow structure	60
4.3	Schematic of the simultaneous implementation of a calibrated multichannel electronic interferometer and a digital particle image velocimeter.	64
4.4	Schematic of the natural convection enclosure.	65
4.5	Schematic of the temperature difference measurement system.	67
4.6	Temperature and velocity fields during the evolution of the flow to steady state for $\gamma=\pi/4$: (a) $t=10$ s, (b) $t=22$ s, (c) $t=40$ s, (d) $t=75$ s, (e) $t=600$ s.	75
4.7	Temperature and velocity fields during the evolution of the flow to steady state for $\gamma=\pi/2$: (a) $t=10$ s, (b) $t=22$ s, (c) $t=40$ s, (d) $t=75$ s, (e) $t=600$ s.	80
4.8	Temperature and velocity fields during the evolution of the flow to steady state for $\gamma=3\pi/4$: (a) $t=10$ s, (b) $t=22$ s, (c) $t=40$ s, (d) $t=75$ s, (e) $t=600$ s.	85
4.9	(a) Temperature in the boundary layer and (b) Nusselt number at the wall and center of the enclosure for $\gamma=\pi/4$.	93
4.10	(a) Temperature in the boundary layer and (b) Nusselt number at the wall and center of the enclosure for $\gamma=\pi/2$.	94
4.11	(a) Temperature in the boundary layer and (b) Nusselt number at the wall and center of the enclosure for $\gamma=3\pi/4$.	95

ABSTRACT

EXPERIMENTS ON TRANSIENT NATURAL CONVECTION IN INCLINED ENCLOSURES USING CALIBRATED MULTICHANNEL ELECTRONIC INTERFEROMETRY AND DIGITAL PARTICLE IMAGE VELOCIMETRY

by

Timothy David Upton
University of New Hampshire, December, 1995

Simultaneous quantitative measurements are made of both the temperature and velocity fields for two-dimensional transient natural convection in an inclined rectangular enclosure. The fluid in the enclosure is initially stationary and isothermal. The transient boundary conditions are initiated by instantaneously heating and cooling two opposing walls. All other walls are insulated and nonconducting. The evolution of the flow to steady state is determined for a Prandtl number of 6.38, a Rayleigh number of 1.5×10^5 , and an aspect ratio of 1.0, at angles of inclination of $\pi/4$, $\pi/2$, and $3\pi/4$. The temperature is measured using calibrated multichannel electronic interferometry, and the velocity is measured using digital particle image velocimetry. This allows accurate measurement of the temperature and velocity fields throughout the enclosure and visualization of the boundary layers, intrusion layers, and recirculation zones. The angle of inclination is shown to have a significant effect on the flow and heat transfer. However, the expected transient oscillations are not evident. This is probably due to differences in the boundary conditions at startup between the current experiments and the numerical simulations.

CHAPTER I

INTRODUCTION

1.1 Overview

This work is a study of transient natural convection in inclined enclosures. To accomplish this a system is implemented to perform time resolved experimental measurements of transient temperature and velocity fields. This system consists of two optical techniques, calibrated multichannel electronic interferometry (CMEI) and digital particle image velocimetry (DPIV). In Chapter II the development of the new technique of CMEI is discussed. CMEI is an interferometric technique used for measuring transient temperature fields. In Chapter III the implementation of DPIV is addressed. DPIV is a correlation technique used for measuring velocity fields. In Chapter IV transient natural convection in inclined enclosures is discussed. The results in Chapter IV include simultaneous quantitative measurements made using CMEI and DPIV of both the temperature and velocity fields for two-dimensional transient natural convection in an inclined rectangular enclosure.

1.2 Calibrated multichannel electronic interferometry

CMEI is an interferometric technique which uses multichannel phase shifting for time resolution of transient temperature fields. In standard phase shifting the three phase-shifted interferograms necessary to determine the interferometric phase are acquired over time, limiting standard phase shifting to steady phenomena. In multichannel phase shifting the phase-shifted interferograms are produced simultaneously using diffraction gratings. However, several problems result from the separation of the three phase-shifted interferograms used in multichannel phase shifting. These problems render multichannel phase shifting nearly unusable. In CMEI described in the present work calibration and alignment techniques are used to correct for these errors and make multichannel phase shifting viable. The development of CMEI comprises a major portion of this research.

1.3 Digital particle image velocimetry

DPIV is a correlation technique for whole field velocity measurement. Light is scattered from seed particles added to the fluid, and two sequential particle images are recorded. The displacement of the particles between the two images is determined using the spatial crosscorrelation. It is not a true instantaneous technique, but as the time between the two particle images becomes small, the measured velocity approaches the instantaneous velocity.

1.4 Transient natural convection in inclined enclosures

Natural convection in enclosures has applications in many fields including architectural, environmental, and solar energy engineering. In many of these applications the enclosures are inclined to the direction of gravity, so that buoyancy forces have both normal and tangential components relative to the walls, and the boundary conditions change with time, so that the convective flow is transient. These flows exhibit a number of interesting features including startup vortices, transient oscillations, and multiple cell structures.

Simultaneous quantitative measurements are made of both the temperature and velocity fields for two-dimensional transient natural convection in an inclined rectangular enclosure. The fluid in the enclosure is initially stationary and isothermal. The transient boundary conditions are initiated impulsively by heating and cooling two opposing walls. The other two walls are insulated and nonconducting. The evolution of the flow to steady state is determined for a Prandtl number of 6.38, a Rayleigh number of 1.5×10^5 , and an aspect ratio of 1.0, at angles of inclination of $\pi/4$, $\pi/2$, and $3\pi/4$. The angle of inclination is shown to have a significant effect on the flow and heat transfer. However, the expected transient oscillations are not evident.

CHAPTER II

CALIBRATED MULTICHANNEL ELECTRONIC INTERFEROMETRY

2.1 Optical flow visualization

Changes in the physical properties of transparent objects such as the density and temperature of fluids are related to variation of the refractive index defined by

$$n = \frac{c_0}{c} , \quad (2.1)$$

where c_0 is the speed of light in a vacuum and c is the speed of light in the material.

Variation of the refractive index is the basis for shadowgraph, schlieren, and interferometric flow visualization techniques. The shadowgraph and schlieren methods are single beam techniques based on ray bending and are sensitive to changes in the second and first derivatives of the refractive index respectively (Merzkirch 1987). Interferometric methods depend on a phase delay or advance of the light and are sensitive to variation of the refractive index directly. Interferometric methods measure the optical path differences between two interfering wavefronts. Each interference fringe in the resulting interferogram corresponds to an optical path difference equal to one wavelength of light (Vest 1979).

2.2 Interferometry

In Mach-Zehnder interferometry the two wavefronts are separated in space. Ideally, the two paths will be identical with no phase object present, and the interferogram will be of uniform irradiance. When a phase object is present in one of the paths, the interferogram will give a quantitative measure of the refractive index field in the object. The phase difference between the two paths is

$$\Delta \Theta(x,y) = \frac{2\pi}{\lambda_0} \int [n(x,y) - n_0] ds \quad (2.2)$$

(Vest 1979), where λ_0 is the wavelength of the light, $n(x, y)$ is the refractive index field in the phase object path, n_0 is the refractive index in the reference path, and s is the path of integration through the phase object. Imperfections in or misalignment of the optical elements will cause the two paths to differ and will be evident as extraneous fringes in the interferogram. These extraneous fringes are avoided by using holographic interferometry.

In holographic interferometry the two wavefronts are separated in time; both beams traverse the same physical space (Vest 1979). When a phase object is present in one of the paths, the phase object wavefront is compared to that recreated by the hologram. The resulting interferogram is sensitive only to the refractive index changes in the phase object. Any other differences in the wavefront will exist in both the reconstructed and the phase object wavefronts and will not be evident as interference fringes.

An important advance in holographic interferometry is electro-optic holographic

interferometry. In electro-optic holography the phase information is stored electronically instead of holographically. A typical setup is a standard Mach-Zehnder interferometer where the phase is determined with no phase object present using piezoelectric phase shifting. This phase map is stored as an image file. If a phase map is calculated at a later time with a phase object present, the phase disturbance due to the phase object itself can be found by subtracting the two phase maps (Stetson et al. 1989; Raber 1991).

2.2.1 Phase shifting

Phase shifting is an augmentation technique for interferometry which allows the interferometric phase to be determined directly from a set of three or more phase-shifted interferograms (Hariharan 1985). The irradiance pattern in an interferogram (Vest 1979) is given by

$$I(x, y) = a(x, y) \{1 + m(x, y) \cos[\Theta(x, y)]\} \quad (2.3)$$

where $\Theta(x, y)$ is the interferometric phase, $a(x, y)$ is the bias, and $m(x, y)$ is the modulation. If the phase difference between the interfering wavefronts is changed by shifting the phase of one of the wavefronts, the equation becomes

$$I_i(x, y) = a(x, y) \{1 + m(x, y) \cos[\Theta(x, y) + \Psi_i]\} \quad (2.4)$$

(Jüptner et al. 1983), where Ψ_i is the phase shift. To solve Eq. (2.4) three phase-shifted interferograms of known phase shift are necessary (Jüptner et al. 1983; Creath 1988).

Phase shifting has been demonstrated for a number of interferometric applications including flow visualization (Watt and Vest 1987; Lanen et al. 1990).

The advantages of this technique include increasing the accuracy by a factor of ten over standard interferometry, eliminating the phase sign ambiguity, and automating determination of the absolute phase. The phase-shifted interferograms are typically produced using a piezoelectric transducer that shifts the phase of one of the interfering wavefronts. Since this process occurs over time, piezoelectric phase shifting is limited to steady phenomena or double-exposure pulsed-laser holographic interferometry (Watt and Vest 1987; Lanen et al. 1990).

2.2.2 Multichannel phase shifting

For time resolution of transient phenomena the phase-shifted interferograms have to exist simultaneously. A technique called multichannel holographic interferometry that has been developed to do this uses the -1, 0, and +1 orders of a diffraction grating to produce the phase-shifted interferograms (Shough and Kwon 1987; Kujawińska and Robinson 1988). If only these orders are considered, the amplitude transmittance of a sinusoidal phase grating (Vest 1979) is given by

$$t(y) = J_0\left(\frac{M}{2}\right) + J_1\left(\frac{M}{2}\right) e^{i(2\pi f_g y + \Psi)} + J_1\left(\frac{M}{2}\right) e^{-i(2\pi f_g y + \Psi - \pi)}, \quad (2.5)$$

where J_n is the Bessel function of the first kind of order n , M is the phase modulation depth, f_g is the spatial frequency of the grating, and Ψ is the phase offset of the grating.

The diffracted orders are phase shifted by the amount of relative phase offset between the phase object wavefront and the reconstructed wavefront. The relative phase offset is changed by translating the grating in the diffraction plane and is of the form

$$\Delta \Psi = 2\pi f_g \Delta y , \quad (2.6)$$

where Δy is the relative translation of the grating. When the hologram is reconstructed, the grating is translated in the diffraction plane by a fraction of the grating period. This introduces a negative phase shift into the -1 order and a positive phase shift into the +1 order relative to the original phase. The three phase-shifted interferograms produced by the diffraction grating are used to perform phase shifting in the same way as the three discretely phase-shifted interferograms used in standard phase shifting.

Several problems particular to multichannel holographic interferometry result from the separation of the three diffracted orders, both in the optics and on the detector. There is also the additional complication of aligning the three diffracted orders so that a pixel to pixel correspondence exists between the three interferograms. None of these problems exist for piezoelectric phase shifting, since the three phase-shifted interferograms are shifted in time rather than space. The use of high quality optical elements and detectors and special hologram development techniques reduces these errors but does not eliminate them. A better way is to evaluate the errors and account for them in the phase computation.

Previous implementations of multichannel interferometers have been expensive and error prone. One technique developed uses a separate camera, frame grabber, and frame

buffer for each interferometric channel. The three frame grabbers have to be customized to synchronize the three cameras (Shough and Kwon 1987). For accurate results the modulation and bias are required to be the same for corresponding pixels of each diffracted order (Kujawińska and Robinson 1988). This requires that the grating diffraction efficiency for the -1, 0, and +1 orders be equal, that the three diffracted orders be separated on the hologram and that the hologram be exposed and developed uniformly for equal hologram diffraction efficiency, and that the camera or cameras have identical response for corresponding pixels. Additionally, the translation of the grating to introduce the desired phase shift has to be highly accurate (Kujawińska, et al. 1989). To introduce a phase shift of $2\pi/3$, the grating has to be moved $1/3$ of a grating period. For a grating with 400 lines per millimeter the translation required is $0.833 \mu\text{m}$. Until now the additional errors in multichannel holographic interferometry have been quantified but not accounted for (Kujawińska and Robinson 1988).

2.3 Calibrated multichannel phase shifting

In the technique of calibrated multichannel electronic interferometry (CMEI) described in the present work, standard piezoelectric phase shifting is used to compensate for the aforementioned errors. In CMEI the phase, modulation, and bias are determined for the optical system with no phase object present. These values are stored electronically and used to correct the interferograms and perform phase shifting with a phase object present.

2.3.1 Optical design

The basic layout of a multichannel electronic interferometer is that of a Mach-Zehnder interferometer (Fig. 2.1). The laser beam is split into an object beam and a reference beam. The object beam is expanded and collimated to illuminate the test section and then is reduced and collimated for image acquisition. The reference beam is expanded and collimated. Diffraction gratings are

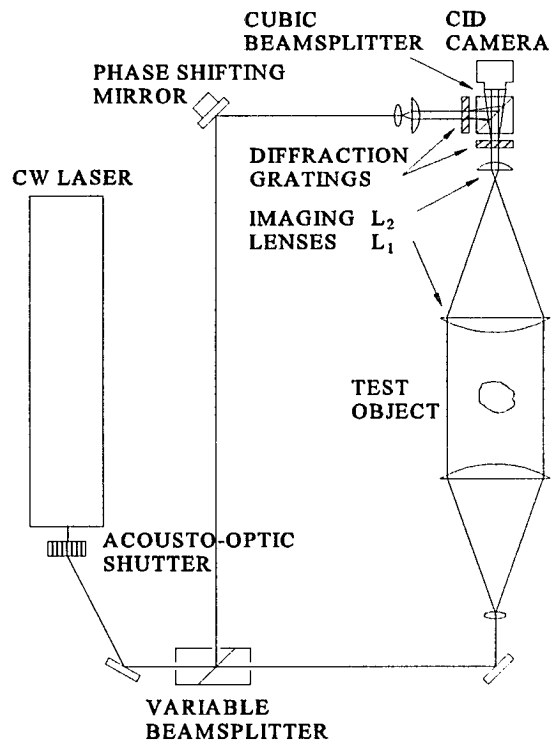


Fig. 2.1 Schematic of a calibrated multichannel electronic interferometer.

located in both beams to produce the three phase-shifted interferograms. These beams are then combined and imaged directly on to the camera.

The interferograms are acquired using a CID Technologies Incorporated CID2250E2 solid state charge injection device camera controlled using a CID Technologies Incorporated ICM7000F interface control module. The advanced features of this camera include frame reset, inject inhibit, charge dump, and rapid scan. These allow multiple frame exposure for low amplitude events, snapshot capture for transient events, asynchronous camera reset to coordinate timing with an event, and region of interest windowing for higher frame rates. The usable camera area is 505 pixels \times 505

pixels. Each pixel measures $15 \mu\text{m} \times 15 \mu\text{m}$. This results in a usable camera area of $2.5 \text{ mm} \times 7.5 \text{ mm}$ for each diffracted order. The interferograms are stored using an Imaging Technology Incorporated VS-100-AT frame grabber capable of storing four images of $512 \text{ pixels} \times 512 \text{ pixels}$. A Siemens 40 mW helium-neon continuous wave laser with a wavelength of 632.8 nm is used to produce the interferograms. The laser is shuttered using an NEC Corporation acousto-optic modulator. Both the laser shutter and the camera reset are controlled by a MetraByte Corporation Dascon-1 digital-analog expansion board. The laser beam is split using a Newport Corporation 930-63 variable beamsplitter. Both beams are expanded and spatially filtered. A mirror mounted on a Burleigh Instrumentation PZ-81 linear piezoelectric transducer is located in the reference beam. The piezoelectric transducer is controlled using the Dascon-1 board and a Kepco NTC 2000 power supply.

Spectrogon diffraction gratings measuring $25 \text{ mm} \times 25 \text{ mm}$ are located in both the object and the reference beams. The diffraction grating located in the reference beam is mounted on a single axis translation stage to change the relative phase offset of the gratings as shown in Eq. (2.6). The diffraction gratings have a spatial frequency of 150 mm^{-1} and are designed so that the -1, 0, and +1 orders are of equal amplitude $\pm 5\%$. For an aligned beam the diffraction angle is given by

$$\alpha_k = \sin^{-1}(k\lambda f_g) , \quad (2.7)$$

where k is the diffracted order and λ is the wavelength of light. A $25 \text{ mm} \times 25 \text{ mm}$ 50/50 prism cube beamsplitter made from BK-7 is used to recombine the beams. The diffraction

angle and the physical and optical properties of the beamsplitter are used to determine the optimum distance from the gratings to the camera for an aligned beam. By use of Snell's law and geometry the optimum grating distance is determined by

$$z_g = \frac{w_c - z_{bs} \tan[\sin^{-1}(\frac{n_{air}}{n_{bs}} \sin(\alpha_1))]}{\tan(\alpha_1)} + z_{bs} , \quad (2.8)$$

where w_c is the usable camera width for each diffracted order, z_{bs} is the thickness of the beamsplitter, n_{air} is the refractive index of air, and n_{bs} is the refractive index of the beamsplitter (Fig. 2.2).

Since the diffracted orders propagate in different directions, refraction and optical path length differences prohibit using standard

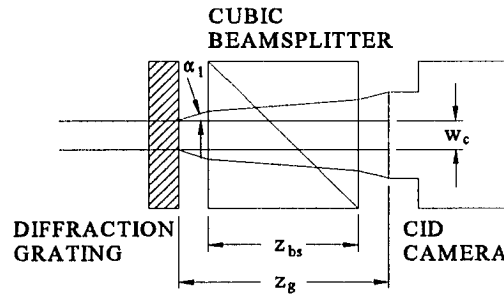


Fig. 2.2 Optimum distance from the gratings to the camera.

flat beamsplitters. These beamsplitters are coated on one side resulting in a different number of passes through the beamsplitter for each beam. For this reason the diffracted orders of one beam are displaced relative to the diffracted orders of the other beam. The displacement of the diffracted orders caused by refraction is

$$d_k = z_{bs} \{ \cos(\angle_k) \tan[\sin^{-1}(\frac{n_{air}}{n_{bs}} \sin(\angle_k))] - \sin(\angle_k) \} , \quad (2.9)$$

where \angle_k depends on the orientation of the diffraction plane and is determined by either

$$\angle_k = \angle_{bs} + \alpha_k \quad (2.10)$$

or

$$\angle_k = \cos^{-1}[\cos(\angle_{bs})\cos(\alpha_k)] , \quad (2.11)$$

where \angle_{bs} is the angle of the beamsplitter (Fig. 2.3). Since the diffracted orders pass through at different angles, the optical path length is different for each order,

introducing a phase error term. The optical path difference of the diffracted orders is

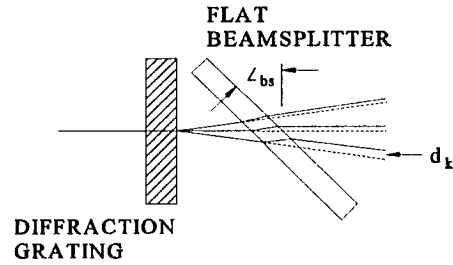


Fig. 2.3 Displacement of the diffracted orders in a flat beamsplitter.

$$OPD = \frac{n_{bs} z_{bs}}{\cos[\sin^{-1}(\frac{n_{air}}{n_{bs}} \sin(\angle_k))]} - \frac{n_{air} z_{bs}}{\cos(\angle_k)} \quad (2.12)$$

The important criteria for the selection of object beam lenses are the location of the image plane of the lens system and the size of the final image (Hecht and Zajac 1979). Both the object and the reference beams are collimated when they pass through the diffraction gratings and beamsplitter to the camera to minimize aberrations caused by refraction and interference fringes caused by mismatched wavefront curvature. Since a collimated beam enters and exits the imaging lenses, the distance between the lenses is

equal to the sum of their focal lengths. For this configuration the image distance from the second imaging lens is

$$s_{i2} = f_2 \left(1 + \frac{f_2}{f_1} \right) - \frac{f_2^2}{f_1^2} s_{o1} , \quad (2.13)$$

where f_1 is the focal length of the first imaging lens, f_2 is the focal length of the second imaging lens, and s_{o1} is the object distance from the first imaging lens. For the interferograms to be in focus on the camera, the image produced by the second imaging lens has to be real. This limits the object distance from the first imaging lens to

$$s_{o1} < f_1 \left(1 + \frac{f_1}{f_2} \right) . \quad (2.14)$$

For this configuration the transverse magnification is

$$M_T = -\frac{f_2}{f_1} . \quad (2.15)$$

The necessary magnification is determined by

$$M_T = \frac{w_c}{w_t} , \quad (2.16)$$

where w_t is the width of the test object. This results in a focal length ratio of

$$\frac{f_2}{f_1} = \frac{w_c}{w_t} . \quad (2.17)$$

The minimum object distance from the first imaging lens is determined by the test object dimensions. The minimum distance between the image plane of the lens system and the

second imaging lens is determined by the optimum grating distance using Eq. (2.8) and the grating and the lens mount dimensions. The minimum values for the focal lengths of the lenses are then found using Eqs. (2.13) and (2.17), subject to the condition of Eq. (2.14). Typically longer focal lengths are selected to minimize wavefront distortion.

Matched plano-convex or achromatic lenses are used in the object beam to minimize wavefront distortion. A more complex system is necessary if the optical table is not long enough to obtain the desired

magnification. To use matched lenses of shorter focal length a negative meniscus lens is added in the object path after the first imaging lens

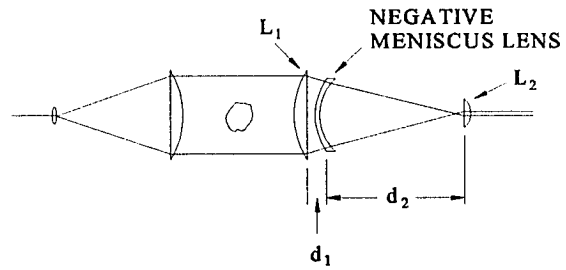


(Fig. 2.4). For a collimated beam to enter and exit the imaging lenses, the

Fig. 2.4 Imaging using a negative meniscus lens.

distance between the meniscus lens and the second imaging lens is

$$d_2 = \frac{f_m (d_1 - f_1)}{d_1 - f_1 - f_m} + f_2, \quad (2.18)$$

where f_m is the focal length of the meniscus lens and d_1 is the distance between the first imaging lens and the meniscus lens, and the image distance from the second imaging lens is

$$s_{i2} = f_2 \left[1 + \frac{f_2 (d_1 - f_1 - f_m) (d_1 - f_m)}{f_1 f_m^2} \right] - \frac{f_2^2 (d_1 - f_1 - f_m)^2}{f_1^2 f_m^2} s_{o1}. \quad (2.19)$$

To produce a real image on the camera, the object distance from the first imaging lens is limited to

$$s_{o1} < \frac{f_1^2 f_m^2 + f_1 f_2 (d_1 - f_1 - f_m)(d_1 - f_m)}{f_2 (d_1 - f_1 - f_m)^2} . \quad (2.20)$$

Additionally this system allows variable magnification by changing the distance between the first imaging lens and the meniscus lens. The magnification of this three lens system is

$$M_T = \frac{f_2 (d_1 - f_1 - f_m)}{f_1 f_m} . \quad (2.21)$$

2.3.2 Alignment

The critical alignments in a multichannel electronic interferometer are the orientation of the diffraction gratings, the cubic beamsplitter, and the camera, and the orientations of the object and the reference beams relative to these components. For a misaligned beam the diffraction angle is given by

$$\alpha_k = \sin^{-1}[k\lambda f_g + \sin(\delta_{in})] - \delta_{in} , \quad (2.22)$$

where δ_{in} is the angle of misalignment in the diffraction plane. For a misaligned beam the displacement of the diffracted orders caused by refraction in the cubic beamsplitter is

$$d_k = z_{bs} \{ \cos(\angle_k) \tan[\sin^{-1}(\frac{n_{ar}}{n_{bs}} \sin(\angle_k))] - \sin(\angle_k) \} , \quad (2.23)$$

where \angle_k is determined by

$$\angle_k = \cos^{-1}[\cos(\alpha_k + \delta_{in})\cos(\delta_{out})] , \quad (2.24)$$

where δ_{out} is the angle of misalignment out of the diffraction plane (Fig. 2.5). The optical path difference of the diffracted orders is

$$OPD = n_{air} \left[\frac{z_g - z_{bs}}{\cos(\angle_k)} - \frac{z_g - z_{bs}}{\cos(\alpha_k)} \right] + n_{bs} \left\{ \frac{z_{bs}}{\cos[\sin^{-1}(\frac{n_{air}}{n_{bs}}\sin(\angle_k))]} - \frac{z_{bs}}{\cos[\sin^{-1}(\frac{n_{air}}{n_{bs}}\sin(\alpha_k))]} \right\} . \quad (2.25)$$

Misalignment of either the diffraction gratings or the cubic beamsplitter relative to each other or to the object and the reference beams results in phase shift and pixel correspondence errors. Pixel correspondence errors

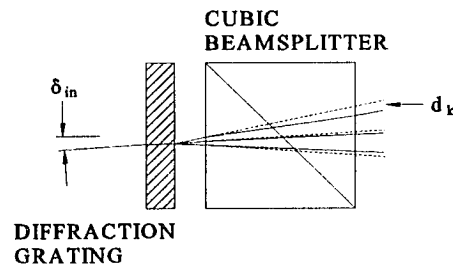


Fig. 2.5 Displacement of the diffracted orders for a misaligned beam.

result from the unequal separation of the diffracted orders as shown in Eqs. (2.22) and (2.23) and from misalignment of the camera. The unequal separation of the diffracted orders also causes phase shift errors, since different regions of the object and the reference wavefront are interfering in each diffracted order. Additional phase shift errors result from the optical path difference between the corresponding diffracted orders of the object and the reference beams as shown in Eq. (2.25).

The initial alignment consists of establishing an alignment plane. This plane is determined by the object and the reference beams at the cubic beamsplitter. The

diffraction gratings, cubic beamsplitter, and camera are oriented relative to this plane. The object and the reference beams are aligned so that the alignment plane is typically horizontal and the beams are perpendicular at the cubic beamsplitter. The cubic beamsplitter is positioned at the intersection of the object and the reference beams so that it bisects the angle between the beams. Each diffraction grating is positioned so that the beam is normal to its surface and the diffraction plane typically lies in the alignment plane. The camera is positioned so that an axis of the detector lies in the alignment plane and the combined beams are normal to the detector.

The alignment accuracy is determined computationally using the technique of spatial crosscorrelation. The two-dimensional crosscorrelation (Bracewell 1965; Goodman 1968) is given by

$$c_{fg}(X, Y) = \int_{-\infty}^{\infty} \int_{-\infty}^{\infty} f^*(x, y) g(x+X, y+Y) dx dy , \quad (2.26)$$

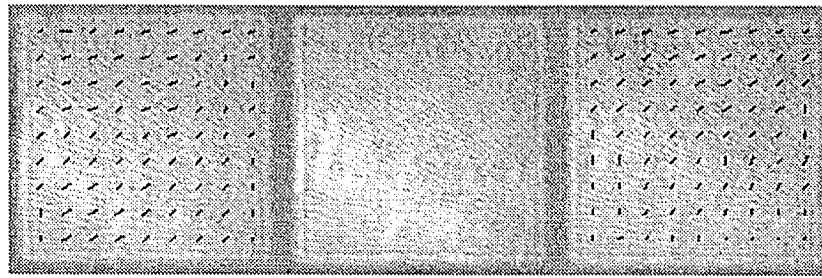
where $f(x, y)$ and $g(x, y)$ are the spatial functions and X and Y are the spatial displacements between the two functions. The maximum value of the crosscorrelation represents the best match between the two functions. By use of the Fourier transform the equation becomes

$$c_{fg}(X, Y) = \mathcal{F}^{-1}[F^*(k_x, k_y) G(k_x, k_y)] , \quad (2.27)$$

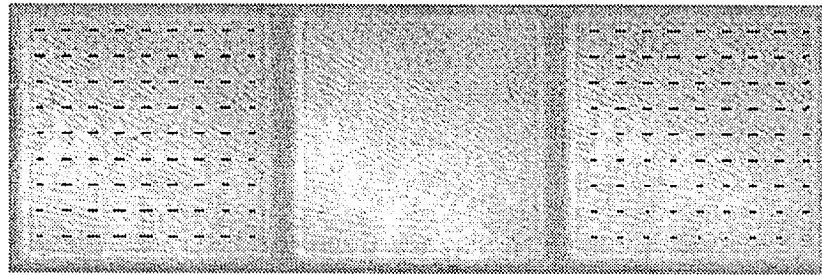
where \mathcal{F}^{-1} denotes the inverse Fourier transform and $F^*(k_x, k_y)$ and $G(k_x, k_y)$ are the Fourier transforms of $f^*(x, y)$ and $g(x, y)$ respectively. The crosscorrelation is determined

numerically using a two-dimensional fast Fourier transform method. Subpixel accuracy is possible with magnification in the Fourier domain. To obtain subpixel accuracy, additional frequency components are added to the Fourier transform product shown in Eq. (2.27) and set to 0. The resulting crosscorrelation is then sampled at subpixel intervals.

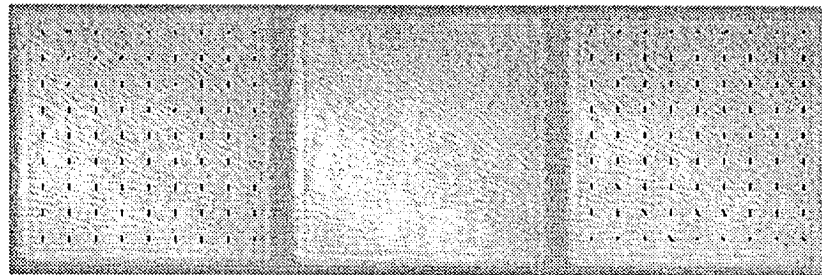
The pixel correspondence between the diffracted orders is determined using an adjustment routine that sets the starting location of the 0 order and an equal displacement to corresponding locations on the -1 and +1 orders. The crosscorrelations between the 0 and the -1 orders and between the 0 and the +1 orders are then determined to indicate the displacement of the -1 and the +1 orders relative to the 0 order. The crosscorrelations of the diffracted orders of the object and the reference beams are determined separately. Arrows are drawn on the -1 and +1 orders by the crosscorrelation routine, and these indicate the direction of misalignment. This misalignment is caused either by the orientation of the diffraction gratings, the cubic beamsplitter, or the camera, or by the determined pixel correspondence. Two common types of misalignment are shown in Fig. 2.6. The misalignment shown in Fig. 2.6(a) indicates a one pixel error both in the displacement used for the pixel correspondence and in the alignment of the diffraction plane. The misalignment shown in Fig. 2.6(b) indicates a one pixel error in the displacement used for the pixel correspondence, while that shown in Fig. 2.6(c) indicates a one pixel error in the alignment of the diffraction plane. A well aligned beam is indicated in Fig. 2.6(d). The crosscorrelations shown were performed with $2 \times$ magnification in the Fourier domain.



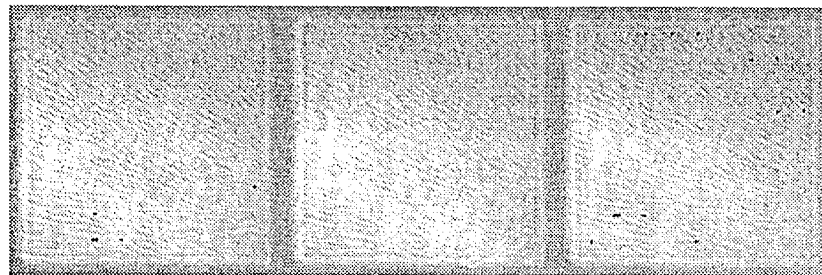
(a)



(b)



(c)



(d)

Fig. 2.6 Common types of misalignment determined using spatial crosscorrelation with $2 \times$ magnification in the Fourier domain: (a) a one pixel error both in the pixel correspondence and in the alignment of the diffraction plane, (b) a one pixel error in the pixel correspondence, (c) a one pixel error in the alignment of the diffraction plane, (d) a well aligned beam.

2.3.3 Calibration

The linear piezoelectric transducer is calibrated by incrementing the controller voltage and measuring the irradiance at a location of high modulation in the 0 order. The phase of one of the interfering wavefronts is shifted by several wavelengths of light to increase accuracy. The phase shift voltage is determined by

$$V_{\Psi} = \frac{\Psi}{2\pi} V_{2\pi} , \quad (2.28)$$

where $V_{2\pi}$ is the voltage required to shift the phase by one wavelength of light. This is found by determining the voltages where the measured irradiance crosses the average irradiance. To account for noise in the irradiance data, a noise threshold is used to determine the crossing voltages accurately. The optimum phase shift (Brophy 1990) is found using

$$\Psi = \frac{(N-1)}{N} \pi , \quad (2.29)$$

where N is the number of phase-shifted interferograms.

The multichannel electronic interferometer is calibrated using piezoelectric phase shifting. To reduce errors associated with the determination of the phase shift, it is left as an unknown in Eq. (2.2) (Dändliker et al. 1982; Schwider et al. 1983; Creath 1988; Brophy 1990). For a linear piezoelectric transducer with a constant but unknown phase shift, Eq. (2.4) is written as

$$I_1(x,y) = a(x,y) \{1 + m(x,y) \cos[\Theta(x,y)]\} , \quad (2.30)$$

$$I_2(x,y) = a(x,y) \{1 + m(x,y) \cos[\Theta(x,y) + \Psi]\} , \quad (2.31)$$

$$I_3(x,y) = a(x,y) \{1 + m(x,y) \cos[\Theta(x,y) + 2\Psi]\} , \quad (2.32)$$

and

$$I_4(x,y) = a(x,y) \{1 + m(x,y) \cos[\Theta(x,y) + 3\Psi]\} \quad (2.33)$$

(Jüptner et al. 1983). Eqs. (2.30), (2.31), (2.32), and (2.33) are solved for the phase shift by

$$\Psi = \cos^{-1} \left[\frac{(I_4 - I_1) - (I_3 - I_2)}{2(I_3 - I_2)} \right] . \quad (2.34)$$

Eqs. (2.30), (2.31), and (2.32) are solved for the phase by

$$\Theta(x,y) = \tan^{-1} \left\{ \frac{[\cos(\Psi) - 1] \{ [2 \cos(\Psi) + 1] I_1 - [2 \cos(\Psi) + 2] I_2 + I_3 \}}{\sqrt{1 - \cos^2(\Psi)} \{ [2 \cos(\Psi) - 1] I_1 - [2 \cos(\Psi)] I_2 + I_3 \}} \right\} \quad (2.35)$$

using Eq. (2.34). Eqs. (2.30) and (2.31) are solved for the modulation by

$$a(x,y) m(x,y) = \frac{I_2 - I_1}{[\cos(\Psi) - 1] \cos(\Theta) - \sin(\Psi) \sin(\Theta)} \quad (2.36)$$

using Eqs. (2.34) and (2.35). Eqs. (2.31) and (2.32) are solved for the modulation by

$$a(x,y)m(x,y) = \frac{I_3 - I_2}{[\cos(\Psi) - 1][2\cos(\Psi) + 1]\cos(\Theta) - \sin(\Psi)[2\cos(\Psi) + 1]\sin(\Theta)} \quad (2.37)$$

using Eqs. (2.34) and (2.35). Eq. (2.30) is solved for the bias by

$$a(x,y) = I_1 - am \cos(\Theta) \quad (2.38)$$

using Eqs. (2.35), (2.36), and (2.37).

During calibration four piezoelectric phase-shifted interferograms are recorded. The phase shift at each pixel is determined using Eq. (2.34). Since the phase shift is uniform over the three diffracted orders, the average of the phase shift at each pixel is used for the phase shift. The phase shift at pixels where $I_3 - I_2$ is less than the maximum irradiance noise is not included in the average. The optical system is calibrated using Eqs. (2.35), (2.36), (2.37), and (2.38). The phase at each pixel is determined using Eq. (2.35). The modulation at each pixel is determined using Eqs. (2.36) and (2.37). At pixels where $I_3 - I_2$ is less than the maximum irradiance noise, the modulation is determined using Eq. (2.36). At pixels where $I_2 - I_1$ is less than the maximum irradiance noise, the modulation is determined using Eq. (2.37). At the remaining pixels the modulation is the average determined using Eqs. (2.36) and (2.37). The bias at each pixel is determined using Eq. (2.38). The phase, modulation, and bias are stored (Fig 2.7). The phase shown in Fig. 2.7(a) indicates the phase shift between the diffracted orders. Modulation and bias differences between the diffracted orders are shown in Figs. 2.7(b) and 2.7(c) respectively.

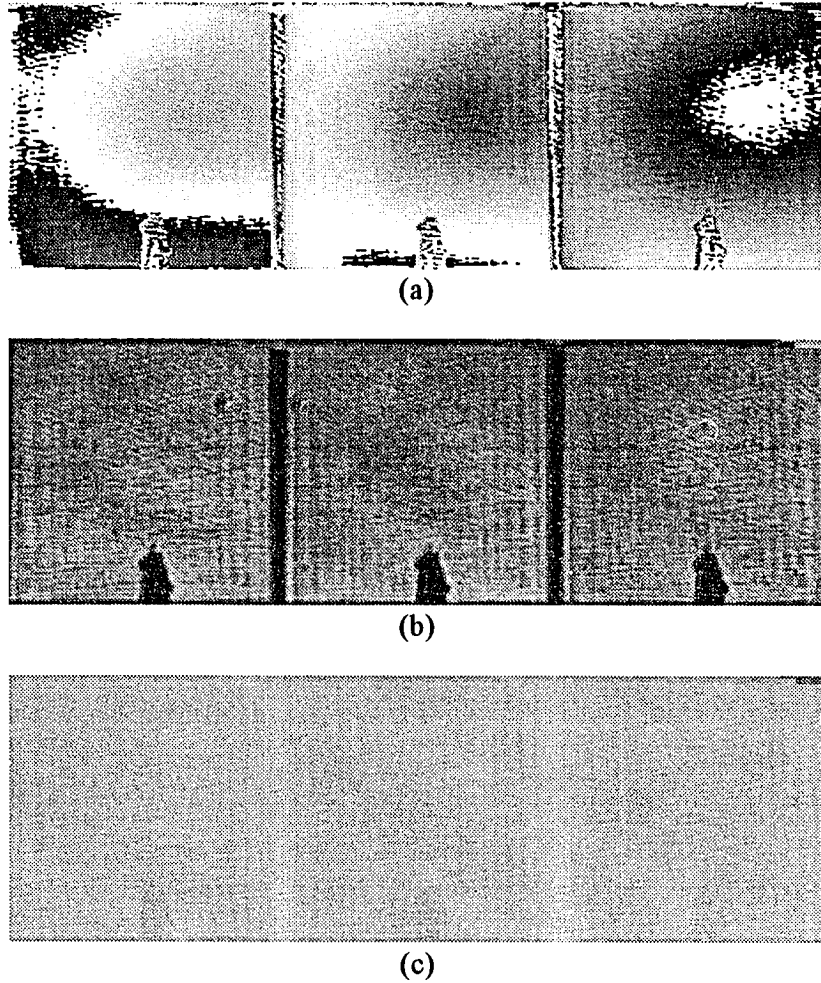


Fig. 2.7 Calibration of multichannel electronic interferometer: (a) phase, (b) modulation, (c) bias.

The phase determined during calibration of the optical system is used for the phase shift in the multichannel phase computation. The accuracy of the multichannel phase computation depends on the magnitude of the phase shift. Since the phase shift is actually measured, the translation of the grating is not critical as long as the interferograms are phase shifted by a large enough amount to minimize truncation errors and to obtain a relatively high signal to noise ratio. The accuracy of the multichannel phase computation

is determined using an error routine which calculates the no flow phase and the minimum phase shift between any two of the diffracted orders. Ideally the relative phase offset of the gratings is $2\pi/3$, shifting the phase of the -1 order by $-2\pi/3$ and the +1 order by $+2\pi/3$ relative to the 0 order. However, the phase shift is not typically this large due to inaccurate translation of the grating, misalignment, and differential aberration between the three diffracted orders.

By use of this calibration technique, the errors associated with the separation of the diffracted orders are measured and corrected. These include variation in grating diffraction efficiency and detector response. An important aspect of this technique is that wavefront errors on the order of 1/10 of a wavelength in the diffraction gratings, beamsplitter, and camera are accounted for and do not cause errors in the final phase computation.

2.3.4 Phase computation

After the multichannel electronic interferometer is calibrated, the desired experiment is run, and a time sequence of interferograms is recorded and stored. The phase for three known but arbitrary phase shifts (Dändliker and Thalman 1985) is given by

$$\Theta(x,y) = \tan^{-1} \left[\frac{(I_2 - I_3)\cos(\Psi_1) + (I_3 - I_1)\cos(\Psi_2) + (I_1 - I_2)\cos(\Psi_3)}{(I_2 - I_3)\sin(\Psi_1) + (I_3 - I_1)\sin(\Psi_2) + (I_1 - I_2)\sin(\Psi_3)} \right] . \quad (2.39)$$

The modulation and bias are considered to be the same for each phase-shifted

interferogram in the derivation of Eq. (2.39). This is accurate for piezoelectric phase shifting in which the phase-shifted interferograms are not shifted in space. To account for modulation and bias differences between the diffracted orders used in multichannel phase shifting, the phase is given by

$$\Theta(x,y) = \tan^{-1} \quad (2.40)$$

$$\left\{ \frac{[\frac{a_1 m_1}{a_1} (\frac{I_2}{a_2} - \frac{I_3}{a_3})] \cos(\Psi_1) + [\frac{a_2 m_2}{a_2} (\frac{I_3}{a_3} - \frac{I_1}{a_1})] \cos(\Psi_2) + [\frac{a_3 m_3}{a_3} (\frac{I_1}{a_1} - \frac{I_2}{a_2})] \cos(\Psi_3)}{[\frac{a_1 m_1}{a_1} (\frac{I_2}{a_2} - \frac{I_3}{a_3})] \sin(\Psi_1) + [\frac{a_2 m_2}{a_2} (\frac{I_3}{a_3} - \frac{I_1}{a_1})] \sin(\Psi_2) + [\frac{a_3 m_3}{a_3} (\frac{I_1}{a_1} - \frac{I_2}{a_2})] \sin(\Psi_3)} \right\},$$

where the subscripts refer to the -1, 0, and +1 orders.

Typically variation in the phase shift between the diffracted orders is on the order of $\pm\pi/10$, and variations in the modulation and bias between the diffracted orders are on the order of $\pm 5\%$. Without calibration the uncertainties in the phase shift, modulation, and bias are equal to these undetermined variations, resulting in an uncertainty (Holman 1989) in the phase of $\pm\pi/13$. With calibration the uncertainties in the phase shift, modulation, and bias depend on the accuracy of the piezoelectric phase shifting. If only the phase shift is determined, the uncertainty in the phase is reduced to $\pm\pi/37$ with an accurate calibration. If the phase shift, modulation, and bias are determined, the uncertainty in the phase is eliminated with an accurate calibration.

A benefit of multichannel interferometry is that it is less influenced by environmental changes such as thermal perturbations, mechanical instabilities, and illumination drift than standard phase-shifted holographic interferometry where the phase-

shifted interferograms are acquired over time (Kujawinska and Robinson 1988).

However, since in CMEI the optical system is calibrated with piezoelectric phase shifting, any errors present in the calibration will be carried through into each real time phase computation.

2.4 Experiment

The technique was used to study the transient behavior of a two-dimensional buoyant thermal plume at start up. The plume was created in air using a resistance heated wire 50 mm long with a diameter of 0.2 mm. The camera was used in asynchronous capture mode with an acquisition window of 168 lines, yielding a maximum frame rate of 82 Hz. Each diffracted order on the camera is 168 pixels \times 168 pixels, allowing a maximum of twelve multichannel interferograms to be stored by the frame grabber. Each of these multichannel interferograms consists of three phase-shifted interferograms (Fig. 2.8). Ten multichannel

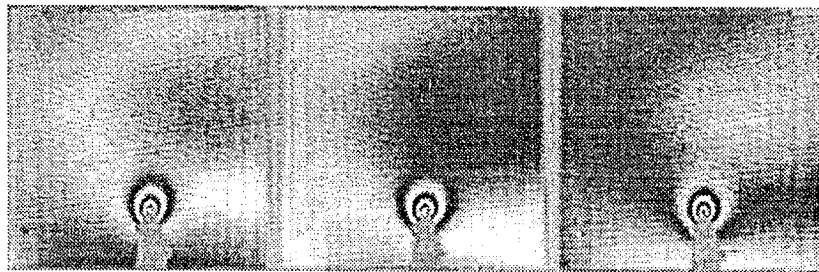


Fig. 2.8 Typical multichannel interferogram.

interferograms were captured beginning at start up with a time interval of 0.15 s using a 40 μ s exposure. The phase maps are shown in Fig. 2.9, and the unwrapped maps are shown in Fig. 2.10. These clearly show the development of the plume and the transition

from radial conduction to convection as the air accelerates due to buoyancy.

Three errors that caused phase errors in the results of previous experiments (Fig. 2.11) are eliminated. Phase errors caused by interferogram defocusing are eliminated by locating the test object to form a real image and determining the image plane. Interlacing errors are eliminated by suspending readout during camera exposure. Pixel correspondence errors are eliminated by accurate determination of the displacements between the diffracted orders and subsequent realignment if necessary. In previous results shown in Fig. 2.11 these phase errors are apparent as breaks in the fringe boundaries in regions of large phase gradients. These phase errors are not

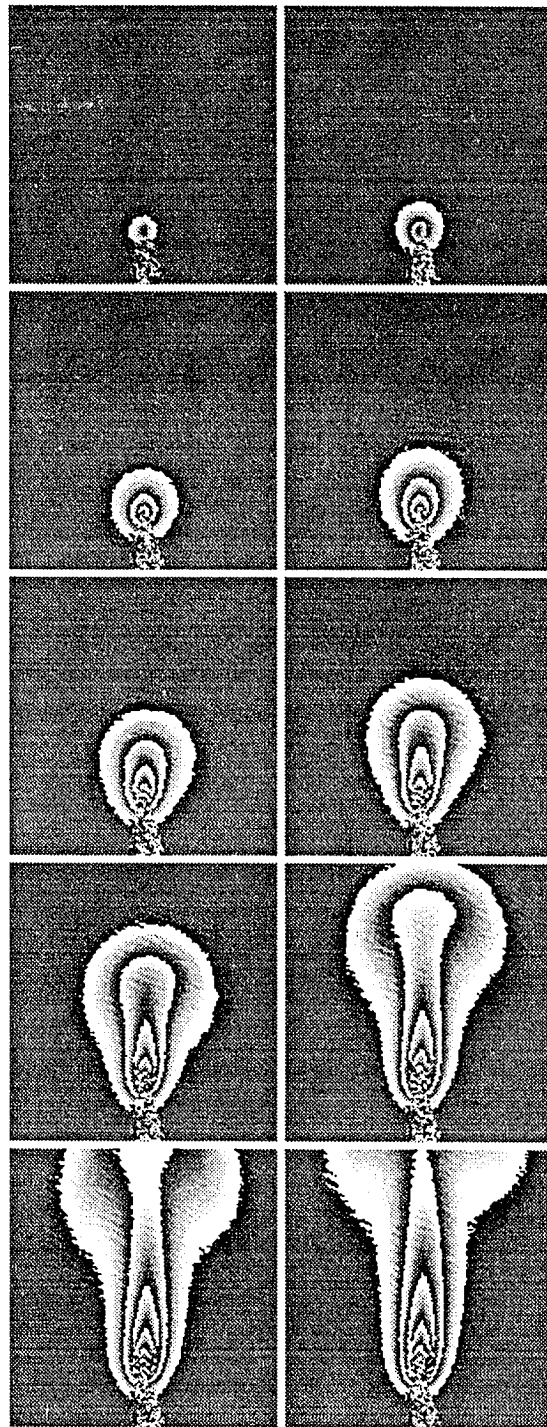


Fig. 2.9 Sequential phase maps of transient buoyant thermal plume.

apparent in the current results (Fig. 2.9).

2.5 Conclusions

The optical and electronic design of a system for CMEI has been discussed. System improvements in the optical setup and the alignment determination have shown to result in more accurate phase computations. These improvements include correct imaging of the phase object, entire frame exposure, and accurate alignment using the crosscorrelations between the diffracted orders.

Multichannel phase shifting has a number of potential applications. It can be used for time resolution of slow flows, which can be resolved at video rate, and applications in which repetitive

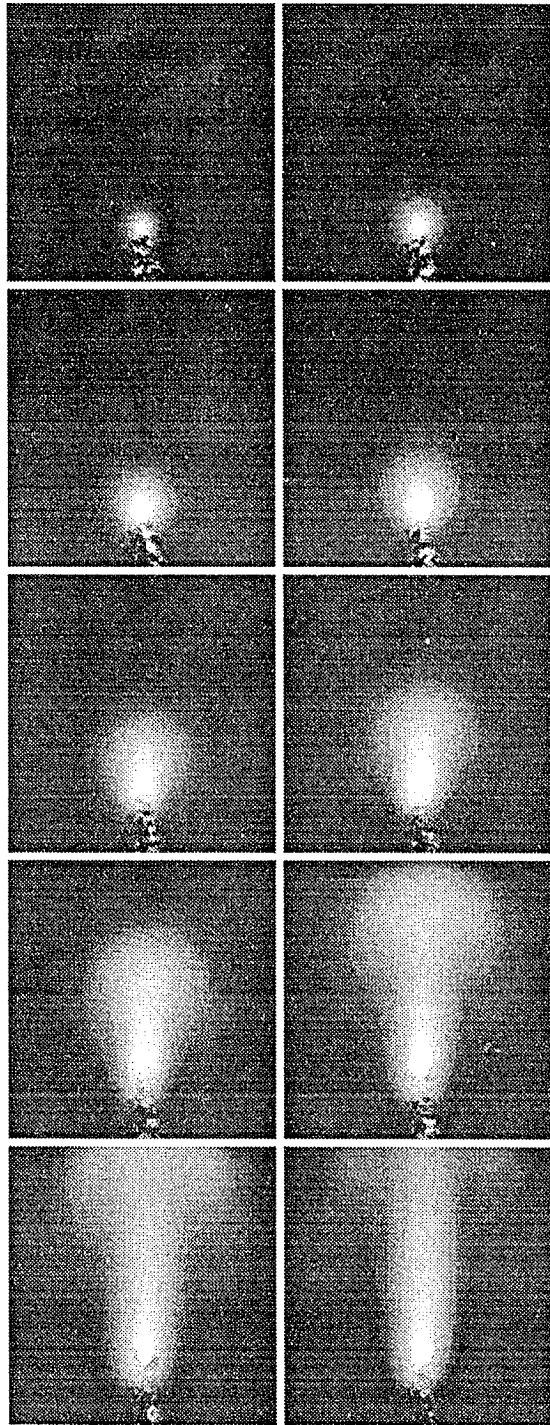


Fig. 2.10 Unwrapped phase of plume shown in Fig. 2.9.

interferograms are required. The technique also has advantages over fringe injection holographic methods (Takeda et al. 1982; Snyder 1988), since no hologram is required, the required computation time is less, and the spatial resolution has no inherent limit. The technique can also potentially be used with pulsed lasers as an alternative to double exposure holographic interferometry.

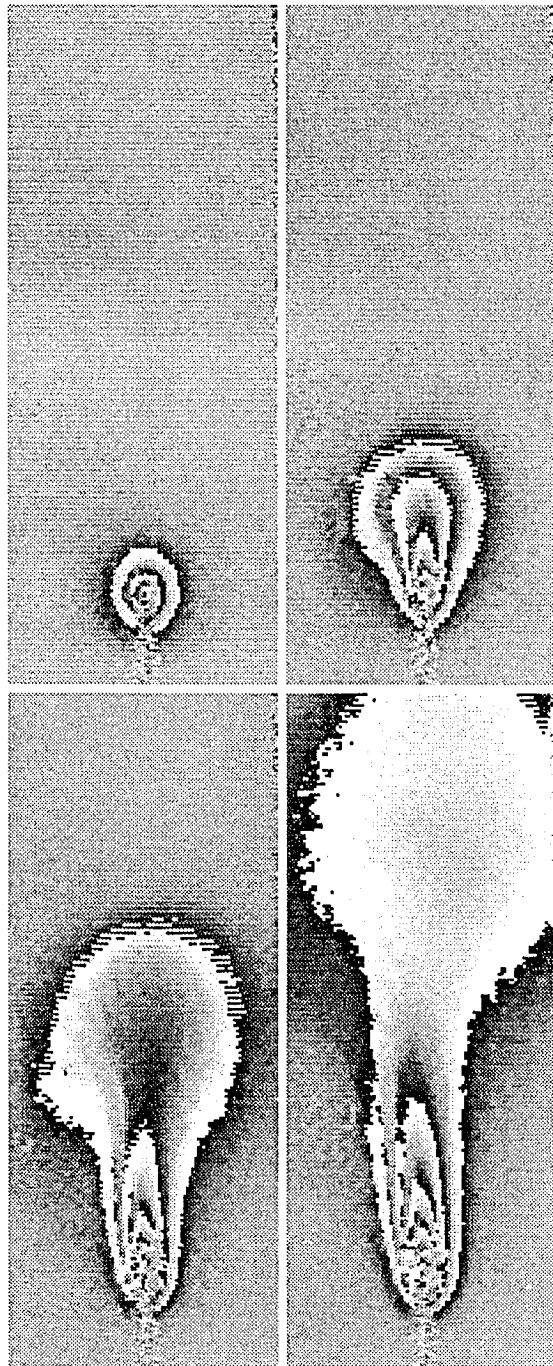


Fig. 2.11 Sequential phase maps with phase errors.

References

- Bracewell, R. 1965: *The Fourier Transform and Its Applications*. New York: McGraw-Hill, 24-48.
- Brophy, C. P. 1990: Effect of intensity error correlation on the computed phase of phase-shifting interferometry. *J. Opt. Soc. Am. A* **7**, 537-541.
- Creath, K. 1988: Phase-measurement interferometry techniques. *Prog. Opt.* **26**, 349-393.
- Dändliker, R.; Thalmann, R.; Willemin, J. -F. 1982: Fringe interpolation by two-reference-beam holographic interferometry: reducing sensitivity to hologram misalignment. *Opt. Comm.* **42**, 301-306.
- Dändliker, R.; Thalmann, R. 1985: Heterodyne and quasi-heterodyne holographic interferometry. *Opt. Eng.* **24**, 824-831.
- Goodman, J. W. 1968: *Introduction to Fourier Optics*. New York: McGraw-Hill, 4-25.
- Hariharan, P. 1985: Quasi-heterodyne holographic interferometry. *Opt. Eng.* **24**, 632-638.
- Hecht, E.; Zajac, A. 1974: *Optics*. Reading MA: Addison-Wesley, 109-116.
- Holman, J. P. 1989: *Experimental Methods for Engineers*. New York: McGraw-Hill, 41-49.
- Jüptner, W.; Kreis, T. M.; Kreitlow, H. 1983: Automatic evaluation of holographic interferograms by reference beam phase shifting. In *Industrial Applications of Laser Technology* (ed. W. F. Fagan). *Proc. Soc. Photo-Opt. Instrum. Eng.* **398**, 22-29.
- Kujawińska, M.; Robinson, D. W. 1988: Multichannel phase-stepped holographic interferometry. *Appl. Opt.* **27**, 312-320.
- Kujawińska, M.; Spik, A.; Robinson, D. W. 1989: Quantitative analysis of transient events by ESPI. In *Interferometry '89* (eds. Z. Jaroszewicz; M. Pluta). *Proc. Soc. Photo-Opt. Instrum. Eng.* **1121**, 416-423.
- Lanen, T. A. W. M.; Nebbeling, C.; van Ingen, J. L. 1990: Digital phase-stepping holographic interferometry in measuring 2-D density fields. *Exp. Fluids* **9**, 231-235.
- Merzkirch, W. 1987: *Flow Visualization*. New York: Academic Press, 115-231.

- Raber, R. S. 1991: Electro-optic interferometry with noise tolerant phase unwrapping. M.S. Thesis, Department of Mechanical Engineering, The University of New Hampshire, Durham/NH.
- Schwider, J.; Burow, R.; Elssner, K. -E.; Grzanna, J.; Spolaczyk, R.; Merkel, K. 1983: Digital wave-front measuring interferometry: some systematic error sources. *Appl. Opt.* **22**, 3421-3432.
- Shough, D. M.; Kwon, O. Y. 1987: Phase-shifting pulsed-laser interferometer. In *Phase Conjugation, Beam Combining, and Diagnostics* (eds. I. Abramowitz; R. A. Fisher). *Proc. Soc. Photo-Opt. Instrum. Eng.* **739**, 174-180.
- Snyder, R. 1988: Instantaneous three-dimensional optical tomographic measurements of species concentration in a co-flowing jet. Ph.D. Thesis, Department of Aeronautics and Astronautics, Stanford University, Stanford/CA.
- Stetson, K. A.; Brohinsky, W. R.; Wahid, J.; Bushman, T. 1989: Electro-optic holography system with real-time arithmetic processing. *J. Nondestr. Eval.* **8**, 69-76.
- Takeda, M.; Ina, H.; Kobayashi, S. 1982: Fourier-transform method of fringe-pattern analysis for computer-based tomography and interferometry. *J. Opt. Soc. Am.* **72**, 156-160.
- Vest, C. M. 1979: *Holographic Interferometry*. New York: John Wiley and Sons, 264-284.
- Watt, D. W.; Vest, C. M. 1987: Digital interferometry for flow visualization. *Exp. Fluids* **5**, 401-406.

CHAPTER III

DIGITAL PARTICLE IMAGE VELOCIMETRY

3.1 Spatial correlation techniques

Measurement by optical correlation is the basis of speckle photography, laser speckle velocimetry, and particle image velocimetry. These methods involve double exposure photographic recording and optical processing of the double exposed images to determine the displacement of either the speckle patterns or the particle images. In digital particle image velocimetry (DPIV) two images are recorded digitally, and the crosscorrelation is determined computationally (Willert and Gharib 1991).

3.2 Speckle photography

Speckle photography is a technique for measuring two-dimensional strain and displacement of solid objects (Vest 1979). The object is illuminated with laser light, and the photographic film is exposed both before and after the object is displaced. The developed film contains two speckle patterns separated by a distance related to the displacement of the object. The object displacement is typically determined by

illuminating a small region of the film with an unexpanded laser beam. Each speckle pair contributes to the formation of Young's fringes. The spacing of these fringes is

$$d_f(x,y) = \frac{\lambda z_f}{d_s(x,y)} \quad (3.1)$$

(Vest 1979), where λ is the wavelength of the light, z_f is the distance from the film to the image plane, and $d_s(x, y)$ is the speckle displacement. The speckle displacement is

$$d_s(x,y) = M_T d(x,y) , \quad (3.2)$$

where M_T is the transverse magnification of the imaging system used to record the two speckle patterns and $d(x, y)$ is the object displacement. The magnitude of the object displacement in the illuminated region is then given by

$$d(x,y) = \frac{\lambda z_f}{M_T d_f(x,y)} . \quad (3.3)$$

The direction of the object displacement is perpendicular to the direction of the fringes.

The technique of speckle photography has been extended to fluid velocity field measurement and is called laser speckle velocimetry (Grousseau and Mallick 1977; Barker and Fournery 1977; Dudderar and Simpkins 1977). The plane of interest is illuminated with a sheet of laser light. The light is scattered from seed particles added to the fluid and is imaged perpendicular to the laser sheet. The film is exposed twice to contain the two displaced speckle patterns. The film is analyzed in the same way as for solid objects. The average fluid velocity between the two exposures is given by

$$u(x,y) = \frac{d(x,y)}{\Delta t} \quad (3.4)$$

(Adrian 1991b), where Δt is the time between exposures. As the time between exposures becomes smaller, the average velocity approaches the instantaneous velocity.

For speckle patterns to exist on the film, the particle concentration must be high enough for many images to overlap with random phase (Adrian 1984). Particle concentrations this high are not always practical, and instead of speckle patterns, diffraction limited images of individual particles are recorded on the film. Advantages of the particle image mode include decreased seeding concentration and increased tolerance to three dimensional motion. In the laser speckle mode three dimensional motion results in different speckle patterns on the film, which do not add constructively to produce Young's fringes when illuminated with a laser beam. In the particle image mode the tolerance to three dimensional motion is approximately equal to the thickness of the laser sheet and the depth of field of the imaging system (Lourenco and Krothapalli 1987). However, in the particle image mode there are regions where there are no velocity data, since there are regions in the fluid where no particles exist (Adrian and Yao 1985).

3.3 Digital particle image velocimetry

Determination of the velocity field in either laser speckle velocimetry or particle image velocimetry requires extensive processing. Additionally, the minimum recoverable velocity is limited by the separation of the particles on the film, and image shifting is

required to determine the sign of the velocity (Adrian 1986). The technique of DPIV resolves many of the problems associated with laser speckle velocimetry and particle image velocimetry (Willert and Gharib 1991). In this technique two separate single exposure particle images are recorded digitally.

The velocity is determined computationally using the technique of spatial crosscorrelation (Willert and Gharib 1991). The two-dimensional crosscorrelation (Bracewell 1965; Goodman 1968) is given by

$$c_{fg}(X, Y) = \int_{-\infty}^{\infty} \int_{-\infty}^{\infty} f^*(x, y) g(x+X, y+Y) dx dy , \quad (3.5)$$

where $f(x, y)$ and $g(x, y)$ are the spatial functions and X and Y are the spatial displacements between the two functions. The maximum value of the crosscorrelation represents the best match between the two functions. By use of the Fourier transform the equation becomes

$$c_{fg}(X, Y) = \mathcal{F}^{-1}[F^*(k_x, k_y)G(k_x, k_y)] , \quad (3.6)$$

where \mathcal{F}^{-1} denotes the inverse Fourier transform and $F^*(k_x, k_y)$ and $G(k_x, k_y)$ are the Fourier transforms of $f^*(x, y)$ and $g(x, y)$ respectively. The crosscorrelation is determined numerically using a two-dimensional fast Fourier transform method. Subpixel accuracy is possible with magnification in the Fourier domain. To obtain subpixel accuracy, additional frequency components are added to the Fourier transform product shown in Eq. (3.6) and set to 0. The resulting crosscorrelation is then sampled at subpixel intervals.

The crosscorrelation and resulting velocity vector between two typical particle images are shown in Fig. 3.1. The particle images are 32 pixels \times 32 pixels, and the crosscorrelation was performed with 2 \times magnification in the Fourier domain. The crosscorrelation coefficient is calculated using

$$cc_{fg}(X, Y) = \frac{c_{fg}(X, Y)}{c_{fg}(0, 0)}, \quad (3.7)$$

where the value of the crosscorrelation coefficient is between 0 and 1. Typically velocity data are rejected where the crosscorrelation coefficient is less than a minimum acceptable value. DPIV has been used to study a low Reynolds number vortex ring (Willert and Gharib 1991), a premixed turbulent flame and a pulsed air jet (Lecordier et al. 1994), and a travelling hydraulic jump (Hornung et al. 1995).

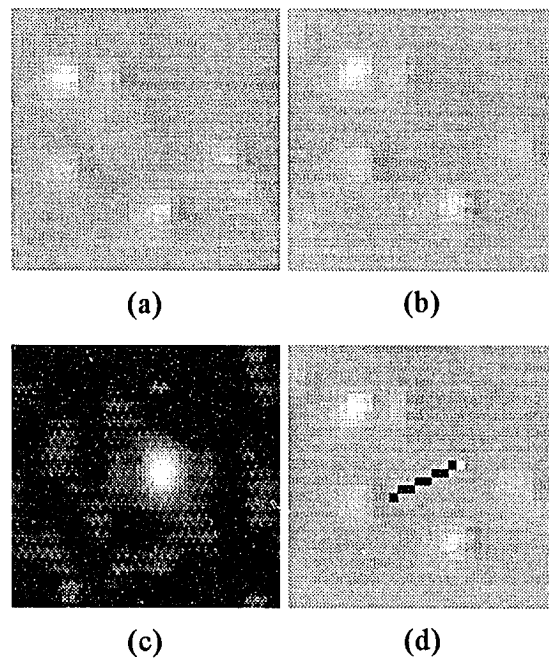


Fig. 3.1 Velocity determined using spatial crosscorrelation with 2 \times magnification in the Fourier domain: (a) particle image, (b) particle image Δt later, (c) crosscorrelation, (d) velocity vector.

3.3.1 Optical design

The basic layout of a digital particle image velocimeter is shown in Fig.

3.2. The laser beam is expanded to illuminate the particles in the test section. The test section is imaged on to the camera in a direction perpendicular to the illumination direction.

The particle images are acquired using an NEC Corporation TI-23A solid state charge coupled

device camera. The usable camera area is 512 pixels wide \times 480 pixels high. Each pixel measures 12.8 μm wide \times 9.9 μm high. The particle images are stored on Fuji Hi8 MP video tape using a Sony EV-S2000 Hi8 video cassette recorder. Timing signals are sent to the audio track of the video tape using a MetraByte Corporation Dascon-1 digital-analog expansion board. The timing signals indicate the location of the particle images on the video tape. A Siemens 40 mW helium-neon continuous wave laser with a wavelength of 632.8 nm is used to produce the particle images. The laser beam is expanded to form a sheet of light using a cylindrical lens.

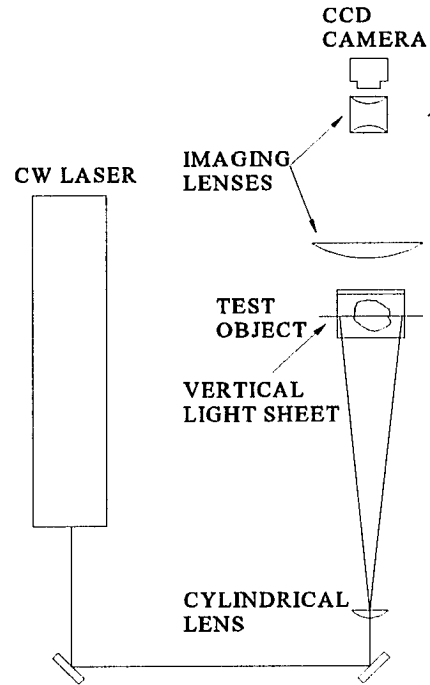


Fig. 3.2 Schematic of a digital particle image velocimeter.

3.3.2 Timing signals

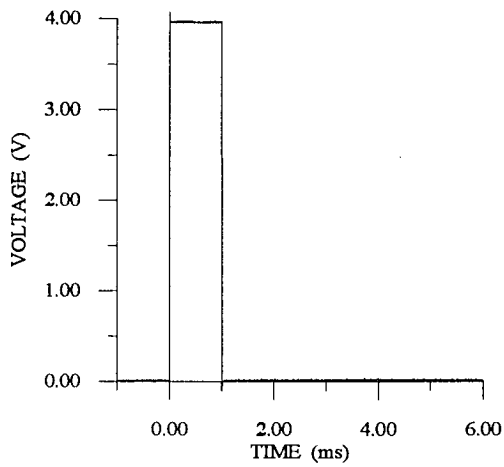
Since the particle images are stored on video tape, timing signals are necessary to indicate the time at which the particle images were recorded. Each timing signal is a 1 ms voltage pulse sent to the audio track of the video tape. After the desired experiment is run, the particle images are transferred to the frame grabber using the timing signals. The timing signals are detected using the digital-analog expansion board. Since the audio track attenuates the high frequency components of the timing signal, an amplifier circuit is necessary. This circuit depends on the characteristics of the recorded timing signal. The timing signal, recorded signal, amplifier circuit, and amplifier circuit output are shown for a VHS video cassette recorder in Fig. 3.3 and for a Hi8 video cassette recorder in Fig. 3.4.

3.3.3 Particle size

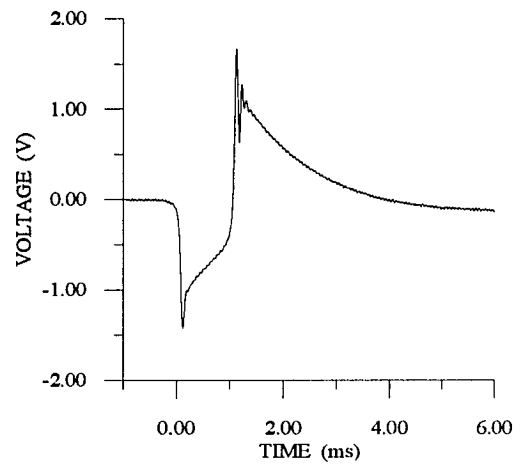
The diameter of the image of a particle is found from the convolution of the point spread function with the image predicted by geometrical optics (Goodman 1968; Hecht and Zajac 1979). The two-dimensional convolution (Bracewell 1965; Goodman 1968) is given by

$$h_{fg}(X, Y) = \int_{-\infty}^{\infty} \int_{-\infty}^{\infty} f(x, y) g(X-x, Y-y) dx dy . \quad (3.8)$$

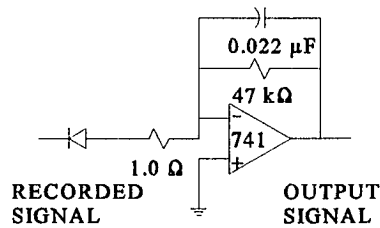
By use of the Fourier transform the equation becomes



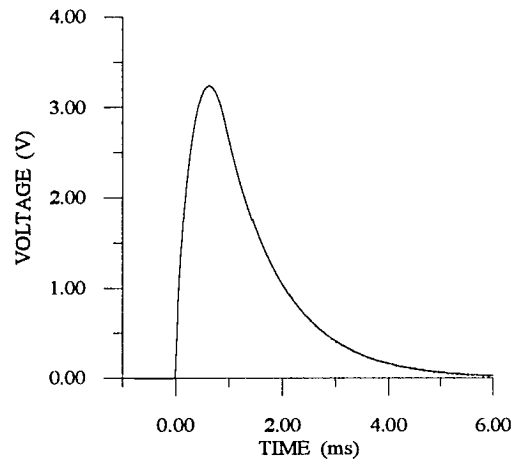
(a)



(b)



(c)



(d)

Fig. 3.3 Timing signals for a VHS video cassette recorder: (a) timing signal, (b) recorded signal, (c) amplifier circuit, (d) output signal.

$$h_{fg}(X, Y) = \mathcal{F}^{-1}[F(k_x, k_y)G(k_x, k_y)] \quad (3.9)$$

The point spread function is proportional to the Airy irradiance distribution function

(Hecht and Zajac 1979) and is given by

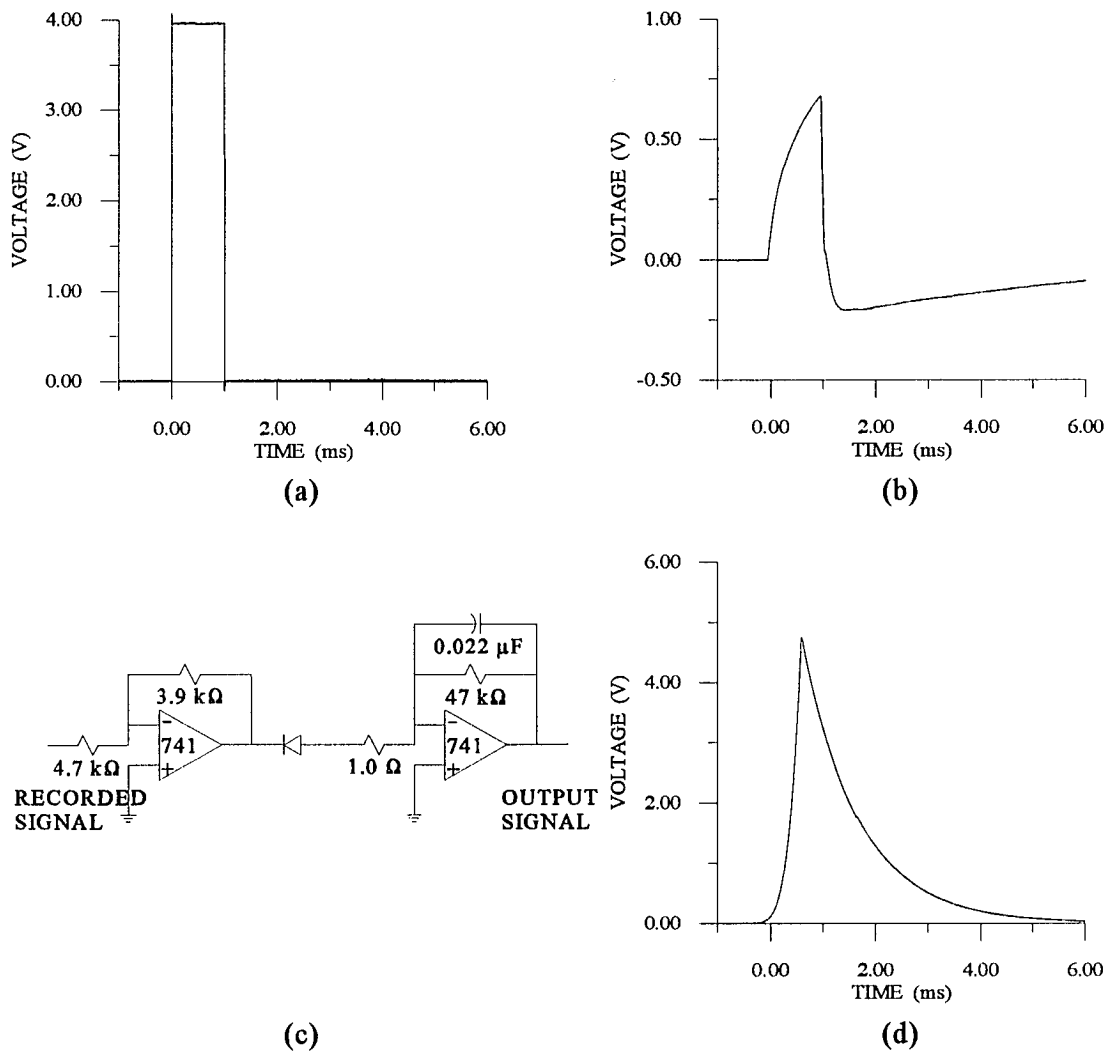


Fig. 3.4 Timing signals for a Hi8 video cassette recorder: (a) timing signal, (b) recorded signal, (c) amplifier circuit, (d) output signal.

$$I_s(r) \propto \left[\frac{2J_1\left(\frac{kDr}{2s_i}\right)}{\frac{kDr}{2s_i}} \right]^2, \quad (3.10)$$

where J_1 is the Bessel function of the first kind of order 1, k is the wavenumber, D is the diameter of the lens, r is the radius of the image, and s_i is the image distance from the lens.

The wavenumber is defined by

$$k = \frac{2\pi}{\lambda} \quad (3.11)$$

The point spread function is approximated by the axisymmetric Gaussian function

$$I_s(r) \propto e^{-ar^2}, \quad (3.12)$$

where a is a constant, in which the value of the Gaussian is 0.025 at the first zero of the Airy distribution (Fig. 3.5), and the irradiance distribution in the geometrical image of a particle is approximated by the axisymmetric Gaussian function in which the value of the Gaussian is 0.025 at the geometrical image radius

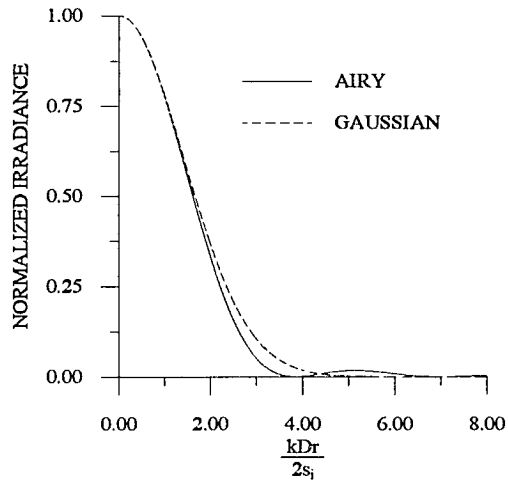


Fig. 3.5 Approximation of Airy distribution using Gaussian function.

(Adrian and Yao 1985). The point spread function is approximated by

$$I_s(r) \propto e^{-[0.251252 \left(\frac{kD}{2s_i}\right)^2]r^2}, \quad (3.13)$$

and the geometrical image is approximated by

$$I_i(r) \propto e^{-[3.68888 \left(\frac{s_{o1}s_{o2}-s_oN}{s_{i1}s_{i2}-s_iN} \frac{2}{\phi_o}\right)^2]r^2}, \quad (3.14)$$

where s_{oi} is the object distance from lens i , s_{ii} is the image distance from lens i , N is the

number of lenses, and ϕ_o is the diameter of the particle. The diameter of the image of a particle is found using Eqs. (3.9), (3.13), and (3.14). The two-dimensional Fourier transform is axisymmetric and is expressed as the Hankel transform, a one dimensional Fourier transform with a Bessel function kernel (Bracewell 1965). The diameter of the image of a particle is approximated by

$$\phi_i = \sqrt{\left(\frac{s_{i1}s_{i2}\dots s_{iN}}{s_{o1}s_{o2}\dots s_{oN}}\right)^2 \phi_o^2 + (2.44)^2 \left[\left(\frac{\lambda s_{i1}}{D_1}\right)^2 + \left(\frac{\lambda s_{i2}}{D_2}\right)^2 + \dots + \left(\frac{\lambda s_{iN}}{D_N}\right)^2 \right]}, \quad (3.15)$$

where D_i is the diameter of lens i .

The uncertainty (Holman 1989) in the fluid velocity measurement determined using Eq. (3.4) is given by

$$\epsilon_u = \frac{1}{\Delta t} \sqrt{\epsilon_d^2 + u^2 \epsilon_{\Delta t}^2}, \quad (3.16)$$

where ϵ_d is the uncertainty in the displacement measurement and $\epsilon_{\Delta t}$ is the uncertainty in the time between exposures. Unless the velocity is very large, the equation becomes

$$\epsilon_u = \frac{\epsilon_d}{\Delta t}, \quad (3.17)$$

since the uncertainty in the time between exposures is typically small compared to the uncertainty in the displacement measurement (Adrian 1991b). The uncertainty in the displacement measurement is written as

$$\epsilon_d = c \phi_i \quad (3.18)$$

(Adrian 1991b), where c is a constant that depends on the method used to determine the displacement of the particle images. The accuracy of the fluid velocity measurement is

$$\frac{\epsilon_u}{u(x,y)} = \frac{c \phi_i}{d(x,y)} \quad (3.19)$$

Accuracy is proportional to the ratio of the diameter of the particle images to the separation of the images (Adrian and Yao 1985). Therefore, maximum accuracy is obtained by using small particles (Adrian 1991b).

For spherical particles the scattered irradiance is given by

$$I_1(\beta, z) = \frac{|S_2(\beta)|^2}{k^2 z^2} I_{01} \quad (3.20)$$

for polarization parallel to the scattering plane, and

$$I_{\perp}(\beta, z) = \frac{|S_1(\beta)|^2}{k^2 z^2} I_{0\perp} \quad (3.21)$$

(van de Hulst 1981), for polarization perpendicular to the scattering plane, where $S(\beta)$ is a complex amplitude function describing the amplitude and phase of a scattered scalar wave, β is the scattering angle from the forward direction, z is the distance from the particle, and I_0 is the incident irradiance in the light sheet. The average irradiance in the image of a particle is determined by the scattered irradiance gathered by the imaging system and is given by

$$\bar{I}_i(\beta) = \frac{NA^2 s_{o1}^2}{\phi_i^2} \frac{|S(\beta)|^2}{k^2 s_{o1}^2} I_0 \quad (3.22)$$

where NA is the numerical aperture. The numerical aperture is determined by

$$NA = \frac{|s_{i1}|}{|s_{o1}|} \frac{|s_{i2}|}{|s_{o2}|} \dots \frac{|s_{i(N-1)}|}{|s_{o(N-1)}|} \frac{D_N}{|s_{oN}|} , \quad (3.23)$$

where D_N is found by iterating through the lenses from 2 to N calculating

$$D_i = \min(D_i, \frac{D_{i-1}}{|s_{i(i-1)}|} |s_{oi}|) . \quad (3.24)$$

The average exposure is given by

$$\bar{E} = \bar{I} t_E , \quad (3.25)$$

where t_E is the exposure time. The average exposure of a particle is then

$$\bar{E}_i(\beta) = \frac{\lambda^2 NA^2 |S(\beta)|^2 I_0 t_E}{4\pi^2 \left\{ \left(\frac{s_{i1}s_{i2}\dots s_{iN}}{s_{o1}s_{o2}\dots s_{oN}} \right)^2 \Phi_o^2 + (2.44)^2 \left[\left(\frac{\lambda s_{i1}}{D_1} \right)^2 + \left(\frac{\lambda s_{i2}}{D_2} \right)^2 + \dots + \left(\frac{\lambda s_{iN}}{D_N} \right)^2 \right] \right\}} . \quad (3.26)$$

Adrian and Yao (1985) performed Mie scattering calculations for light scattered perpendicular to the illumination direction for particles from 1 μm to 20 μm in diameter in both air and water. They determined that for particles in the range from 1 μm to 10 μm in diameter, the scattering is

$$|S(\beta)|^2 \propto \left(\frac{\Phi_o}{\lambda} \right)^3 , \quad (3.27)$$

and for particles larger than 10 μm in diameter, the scattering is

$$|S(\beta)|^2 \propto \left(\frac{\Phi_o}{\lambda} \right)^2 \quad (3.28)$$

(Adrian and Yao 1985; Adrian 1991a). For particles on the order of the wavelength of the light, the point spread function dominates the denominator, and Eq. (3.26) becomes

$$\bar{E}_i \sim \frac{\phi_o^3 NA^2 I_0 t_E}{\lambda^3 \left[\left(\frac{s_{i1}}{D_1} \right)^2 + \left(\frac{s_{i2}}{D_2} \right)^2 + \dots + \left(\frac{s_{iN}}{D_N} \right)^2 \right]} \quad (3.29)$$

using Eq. (3.27). For particles large compared to the wavelength of the light, the geometrical image dominates the denominator, and Eq. (3.26) becomes

$$\bar{E}_i \sim \frac{NA^2 I_0 t_E}{\left(\frac{s_{i1} s_{i2} \dots s_{iN}}{s_{o1} s_{o2} \dots s_{oN}} \right)^2} \quad (3.30)$$

using Eq. (3.28). For particles in the range from 1 μm to 10 μm in diameter, the exposure is proportional to the diameter of the particle cubed as shown in Eq. (3.29). For particles larger than 10 μm in diameter, the exposure is independent of the diameter of the particle as shown in Eq. (3.30).

The optimum particle size is a compromise between accuracy and exposure (Adrian and Yao 1985). For particle images acquired using a video camera, the spatial resolution is limited by the size of the pixels, and the exposure is averaged over the area of a pixel. Therefore accuracy and signal to noise ratio are both maximized when the size of the image of a particle is on the order of a pixel. The size of the image of a particle is determined using Eq. (3.15). This typically results in a particle size in which Eq. (3.30) applies, where the exposure is independent of particle size.

3.4 Conclusions

The optical and electronic design of a system for DPIV has been discussed. It has been shown that video tape storage of the particle images is possible using timing signals. The diameter of the image of a particle for a multiple lens system has been derived, including a discussion of accuracy and exposure considerations for determining the optimum particle size for a given system.

References

- Adrian, R. J. 1984: Scattering particle characteristics and their effect on pulsed laser measurements of fluid flow: speckle velocimetry vs particle image velocimetry. *Appl. Opt.* **23**, 1690-1691.
- Adrian, R. J.; Yao, C. S. 1985: Pulsed laser technique application to liquid and gaseous flows and the scattering power of seed materials. *Appl. Opt.* **24**, 44-52.
- Adrian, R. J. 1986: Image shifting technique to resolve directional ambiguity in double-pulsed velocimetry. *Appl. Opt.* **25**, 3855-3858.
- Adrian, R. J. 1991a: Particle-imaging techniques for experimental fluid mechanics. *Annu. Rev. Fluid Mech.* **23**, 261-304.
- Adrian, R. J. 1991b: Optical instrumentation for measurement of fluid velocity fields. In *Fluids Engineering* (eds. J. H. Kim; J. M. Hyun; C. -O. Lee). New York: Hemisphere, 311-329.
- Barker, D. B.; Fourney, M. E. 1977: Measuring fluid velocities with speckle patterns. *Opt. Lett.* **1**, 135-137.
- Bracewell, R. 1965: *The Fourier Transform and Its Applications*. New York: McGraw-Hill, 24-48, 241-250.

- Dudderar, T. D.; Simpkins, P. G. 1977: Laser speckle photography in a fluid medium. *Nature* **270**, 45-47.
- Goodman, J. W. 1968: *Introduction to Fourier Optics*. New York: McGraw-Hill, 4-25, 90-96.
- Grousseau, R.; Mallick, S. 1977: Study of flow pattern in a fluid by scattered laser light. *Appl. Opt.* **16**, 2334-2336.
- Hecht, E.; Zajac, A. 1974: *Optics*. Reading MA: Addison-Wesley, 109-116, 403-411.
- Holman, J. P. 1989: *Experimental Methods for Engineers*. New York: McGraw-Hill, 41-47.
- Hornung, H. G.; Willert, C.; Turner, S. 1995: The flow field downstream of a hydraulic jump. *J. Fluid Mech.* **287**, 299-316.
- Lecordier, B.; Mouqallid, M.; Vottier, S.; Rouland, E.; Allano, D.; Trinite, M. 1994: CCD recording method for cross-correlation PIV development in unstationary high speed flow. *Exp. Fluids* **17**, 205-208.
- Lourenco, L.; Krothapalli, A. 1987: The role of photographic parameters in laser speckle or particle image displacement velocimetry. *Exp. Fluids* **5**, 29-32.
- van de Hulst, H. C. 1981: *Light Scattering by Small Particles*. New York: Dover, 28-36.
- Vest, C. M. 1979: *Holographic Interferometry*. New York: John Wiley and Sons, 396-413.
- Willert, C. E.; Gharib, M. 1991: Digital particle image velocimetry. *Exp. Fluids* **10**, 181-193.

CHAPTER IV

TRANSIENT NATURAL CONVECTION IN INCLINED ENCLOSURES

4.1 Transient natural convection in enclosures

Transient natural convection in enclosures in which the temperatures of two opposing walls are initiated impulsively has been the focus of a number of experimental and numerical investigations. In the enclosures of interest convection boundary layers form on the heated and cooled walls. The boundary layers are redirected by the other two walls of the enclosure and flow across the enclosure as intrusion layers. Previous numerical results have indicated that transient oscillations consisting of two distinct boundary oscillations and a whole cavity oscillation occur during the initial stages of the flow. Several of the experimental studies confirm the existence of the two boundary layer oscillations, but none has shown the whole cavity oscillations. The present work is an effort to confirm the existence of all the transient oscillations experimentally.

Natural convection in inclined enclosures has also been studied using experimental and numerical methods. The angle of inclination has been shown to have a pronounced effect on the flow structure. In the present work scale analysis is used to determine the important terms in the equations of motion as a function of the angle of inclination and to

produce estimates of the time and length scales for the boundary layers and intrusion layers.

Simultaneous quantitative measurements of both the temperature and velocity fields for two-dimensional transient natural convection in an inclined rectangular enclosure are made. The fluid in the enclosure is initially stationary and isothermal. The transient boundary conditions are initiated impulsively by heating and cooling two opposing walls. The other two walls are insulated and nonconducting. The temperature is measured using calibrated multichannel electronic interferometry (CMEI), and the velocity is measured using digital particle image velocimetry (DPIV).

4.1.1 Previous work

The majority of whole field temperature and velocity results for transient natural convection in enclosures have been obtained using numerical methods (Patterson and Imberger 1980; Hall et al. 1988; Hamady et al. 1989; Schladow 1990; Patterson and Armfield 1990; Fusegi et al. 1991; Kuyper et al. 1993; Hiller 1993). Previous experimental results for the temperature field have been pointwise measurements using thermistors (Ivey 1984; Patterson and Armfield 1990) or thermocouples (Briggs and Jones 1985) which disturb the flow and average the temperature over their volume. Whole field measurements using standard interferometry (Hamady et al. 1989) have been made only for steady flow. Previous experimental results for the velocity field have been pointwise measurements using laser doppler velocimetry (Briggs and Jones 1985) or visualization

using streak photography (Ivey 1984; Patterson and Armfield 1990) and smoke visualization (Hamady et al. 1989), yielding only qualitative data. Simultaneous quantitative measurements of both the temperature and velocity fields appear to be limited to experiments using liquid crystal tracers and particle image velocimetry (Hiller et al. 1993), where different angles of inclination were not considered.

4.1.2 Classification

The classification of transient natural convection in inclined enclosures depends on the Prandtl number, the Rayleigh number, the aspect ratio, and the angle of inclination (Patterson and Imberger 1980; Hamady et al. 1989; Kuyper 1993; Bejan 1995). The Prandtl number is defined by

$$Pr = \frac{\nu}{\alpha}, \quad (4.1)$$

where ν is the kinematic viscosity and α is the thermal diffusivity. The thermal diffusivity is defined as

$$\alpha = \frac{k}{\rho C}, \quad (4.2)$$

where k is the thermal conductivity, ρ is the density, and C is the specific heat. The Rayleigh number is defined by

$$Ra = \frac{g\beta\Delta TH^3}{\nu\alpha}, \quad (4.3)$$

where g is the acceleration due to gravity, β is the volume expansion coefficient at constant pressure, ΔT is the temperature difference, and H is the height of the enclosure.

The temperature difference is defined as

$$\Delta T = T_w - T_0 , \quad (4.4)$$

where T_w is the wall temperature and T_0 is the initial fluid temperature. The aspect ratio is defined by

$$A = \frac{H}{W} , \quad (4.5)$$

where W is the width of the enclosure. The angle of inclination, γ , is defined by the angle of the heated wall from the horizontal direction.

4.1.3 Transient and periodic oscillations

At high Rayleigh numbers the flow exhibits oscillatory behavior which depends on the boundary conditions (Papanicolaou and Jaluria 1992). Transient oscillations occurring at startup and nondecaying periodic oscillations have been observed. Transient oscillations have been observed in enclosures consisting of two isothermal vertical walls and two insulated and nonconducting horizontal walls, while periodic oscillations have been observed in enclosures consisting of two isothermal vertical walls and two conducting horizontal walls in which a linear temperature gradient exists between the two isothermal vertical walls. A discussion of both transient and periodic oscillations is included for

completeness and because nonideal experimental boundary conditions may lead to both types.

Patterson and Imberger (1980) claimed the transient oscillations resulted because the entrainment length of the vertical boundary layers is greater than the thickness of the horizontal intrusion layers; as the discharged intrusion layers reach the vertical boundary layers, they spread against buoyancy to meet the entrainment length, tilting the isotherms beyond the horizontal and generating internal waves. In an experimental study Ivey (1984) did not see any evidence of regular cavity scale internal waves. He argued instead that the transient oscillations occurred because of an internal hydraulic jump (Yih 1977) with an increase in thickness of the horizontal intrusion layers as they emerge from the vertical boundary layers. The transient oscillations were stated to disappear as the interior is set in motion and stratifies in temperature, increasing the thickness of the intrusion and flooding the hydraulic jump. In a direct numerical simulation Schladow (1990) found transient oscillations consisting of two distinct boundary layer instabilities and a whole cavity oscillation. The first of the boundary layer instabilities was attributed to the leading edge effect of the vertical boundary layer. The second was attributed to the impact of the horizontal intrusion from the opposing vertical wall with the boundary layer. The frequency of these oscillations was determined by selective amplification of the disturbance and was higher than the frequency of the whole cavity oscillations. The whole cavity oscillations were attributed to the horizontal pressure gradient established by changes in the intrusion temperature field. These whole cavity oscillations were stated as determining the nature of the flow in the interior as the oscillation produces a flow in the

opposite direction of the intrusion flow. The internal hydraulic jump proposed by Ivey (1984) was shown instead to be a complex recirculation zone. In an experimental and numerical investigation Patterson and Armfield (1990) came to similar conclusions. The two boundary layer oscillations were attributed to travelling wave instabilities on the boundary layer caused first by initiation of the boundary layer and second by impact of the incoming intrusion. The whole cavity oscillations were stated to result from the splitting of the horizontal intrusion as it impacts the opposite wall. Armfield and Patterson (1992) stated that the first boundary layer instability takes the form of waves travelling in the flow direction caused by the initial singularity generated at the leading edge of the boundary layer. Temperature overshoot is possible if the temperature at a point rises to a higher value than at steady state before the leading edge arrives. They agreed that the boundary layer selectively amplifies a single wavenumber.

Briggs and Jones (1985) claimed the periodic oscillations are induced by the linear horizontal surface temperature. They stated that the vertical temperature gradient in the horizontal intrusions is unstable, since the hot intrusion is cooled from the top and the cold intrusion is heated from the bottom as they cross the enclosure. They hypothesized that the periodic oscillations are a resonance phenomena between travelling waves along the top and bottom of the enclosure and the natural buoyant frequency of the stratified fluid in the interior of the enclosure. Winters (1987) showed that the periodic oscillations arise as a Hopf bifurcation, and agreed with Briggs and Jones (1985) that the oscillations are the result of a resonance phenomena between the travelling waves and gravity waves in the stratified interior of the enclosure. Briggs and Jones (1985) claimed that the frequency of

the periodic oscillations is also proportional to the Brunt-Väisälä frequency.

Patterson and Imberger (1980) showed that the critical Rayleigh number for whole cavity transient oscillations in an enclosure consisting of two isothermal vertical walls and two insulated and nonconducting horizontal walls is

$$Ra_c \sim Pr^4 A^{-4} . \quad (4.6)$$

They found for a fluid with $Pr=7$ and an enclosure with $A=1$ the critical Rayleigh number for whole cavity transient oscillations to be $Ra_c \sim 2 \times 10^3$. By use of linear stability analysis, Gebhart and Mahajan (1982) determined that the frequency of the boundary layer transient oscillations is

$$\omega = \frac{\nu Ra^{\frac{2}{3}} \Omega}{H^2 Pr^{\frac{2}{3}}} , \quad (4.7)$$

where Ω is a generalized frequency. Patterson and Imberger (1980) showed that the frequency of the whole cavity transient oscillations is

$$\omega \sim \frac{N}{\sqrt{1+A^2}} , \quad (4.8)$$

where N is the Brunt-Väisälä frequency defined by

$$N = \max \sqrt{\frac{g}{\rho} \frac{d\rho}{dy}} \quad (4.9)$$

(Yih 1977), where $d\rho/dy$ is the density gradient. The scale for the Brunt-Väisälä

frequency is

$$N \sim \frac{\sqrt{\nu \alpha Ra}}{H^2} \quad (4.10)$$

(Patterson and Imberger 1980).

Briggs and Jones (1985) performed experiments using an air filled enclosure with $A=1$ consisting of two isothermal vertical walls and two conducting horizontal walls in which a linear temperature gradient exists between the two isothermal vertical walls. They found the critical Rayleigh number for periodic oscillations to be $Ra_c=3 \times 10^6$. For the same boundary conditions Winters (1987) determined the critical Rayleigh number for periodic oscillations to be $Ra_c=2.1 \times 10^6$ using linear stability methods. Winters (1987) determined the frequency of the periodic oscillations to be

$$\omega = \frac{1.9 \times 10^3 \alpha}{W^2} \quad (4.11)$$

using linear stability methods.

4.1.4 Problem description

The geometry of the two-dimensional inclined rectangular enclosure is shown in Fig. 4.1.

The fluid in the enclosure is modeled as Newtonian, incompressible, and constant property. The continuity equation is

$$\frac{\partial u}{\partial x} + \frac{\partial v}{\partial y} = 0, \quad (4.12)$$

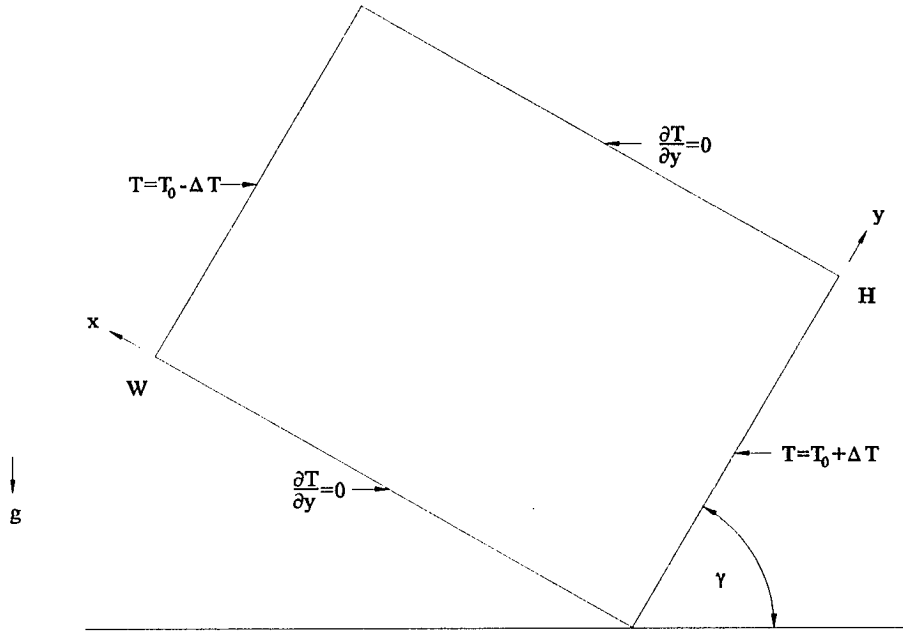


Fig. 4.1 Geometry of two-dimensional inclined rectangular enclosure.

where u is the velocity in the x direction and v is the velocity in the y direction. In an inclined enclosure buoyancy forces have both normal and tangential components relative to the walls. By use of the Boussinesq approximation the Navier-Stokes equation in the x direction is

$$\frac{\partial u}{\partial t} + u \frac{\partial u}{\partial x} + v \frac{\partial u}{\partial y} = -\frac{1}{\rho_0} \frac{\partial P}{\partial x} + \nu \left(\frac{\partial^2 u}{\partial x^2} + \frac{\partial^2 u}{\partial y^2} \right) - g[1 - \beta(T - T_0)] \cos(\gamma) , \quad (4.13)$$

and that in the y direction is

$$\frac{\partial v}{\partial t} + u \frac{\partial v}{\partial x} + v \frac{\partial v}{\partial y} = -\frac{1}{\rho_0} \frac{\partial P}{\partial y} + \nu \left(\frac{\partial^2 v}{\partial x^2} + \frac{\partial^2 v}{\partial y^2} \right) - g[1 - \beta(T - T_0)] \sin(\gamma) , \quad (4.14)$$

where P is the pressure and T is the temperature. In the Boussinesq approximation

changes in fluid properties are neglected everywhere except in the body force term. In the body force term the density is written as

$$\rho = \rho_0 [1 - \beta(T - T_0)] , \quad (4.15)$$

where ρ_0 is the initial fluid density. The energy equation is

$$\frac{\partial T}{\partial t} + u \frac{\partial T}{\partial x} + v \frac{\partial T}{\partial y} = \alpha \left(\frac{\partial^2 T}{\partial x^2} + \frac{\partial^2 T}{\partial y^2} \right) . \quad (4.16)$$

The initial conditions are those of a stationary,

$$u(x, y, 0) = 0 , \quad (4.17)$$

$$v(x, y, 0) = 0 , \quad (4.18)$$

and isothermal,

$$T(x, y, 0) = T_0 , \quad (4.19)$$

fluid. The boundary conditions for $t \geq 0$ are no flow and no slip on all walls,

$$u(0, y, t) = 0 , \quad u(W, y, t) = 0 , \quad u(x, 0, t) = 0 , \quad u(x, H, t) = 0 , \quad (4.20)$$

$$v(0, y, t) = 0 , \quad v(W, y, t) = 0 , \quad v(x, 0, t) = 0 , \quad v(x, H, t) = 0 , \quad (4.21)$$

and two opposing isothermal heated and cooled walls with the other two walls insulated and nonconducting,

$$T(0,y,t) = T_0 + \Delta T, \quad T(W,y,t) = T_0 - \Delta T, \quad \frac{\partial T(x,0,t)}{\partial y} = 0, \quad \frac{\partial T(x,H,t)}{\partial y} = 0. \quad (4.22)$$

4.1.5 Scale analysis

In scale analysis linear approximations are made to the terms in the continuity equation, the momentum equations, and the energy equation in a region of interest. For example, in a direction across the boundary layer a derivative term such as $\partial u/\partial x$ scales as u/δ , where δ is the boundary layer thickness, since as x goes from 0 to δ , u goes from 0 to u . The principles of scale analysis are discussed in detail by Bejan (1995).

The scale analysis discussed here follows the scaling arguments Patterson and Imberger (1980) made for an enclosure with $\gamma = \pi/2$, and the scale analysis is based on the assumption that both the vertical boundary layers and the horizontal intrusion layers are distinct. At times larger than the thermal boundary layer growth time τ , the fluid near the heated and cooled walls is characterized by a two-layer structure consisting of an inner thermal boundary layer of thickness δ_T and an outer wall jet of thickness δ_v shown in Fig. 4.2 (Patterson and Imberger 1980; Bejan 1995). The heated fluid from the thermal boundary layer crosses the enclosure in an intrusion layer, while the unheated fluid from the wall jet discharges as a potential flow into the interior of the enclosure (Patterson and Imberger 1980; Bejan 1995).

The thermal boundary layer grows until the heat conducted in through the wall is balanced by that convected away by the buoyant layer (Patterson and Imberger 1980;

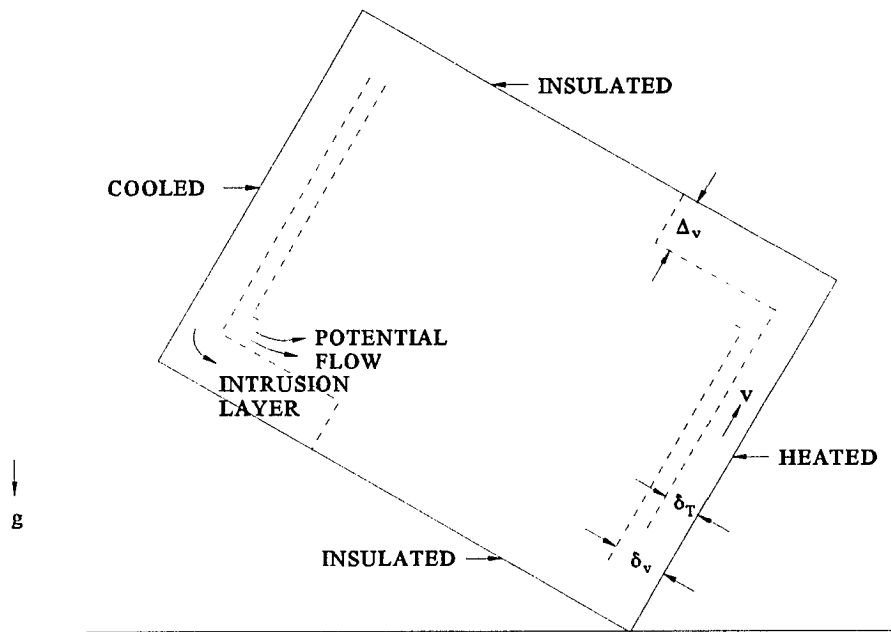


Fig. 4.2 Two-layer flow structure.

Bejan 1995). For a fluid with $Pr \geq 1$ the thickness scale for the thermal boundary layer is

$$\delta_T \sim \frac{H}{[\sin(\gamma)Ra]^{\frac{1}{4}}}, \quad (4.23)$$

the growth time scale is

$$\tau \sim \frac{H^2}{\alpha [\sin(\gamma)Ra]^{\frac{1}{2}}}, \quad (4.24)$$

and the velocity scale is

$$v \sim \frac{\alpha [\sin(\gamma)Ra]^{\frac{1}{2}}}{H}, \quad (4.25)$$

based on a balance between convection and conduction in the energy equation. The diffusion of momentum out of the thermal boundary layer maintains an outer velocity boundary layer in which the effect of buoyancy is minor (Patterson and Imberger 1980; Bejan 1995). The thickness scale for the velocity boundary layer is

$$\delta_v \sim \frac{HPr^{\frac{1}{2}}}{[\sin(\gamma)Ra]^{\frac{1}{4}}}, \quad (4.26)$$

based on a balance between inertia and viscous diffusion in the momentum equation.

The thermal boundary layer is distinct if $\delta_T < W$, which occurs when

$$A < [\sin(\gamma)Ra]^{\frac{1}{4}} \quad (4.27)$$

using Eq. (4.23). The velocity boundary layer is distinct if $\delta_v < W$, which occurs when

$$A < \frac{[\sin(\gamma)Ra]^{\frac{1}{4}}}{Pr^{\frac{1}{2}}} \quad (4.28)$$

using Eq. (4.26). The intrusion layer is distinct if the heat conducted out is small compared to that convected across the enclosure (Bejan 1995), which occurs when

$$\frac{1}{A} < [\sin(\gamma)Ra]^{\frac{1}{4}}. \quad (4.29)$$

For high Rayleigh numbers the conditions of both Eqs. (4.27) and (4.29) are satisfied, and the flow is in the boundary layer regime (Bejan 1995).

If $\gamma \sim \pi/2$ the intrusion layer is dominated by pressure resulting from buoyancy in the boundary layer, and the thickness scale for a viscous intrusion layer is

$$\Delta_v \sim \frac{H^{\frac{3}{4}} W^{\frac{1}{4}}}{Ra^{\frac{3}{16}}}, \quad (4.30)$$

and the time scale for the intrusion layer to travel across the enclosure is

$$T_v \sim \frac{H^{\frac{3}{4}} W^{\frac{5}{4}}}{\alpha Ra^{\frac{7}{16}}} \quad (4.31)$$

(Patterson and Imberger 1980), based on a balance between boundary layer buoyancy and viscous diffusion in the momentum equation. If $\gamma \neq \pi/2$ the intrusion layer is dominated by buoyancy in the intrusion layer itself, and the thickness scale for a viscous intrusion layer is

$$\Delta_v \sim \frac{H [\sin(\gamma)]^{\frac{1}{12}}}{[\cos(\gamma)]^{\frac{1}{3}} Ra^{\frac{1}{4}}}, \quad (4.32)$$

and the time scale for the intrusion layer to travel across the enclosure is

$$T_v \sim \frac{HW}{\alpha [\sin(\gamma)]^{\frac{1}{6}} [\cos(\gamma)]^{\frac{1}{3}} Ra^{\frac{1}{2}}}, \quad (4.33)$$

based on a balance between intrusion layer buoyancy and viscous diffusion in the

momentum equation.

For an enclosure with $\gamma=\pi/2$ Patterson and Imberger (1980) classified the flow into one of three regimes. In the first regime for $Ra<1$, the flow is primarily conductive approaching a linear horizontal temperature gradient at steady state. In the second regime for $Ra>Ra_c$, where the critical Rayleigh number for convection is

$$Ra_c \sim \max(Pr^2, A^{-\frac{4}{3}}, A^{-12}) \quad (4.34)$$

(Patterson and Imberger 1980), horizontal intrusion layers convect heat across the enclosure creating a primarily vertical temperature gradient in the interior of the enclosure. The third regime for $1<Ra<Ra_c$ is a transition region between the conduction and convection regimes.

4.2 Simultaneous quantitative measurements of both the temperature and velocity fields

Simultaneous quantitative measurements were made of both the temperature and velocity fields using CMEI and DPIV. A calibrated multichannel electronic interferometer (Fig. 2.1) and a digital particle image velocimeter (Fig. 3.2) were implemented simultaneously using the combined optical setup shown in Fig. 4.3. A 50/50 pellicle beamsplitter with a 76.2 mm diameter clear aperture was used to split the object beam to allow simultaneous acquisition of temperature and velocity data. The evolution of the flow to steady state was determined for a Prandtl number of 6.38, a Rayleigh number of 1.5×10^5 , and an

aspect ratio of 1.0, at angles of inclination of $\pi/4$, $\pi/2$, and $3\pi/4$.

4.2.1 Experimental design

The experiments were performed in a rectangular enclosure measuring 3.0 cm wide \times 3.0 cm high \times 6.0 cm long consisting of two isothermal walls and two insulated and nonconducting walls (Fig. 4.4). The enclosure was constructed from acrylic glass 5.4 mm thick. The two isothermal walls were made from 0.30 mm thick

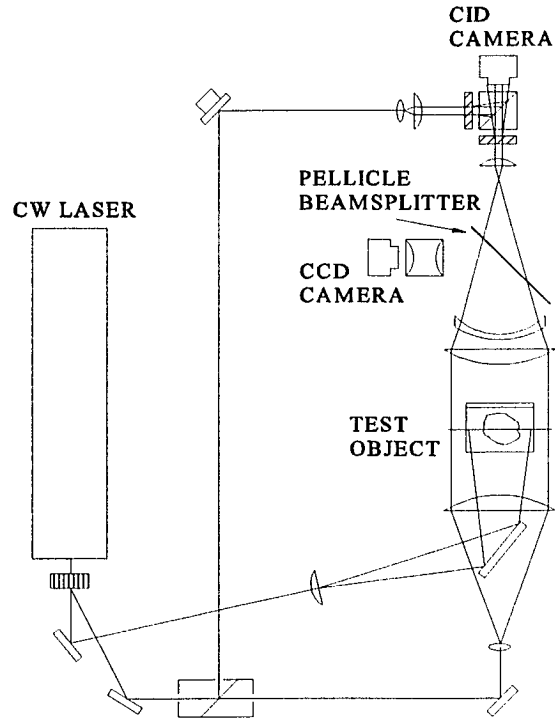


Fig. 4.3 Schematic of the simultaneous implementation of a calibrated multichannel electronic interferometer (Fig. 2.1) and a digital particle image velocimeter (Fig. 3.2).

experimental grade copper. The two walls in the interferometer path were 12.7 mm thick optical windows made from BK-7. The seal between the optical windows and the enclosure was made using rubber o-rings and an adjustable clamp system. The enclosure was filled with water seeded with particles. The optical windows and the adjustable clamp system were necessary to eliminate refraction in the phase object path as the light passed through the interfaces between the air, water, and windows. The particles used were Bangs Laboratories Incorporated P0750000PN macro beads made from styrene and paramethylstyrene. They had a density of 1.020 kg/m³ and a diameter range of 50 μ m to

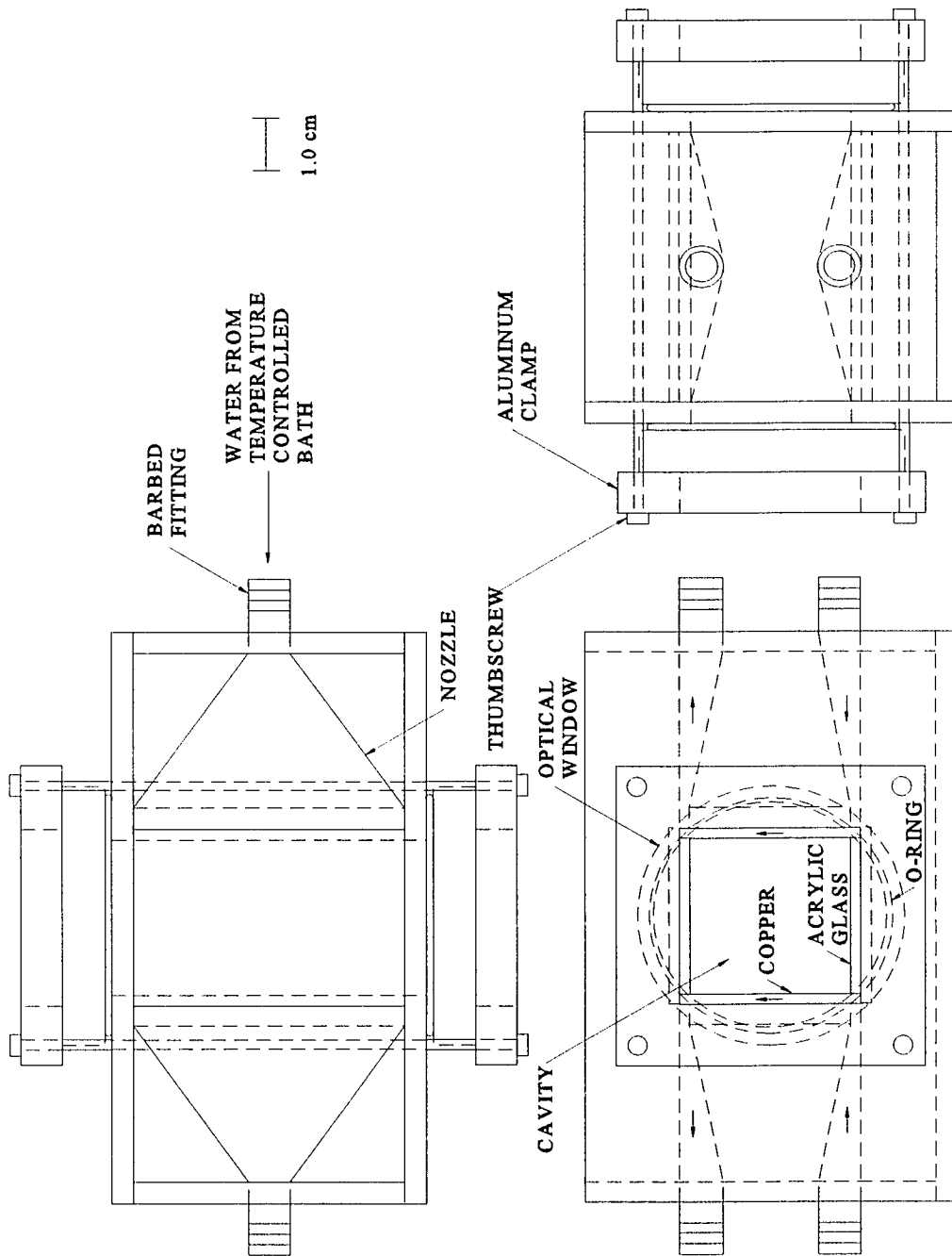


Fig. 4.4 Schematic of the natural convection enclosure.

90 μm with an average diameter of 75.000 μm . To make the particles neutrally buoyant, sodium bicarbonate was added to the water in the enclosure until its density was 1.02 kg/m^3 .

NESLAB Instruments Incorporated EX-111D and RTE-111D temperature controlled baths with water as the working fluid were used to control the temperature of the two isothermal walls. The temperature stability of the baths was specified as ± 0.01 $^\circ\text{C}$. The EX-111D bath was maintained at $T_h = T_0 + \Delta T$, while the RTE-111D bath was maintained at $T_c = T_0 - \Delta T$. The magnitude of ΔT was limited due to refraction errors. In order for the deviation due to refraction to be less than $\lambda/10$,

$$\frac{\left(\frac{dn}{dy}\right)^2 z_p^3}{n(y)\lambda_0} < 0.3 \quad (4.35)$$

(Vest 1979), where dn/dy is the refractive index gradient, z_p is the path length through the phase object, $n(y)$ is the refractive index, and λ_0 is the wavelength of the light. The maximum temperature gradient is then given by

$$\frac{dT}{dy} < \sqrt{0.3 \frac{n(y)\lambda_0}{\left(\frac{dn}{dT}\right)^2 z_p^3}}, \quad (4.36)$$

where dn/dT is the change in the refractive index with temperature. For a linear temperature gradient, the temperature difference is limited to

$$\Delta T < \left[\frac{v \alpha H}{g \beta \sin(\gamma)} \right]^{\frac{1}{5}} \left[0.3 \frac{n(y)\lambda_0}{\left(\frac{dn}{dT}\right)^2 z_p^3} \right]^{\frac{2}{5}} \quad (4.37)$$

using Eqs. (4.23) and (4.36). For an enclosure with $\gamma=\pi/2$ the temperature difference is limited to $\Delta T < 0.47$ °C. Since the temperature of the EX-111D bath was close to the ambient temperature, additional cooling was required. This was accomplished by circulating the bath fluid between the RTE-111D and the EX-111D. The circulation to the two isothermal vertical walls was controlled using two ASCO 8320G178 three way solenoid valves with an operating voltage of 24 V DC. The solenoid valves were located near the enclosure, and the bath fluid was circulated through the valves while de-energized to bring the plumbing to the bath temperature. The solenoid valves were controlled by a MetraByte Corporation Dascon-1 digital-analog expansion board which switched a 24 V DC power supply using a relay with a 12 V DC coil. The ambient temperature and the initial temperature of the fluid in the enclosure was approximately $T_0=24$ °C. To satisfy the condition of Eq. (4.37), the

temperature difference was $\Delta T=0.30$ °C. To accurately determine ΔT , a system of Copper-Constantan thermocouples was used (Fig. 4.5).

The system was designed to result in a voltage difference $\Delta V=0$ V when ΔT for both the hot and cold baths was the same. The output voltage was measured using a Doric DS-100 integrating microvoltmeter. The

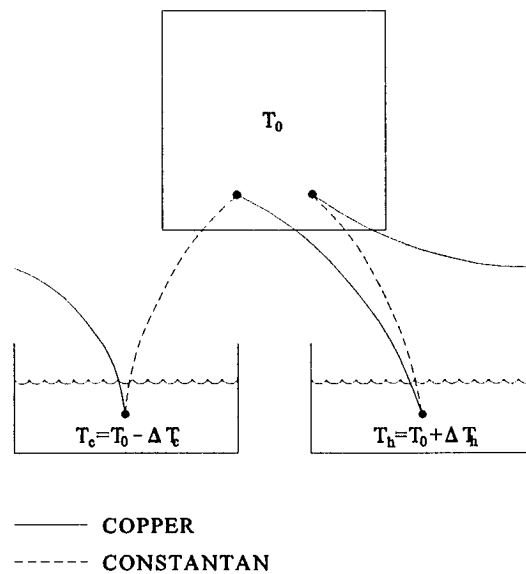


Fig. 4.5 Schematic of the temperature difference measurement system.

sensitivity of the system was found to be 0.081 mV/°C (Powell 1976).

4.2.2 Analysis

The flow is classified by $Pr=6.38$, $Ra=1.5\times 10^5$, and $A=1.0$ using Eqs. (4.1), (4.3), and (4.5). For an enclosure with $\gamma=\pi/2$ the critical Rayleigh number for convection is $Ra_c\sim 40$ using Eq. (4.34), and the critical Rayleigh number for whole cavity transient oscillations is $Ra_c\sim 2\times 10^3$ using Eq. (4.6). This flow is in a convective regime where transient oscillations are expected. To obtain accurate transient results, it is important that the initiation time of the experiment be small compared to the growth time scale of the thermal boundary layer (Patterson and Armfield 1990). The growth time scale for the thermal boundary layer is $\tau\sim 16$ s using Eq. (4.24). To initiate the transient boundary conditions, the solenoids were energized, and water from the temperature controlled baths was pumped to the two isothermal vertical walls at a volume flow rate of 1.7×10^{-5} m³/s. At this flow rate the space next to the walls was filled in 0.3 s. The time for the walls to reach $0.9\Delta T$ was found to be 1.7 s using lumped heat capacity analysis (Kreith and Bohn 1993). This resulted in an initiation time of 2.0 s. Previous experimental studies (Ivey 1984; Patterson and Armfield 1990) based the initiation time on the conduction time scale through the walls, which is given by

$$\tau_c \sim \frac{x_w^2}{\alpha}, \quad (4.38)$$

where x_w is the wall thickness. This time scale does not correctly describe the time

required for the isothermal vertical walls to reach ΔT .

Time resolution of the transient temperature and velocity fields requires a sequence of instantaneous data. The time resolution of a transient flow using CMEI and DPIV is limited by the exposure time and the frame rate. To capture an instant in time, the exposure time has to be less than the time the flow moves one camera pixel. The frame rate has to be large enough to resolve the time scales of the flow. To determine the frequency content of a time dependent signal, the sample rate must be more than twice the highest frequency contained in the signal (Figliola and Beasley 1995). Frequencies in the signal higher than the Nyquist frequency are not properly represented. The exposure time for the temperature field was 0.050 ms, and that for the velocity field was 33 ms. The maximum frame rate for the temperature field was 70 Hz, and that for the velocity field was 30 Hz. Typically the frame rate used for both the temperature and velocity fields was 2.5 Hz. However, the time between the two particle images used to determine the velocity field ranged from 0.27 s to 1.1 s, depending on the flow velocity. Measurement of velocity time scales on the order of the time between the two particle images or less was not possible. Gebhart and Mahajan (1982) reported that for $Pr=6.38$ a generalized frequency of $\Omega=0.28$ has the highest amplification rate. By use of this value in Eq. (4.7), the frequency of the two boundary layer transient oscillations is $f=0.037$ Hz. The frequency of the whole cavity transient oscillations is $f\sim 0.018$ Hz using Eqs (4.8) and (4.10). The frame rate was high enough to resolve both the boundary layer oscillations and the whole cavity oscillations.

Four different quantities have been used to indicate the two boundary layer

oscillations. These are the temperature in the boundary layer, the velocity in the boundary layer, the Nusselt number at the wall of the enclosure, and the Nusselt number at the center of the enclosure, all functions of time (Ivey 1984; Patterson and Armfield 1990; Schladow 1990; Armfield and Patterson 1991). Of these four quantities, the whole cavity oscillations have been apparent only in Nusselt number at the center of the enclosure (Patterson and Imberger 1980; Patterson and Armfield 1990; Schladow 1990).

The Nusselt number is defined by

$$Nu = \frac{\bar{h}W}{k}, \quad (4.39)$$

where \bar{h} is the average convection heat transfer coefficient defined by

$$\bar{h} = \frac{q}{2H\Delta T}, \quad (4.40)$$

where q is the rate of heat transfer. By use of Eqs. (4.39) and (4.40) the Nusselt number at the wall of the enclosure is written as

$$Nu_w = \frac{1}{2kA\Delta T_0} \int_0^H \left(-k \frac{\partial T}{\partial x}\right) dy, \quad (4.41)$$

and the Nusselt number at the center of the enclosure is written as

$$Nu_c = \frac{1}{2kA\Delta T_0} \int_0^H \left(\rho C u T - k \frac{\partial T}{\partial x}\right) dy \quad (4.42)$$

(Patterson and Imberger 1980; Schladow 1990). The Nusselt number at the wall and the

center of the enclosure are determined from the experimental data using numerical integration. The equations are written as

$$Nu_w = \frac{1}{2kA\Delta T_{i-1}} \sum_{i=1}^N \left(-k \frac{\partial T}{\partial x}\right)_i \Delta y \quad (4.43)$$

and

$$Nu_c = \frac{1}{2kA\Delta T_{i-1}} \sum_{i=1}^N \left(\rho C u T - k \frac{\partial T}{\partial x}\right)_i \Delta y \quad (4.44)$$

where

$$\Delta y = \frac{H}{N} \quad (4.45)$$

and N is the number of data points. Typically 30 intervals are used in Eqs. (4.43) and (4.44).

The temperature field is determined using

$$T = \frac{\Delta \Theta}{\frac{dn}{dT} \frac{2\pi r_p}{\lambda_0}} + T_0 \quad (4.46)$$

where $\Delta \Theta$ is the phase difference and T_0 is the reference temperature. In a small region the temperature field is approximated by the linear function

$$T(x,y) = \frac{\partial T}{\partial x} dx + \frac{\partial T}{\partial y} dy + T(0,0) \quad (4.47)$$

The temperature and temperature gradient are determined using the method of least squares (Yamane 1967; Holman 1989). If variation in only the x direction is considered,

the temperature is given by

$$T(x) = \frac{\partial T}{\partial x} x + T(0) , \quad (4.48)$$

where

$$T(0) = \frac{\sum_{i=1}^N x_i^2 \sum_{i=1}^N T_i - \sum_{i=1}^N x_i \sum_{i=1}^N x_i T_i}{N \sum_{i=1}^N x_i^2 - (\sum_{i=1}^N x_i)^2} \quad (4.49)$$

and

$$\frac{\partial T}{\partial x} = \frac{N \sum_{i=1}^N x_i T_i - \sum_{i=1}^N x_i \sum_{i=1}^N T_i}{N \sum_{i=1}^N x_i^2 - (\sum_{i=1}^N x_i)^2} \quad (4.50)$$

(Yamane 1967; Holman 1989), where $T(x_i)$ is the measured data. This reduces the uncertainty to

$$\epsilon_T = \frac{\epsilon_{T_i}}{\sqrt{N}} \quad (4.51)$$

(Holman 1989). Noise in the phase difference is on the order of $\pm\pi/10$. Typically five pixels are used in Eqs. (4.49) and (4.50), resulting in an uncertainty in the temperature field of ± 0.002 °C and an uncertainty in the temperature gradient of ± 0.002 °C/mm using Eqs. (4.46) and (4.51). The velocity field is determined to 0.5 pixel accuracy, resulting in

an uncertainty in the velocity field of typically ± 0.06 mm/s. The uncertainty in the Nusselt number measurement at the wall of the enclosure is given by

$$\epsilon_{Nu_w} = \frac{1}{2kA\Delta T} \sqrt{\sum_{i=1}^N [(-k)_i \Delta y \epsilon_{\frac{\partial T}{\partial x}}]^2}, \quad (4.52)$$

and the uncertainty in the Nusselt number measurement at the center of the enclosure is given by

$$\epsilon_{Nu_c} = \frac{1}{2kA\Delta T} \sqrt{\sum_{i=1}^N [(\rho C \Delta T)_i \Delta y \epsilon_u]^2 + \sum_{i=1}^N [(\rho C u)_i \Delta y \epsilon_T]^2 + \sum_{i=1}^N [(-k)_i \Delta y \epsilon_{\frac{\partial T}{\partial x}}]^2}, \quad (4.53)$$

where $\epsilon_{\partial T/\partial x}$ is the uncertainty in the temperature gradient, ϵ_u is the uncertainty in the velocity field, and ϵ_T is the uncertainty in the temperature field. The equations are written as

$$\epsilon_{Nu_w} = \frac{1}{2kA\Delta T} \frac{H}{\sqrt{N}} k \epsilon_{\frac{\partial T}{\partial x}} \quad (4.54)$$

and

$$\epsilon_{Nu_c} = \frac{1}{2kA\Delta T} \frac{H}{\sqrt{N}} \sqrt{[\rho C \Delta T \epsilon_u]^2 + [\rho C u \epsilon_T]^2 + [k \epsilon_{\frac{\partial T}{\partial x}}]^2} \quad (4.55)$$

using Eq. (4.45). The uncertainty in the Nusselt number measurement at the wall is ± 0.02 using Eq. (4.54), and the uncertainty in the Nusselt number measurement at the center is ± 0.6 using Eq. (4.55).

4.2.3 Results and discussion

The temperature and velocity fields during the evolution of the flow to steady state are shown for $\gamma=\pi/4$ in Fig. 4.6, $\gamma=\pi/2$ in Fig. 4.7, and $\gamma=3\pi/4$ in Fig. 4.8. The temperature fields are shown as grey scale maps, and the velocity fields are shown by vectors whose length is proportional to the velocity. The absence of temperature data in Figs. 4.6 and 4.8 results from the limited usable camera area. Locations where no velocity vectors exist indicate either a velocity of 0 or an absence of data.

Figs. 4.6, 4.7, and 4.8 exhibit differences due entirely to the angle of inclination. Immediately after the transient boundary conditions are initiated, there is no fluid motion, and the thermal boundary layer grows by pure conduction, so that initially the temperature and velocity fields are independent of the angle of inclination. This is illustrated at 10 s from startup in Figs. 4.6(a), 4.7(a), and 4.8(a). As the thermal boundary layer continues to grow, it is accelerated by the tangential component relative to the wall of the buoyancy force. Since the normal component relative to the wall of the buoyancy force does not significantly affect the flow for $\pi/6 < \gamma < 5\pi/6$ (Bejan 1995), the temperature and velocity fields for the three angles of inclination are nearly identical and differ only in the apparent Rayleigh number. At 22 s the boundary layer has started to convect as shown in Figs. 4.6(b), 4.7(b), and 4.8(b).

Once the intrusion layer starts to cross the enclosure, the angle of inclination has a more pronounced effect. This is shown at 40 s in Figs. 4.6(c), 4.7(c), and 4.8(c). When $\gamma=\pi/4$, the intrusion layer is drawn across the enclosure as a buoyant jet. Since buoyancy

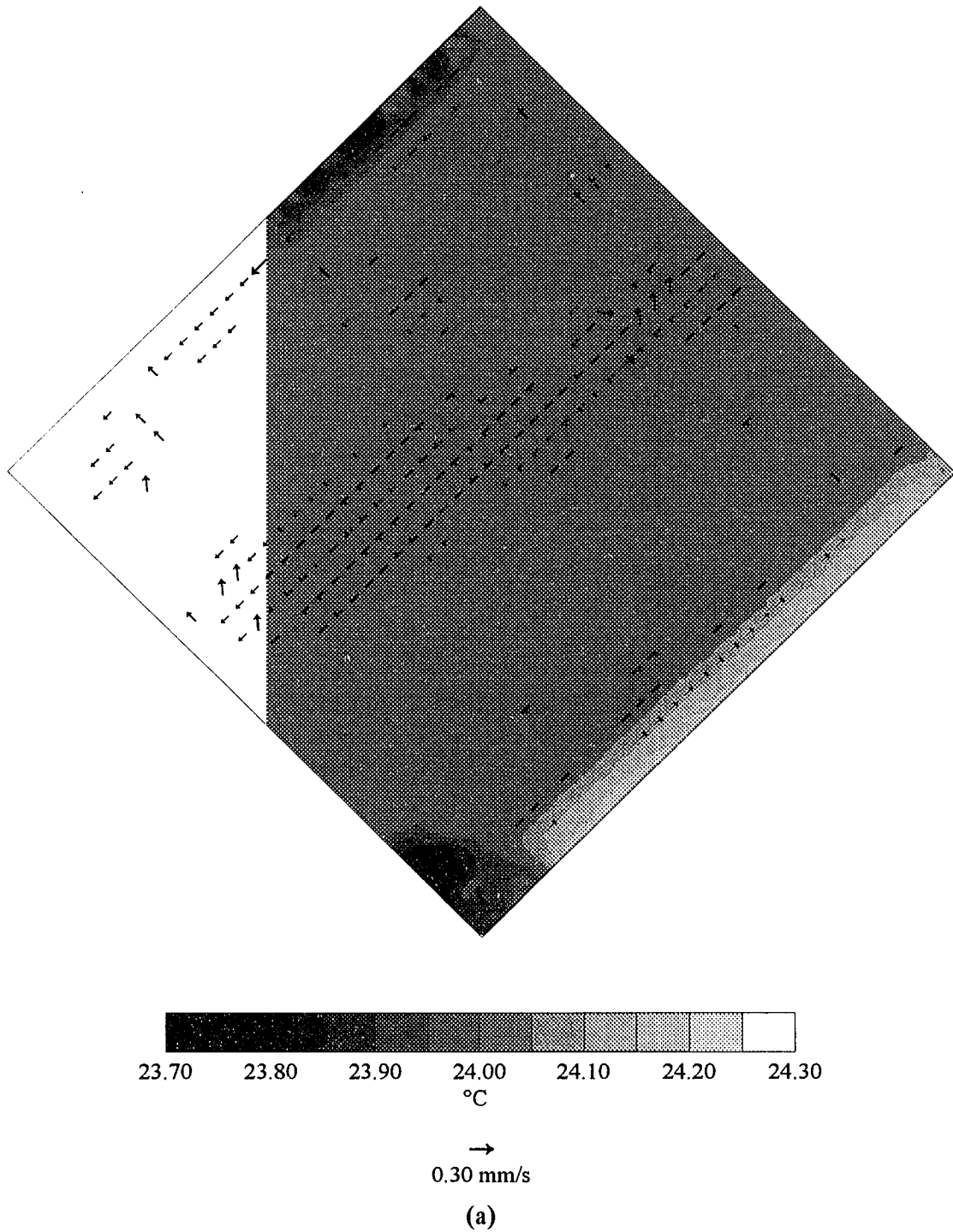
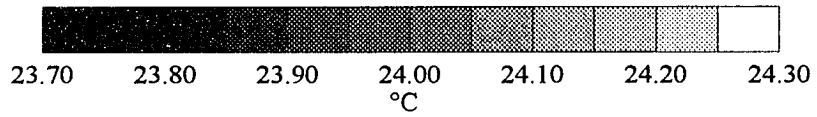
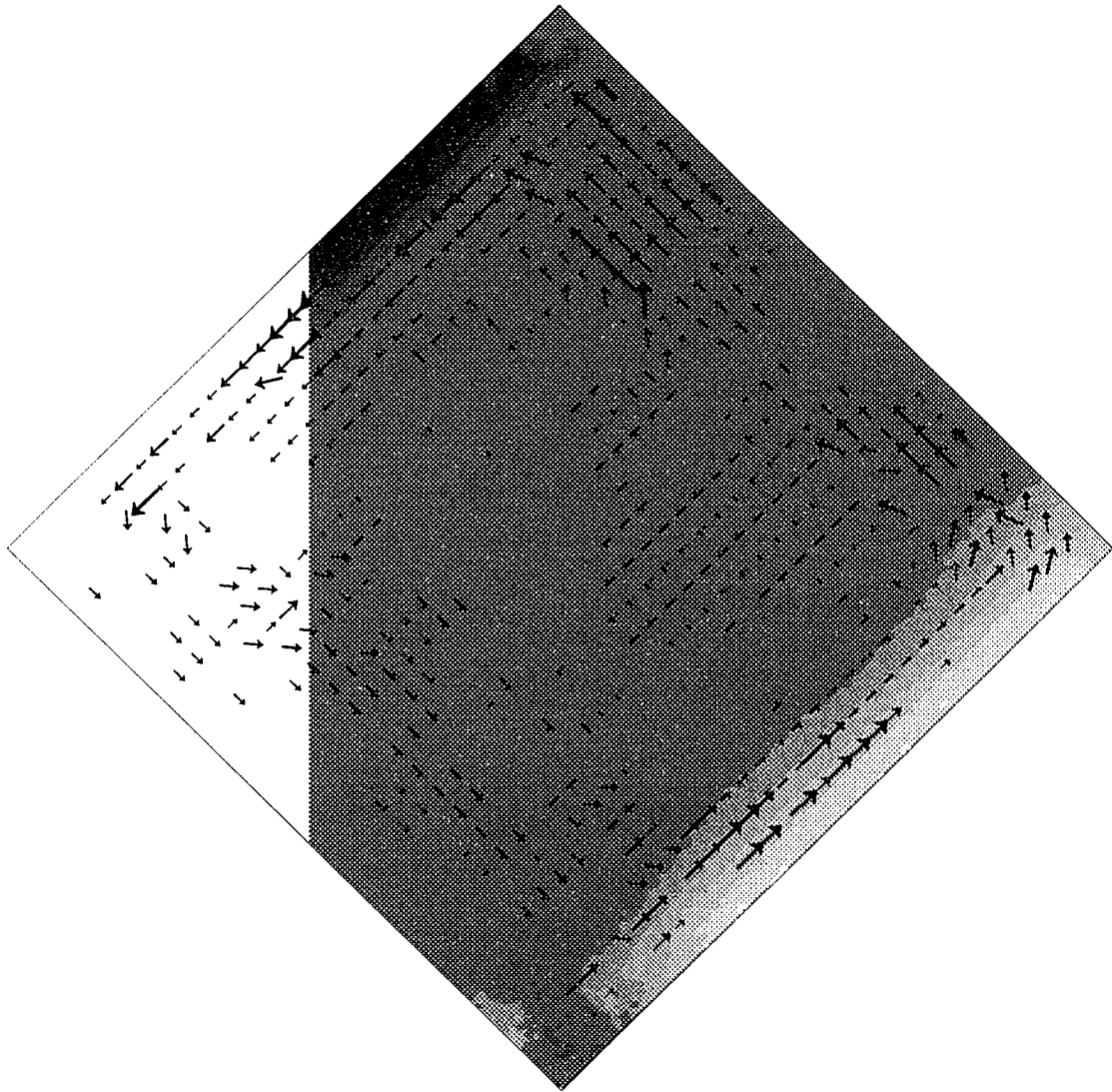
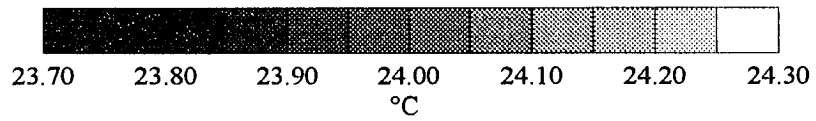
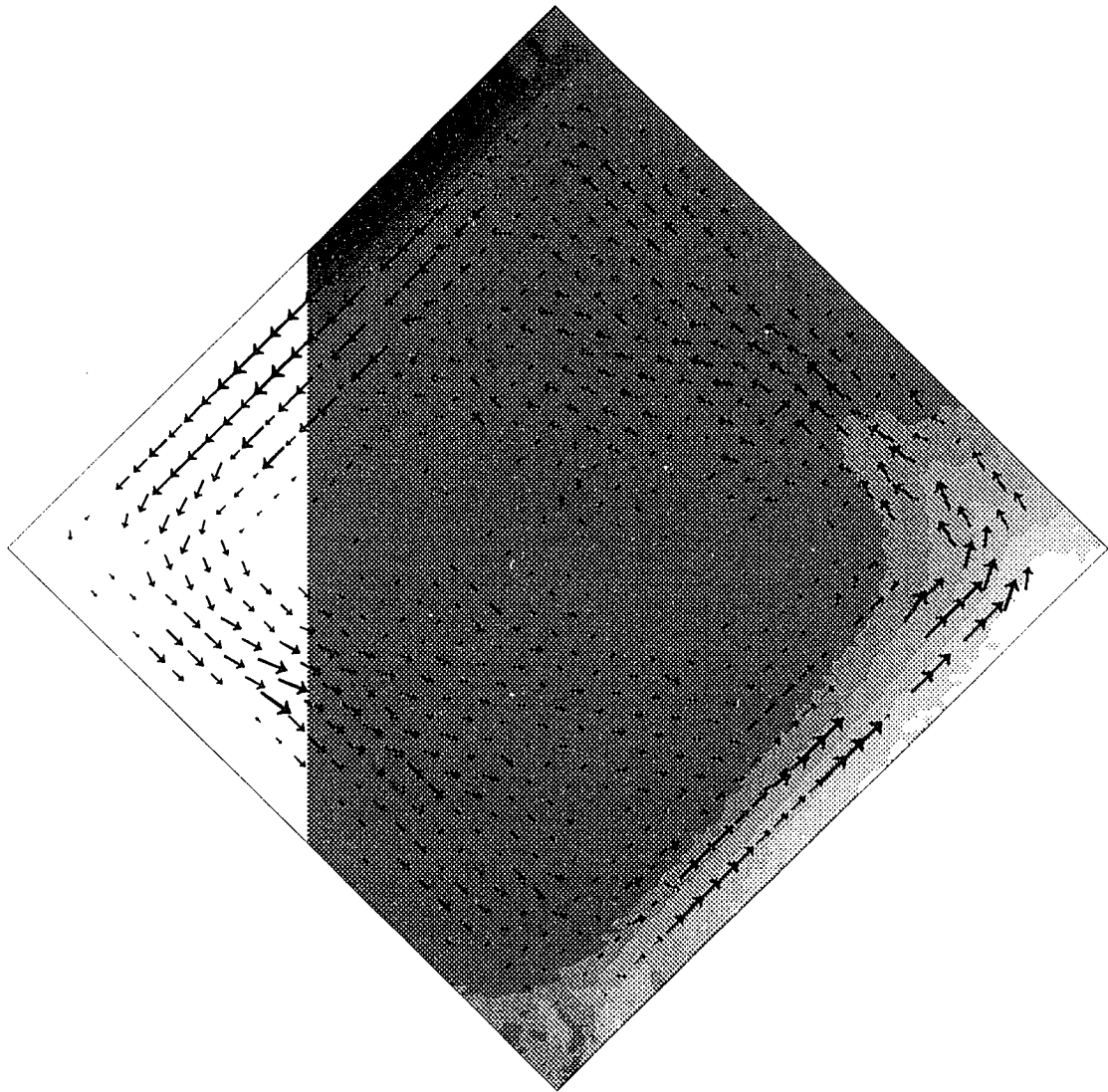


Fig. 4.6 Temperature and velocity fields during the evolution of the flow to steady state for $\gamma=\pi/4$: (a) $t=10$ s, (b) $t=22$ s, (c) $t=40$ s, (d) $t=75$ s, (e) $t=600$ s.



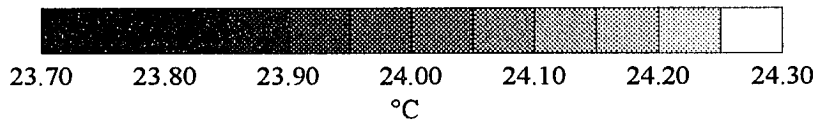
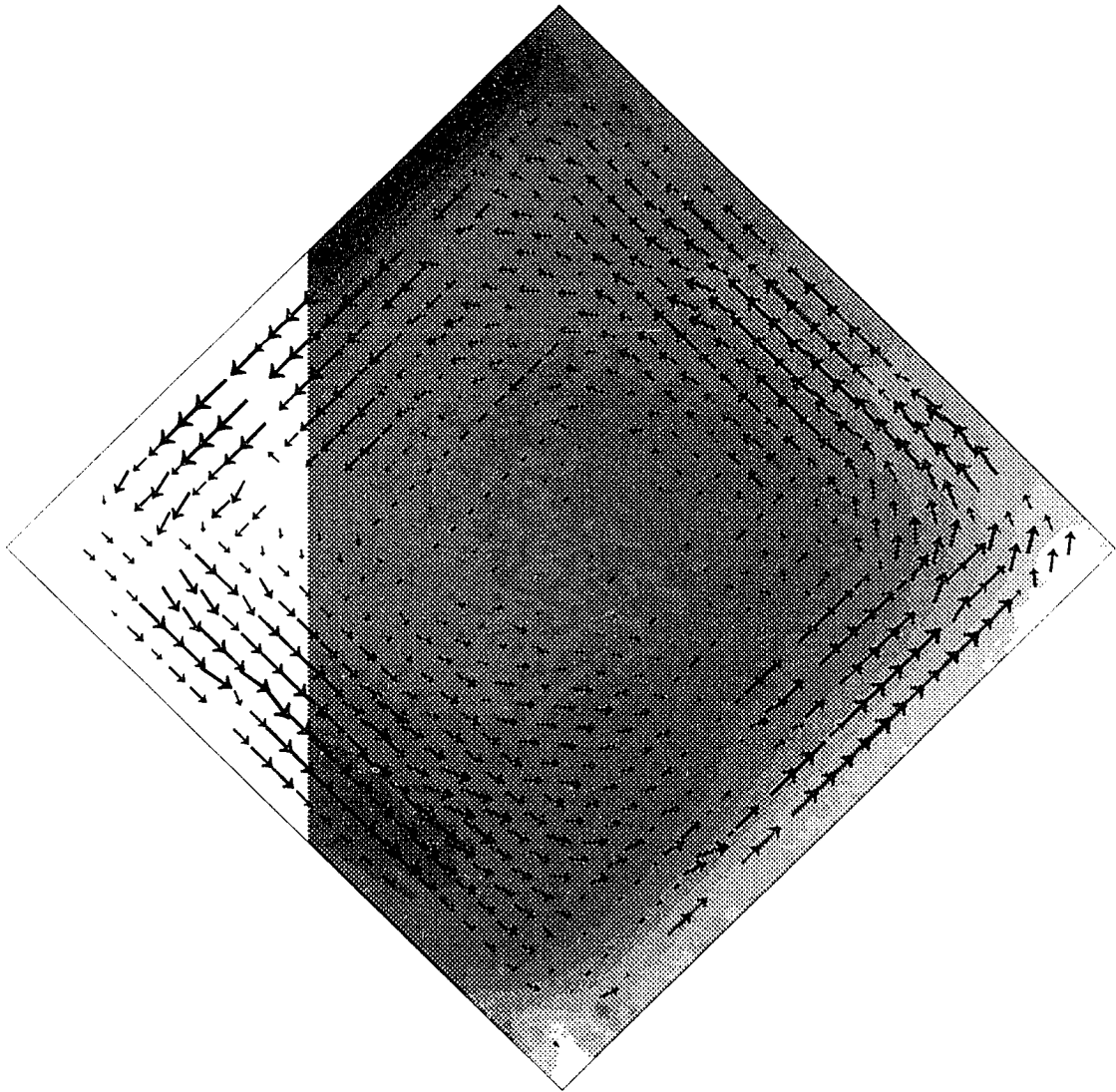
→
0.30 mm/s

(b)



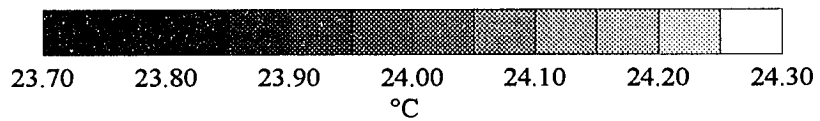
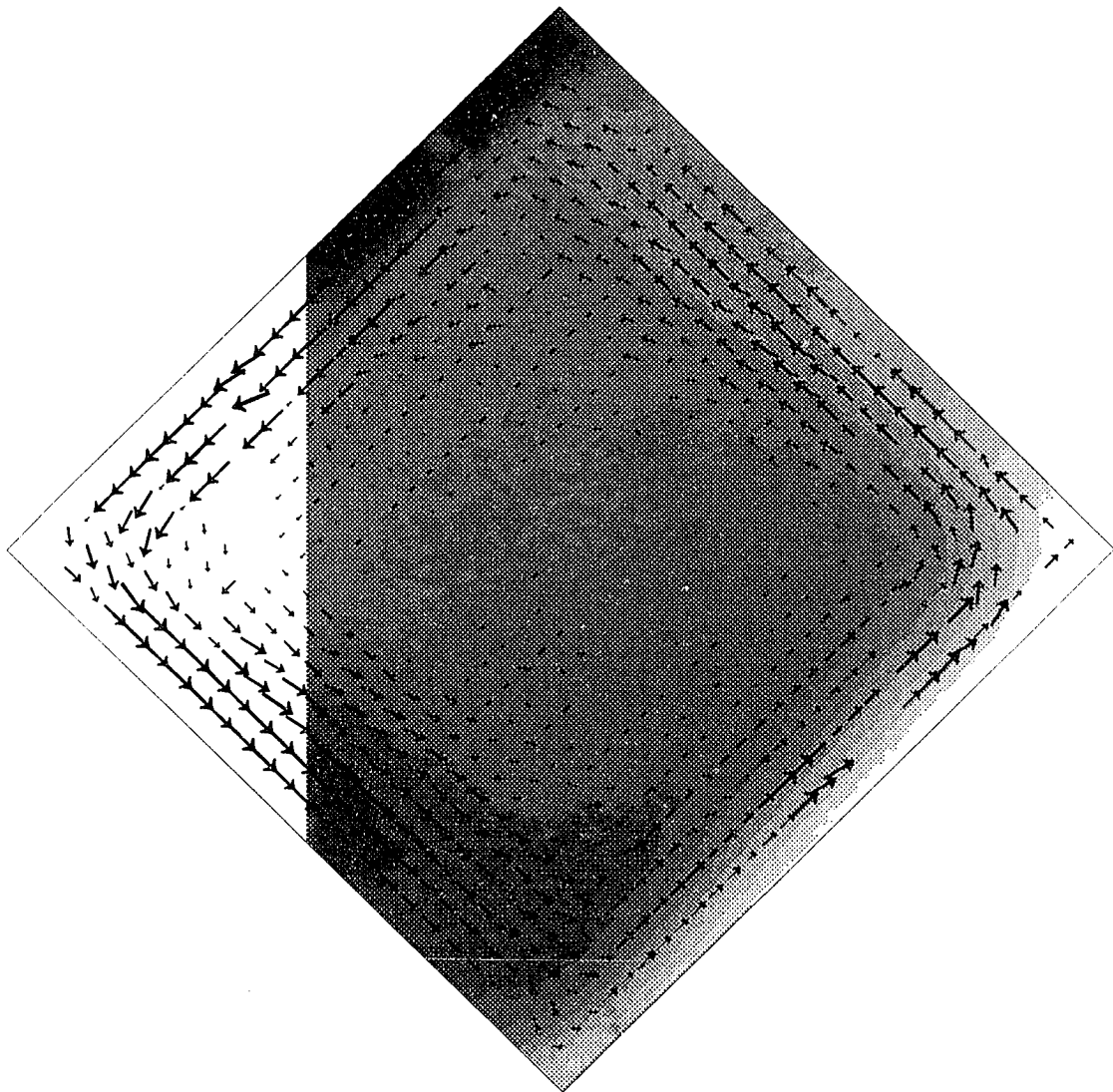
→
0.60 mm/s

(c)



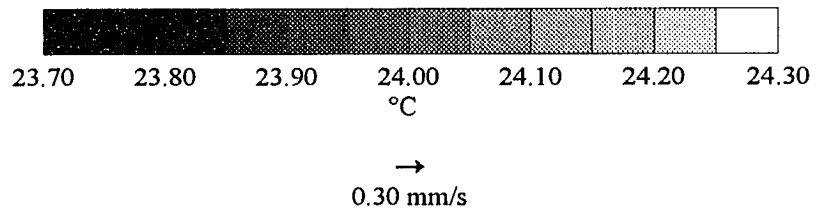
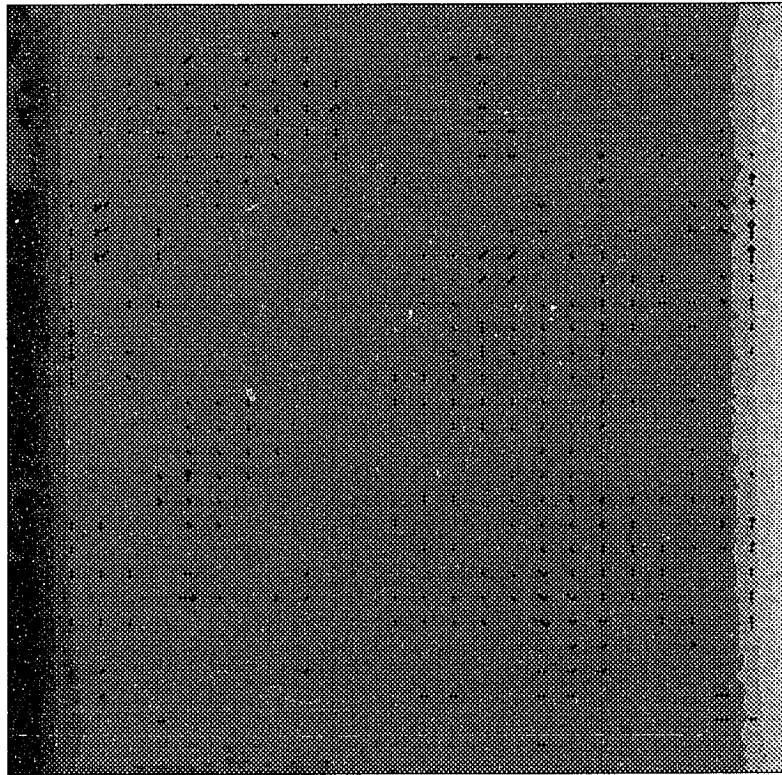
→
0.60 mm/s

(d)



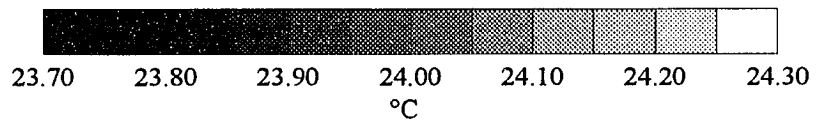
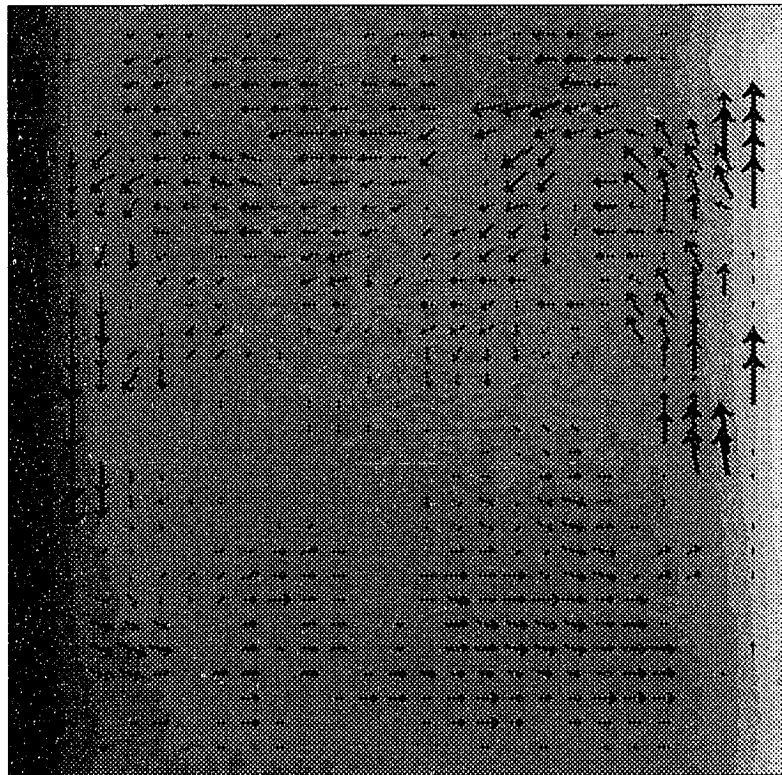
→
0.60 mm/s

(e)



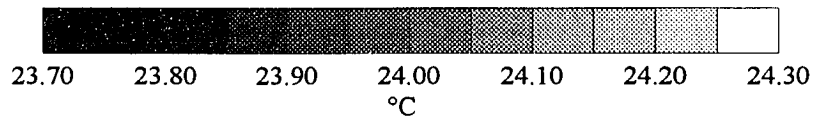
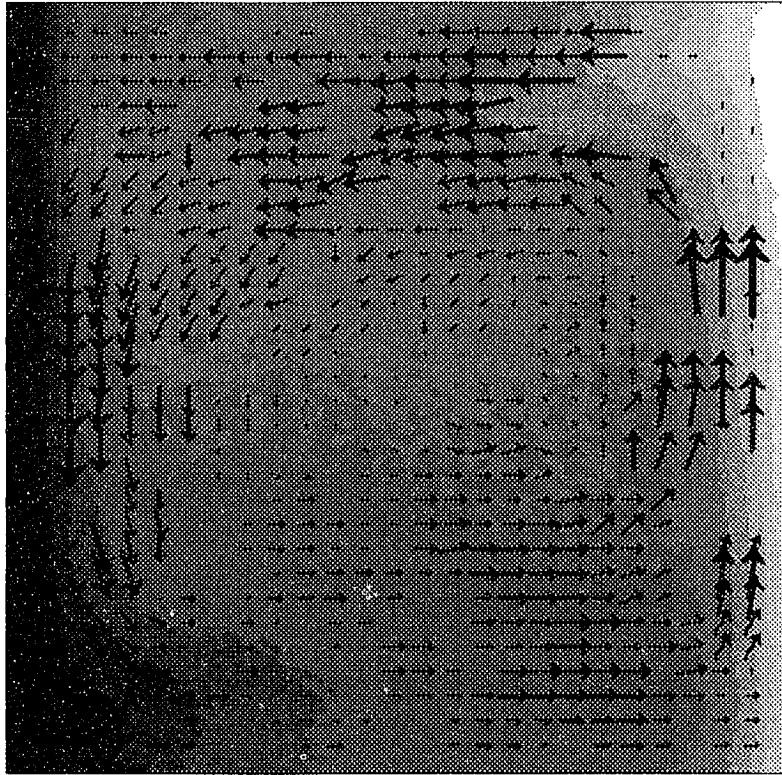
(a)

Fig. 4.7 Temperature and velocity fields during the evolution of the flow to steady state for $\gamma=\pi/2$: (a) $t=10$ s, (b) $t=22$ s, (c) $t=40$ s, (d) $t=75$ s, (e) $t=600$ s.



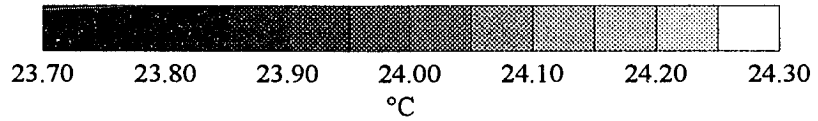
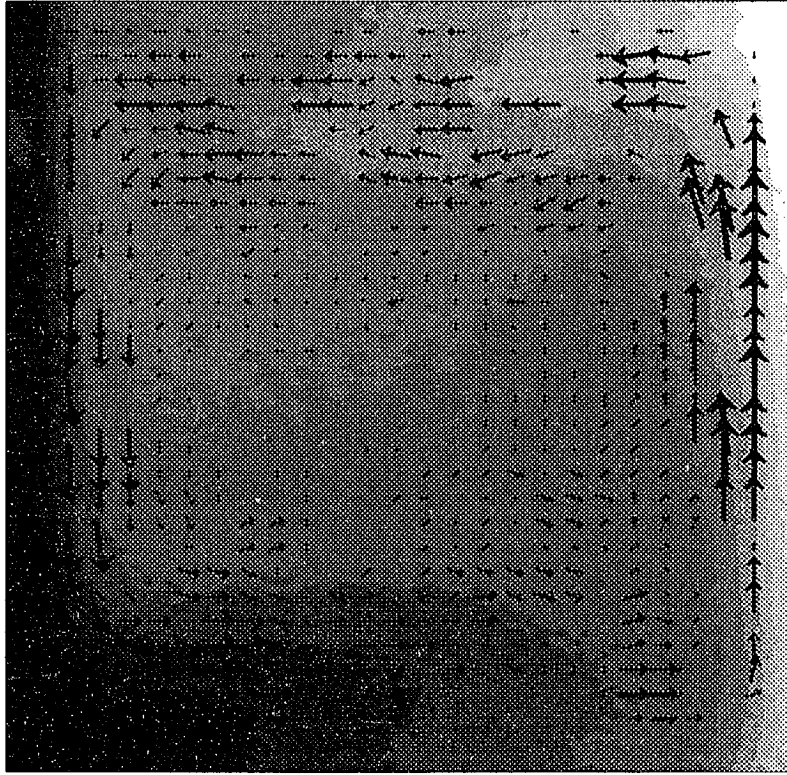
→
0.30 mm/s

(b)



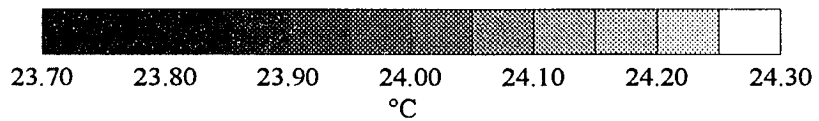
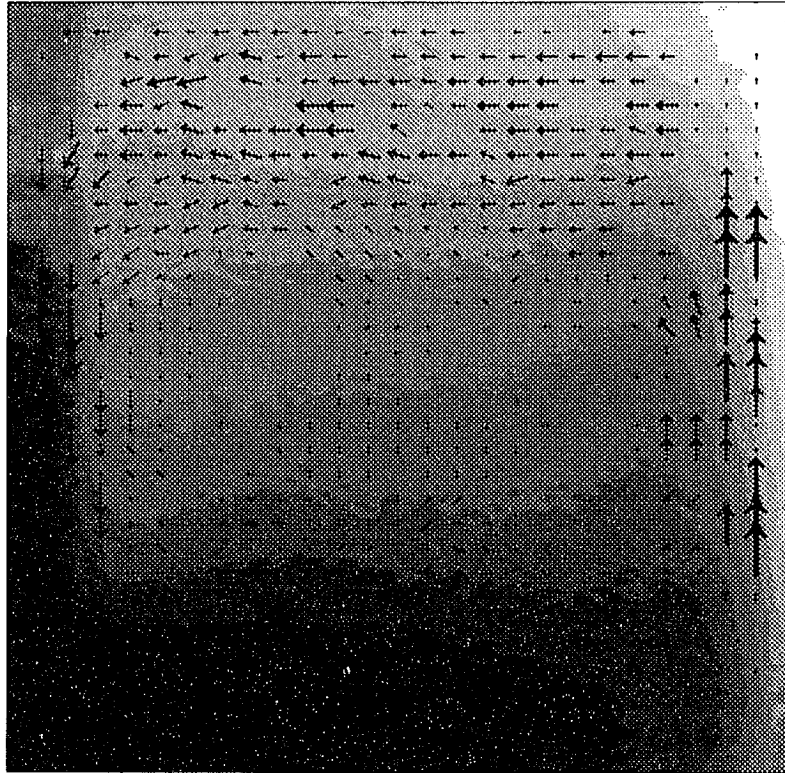
→
0.30 mm/s

(c)



→
0.30 mm/s

(d)



→
0.30 mm/s

(e)

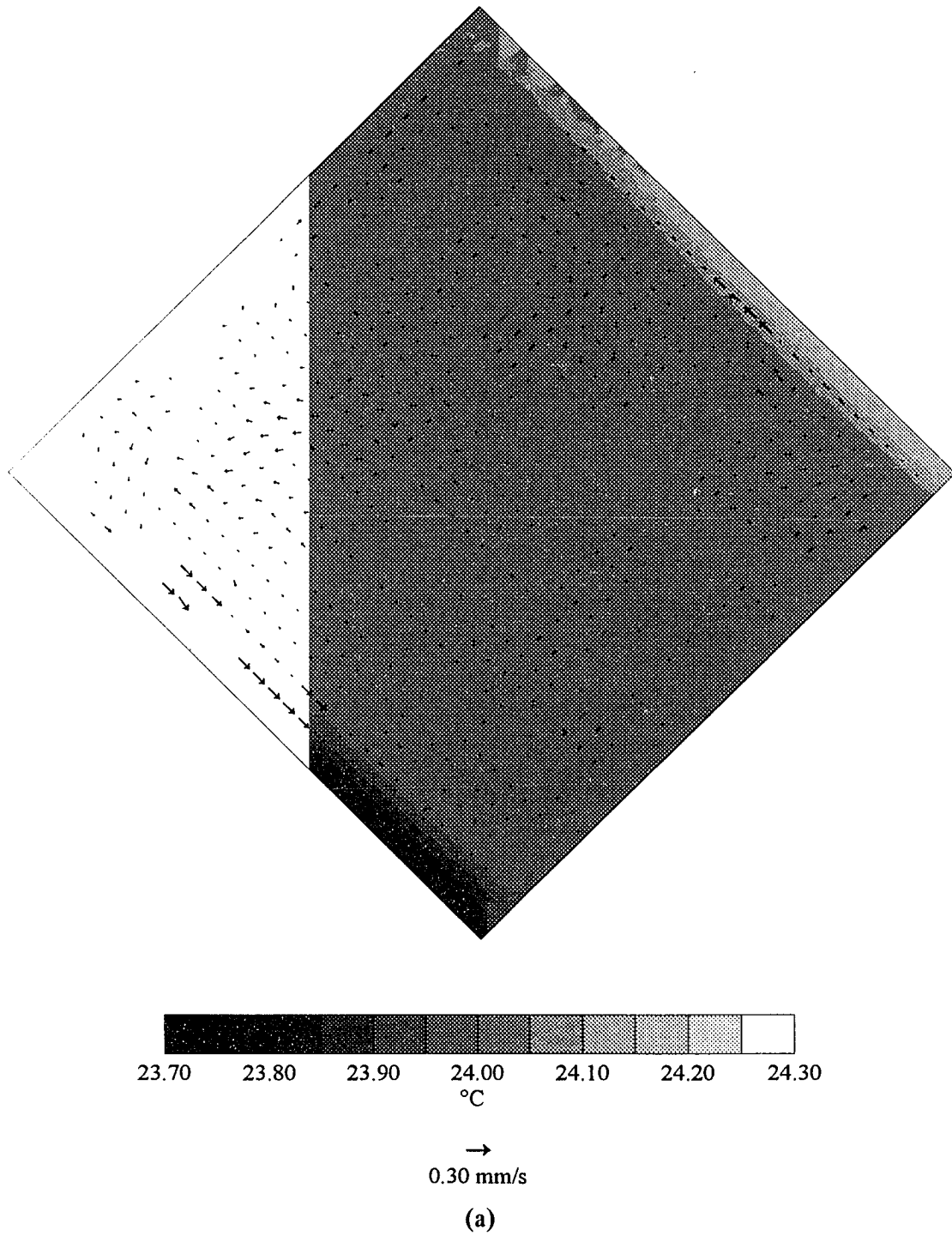
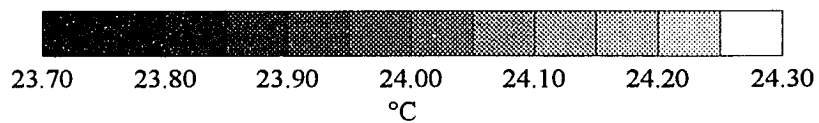
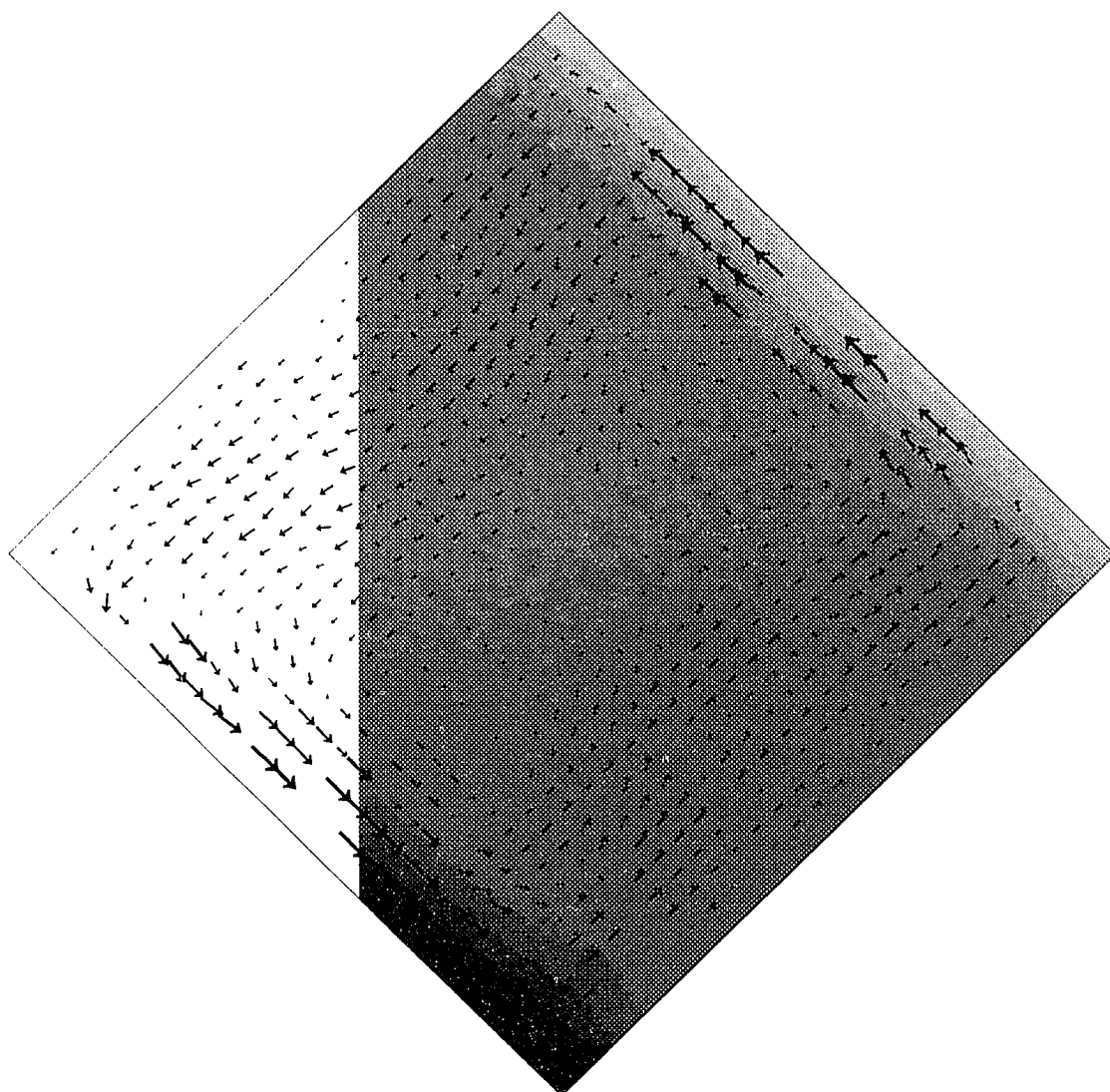
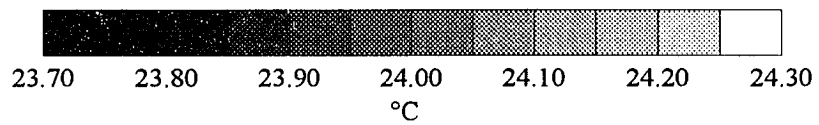
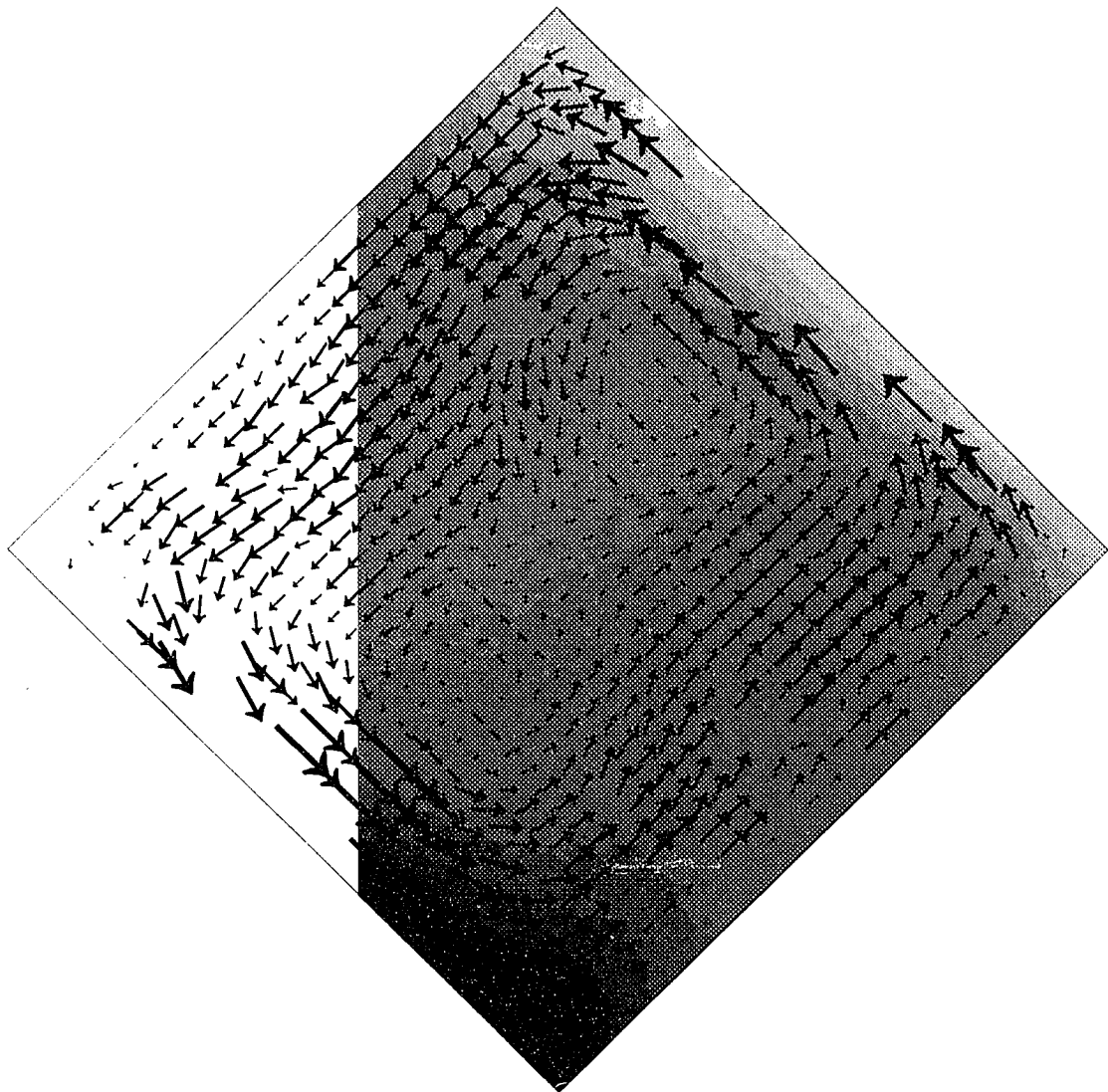


Fig. 4.8 Temperature and velocity fields during the evolution of the flow to steady state for $\gamma=3\pi/4$: (a) $t=10$ s, (b) $t=22$ s, (c) $t=40$ s, (d) $t=75$ s, (e) $t=600$ s.



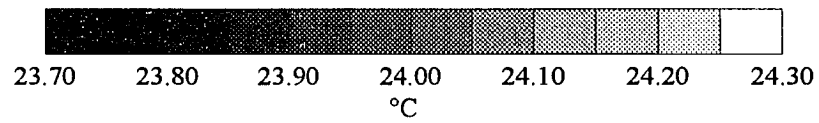
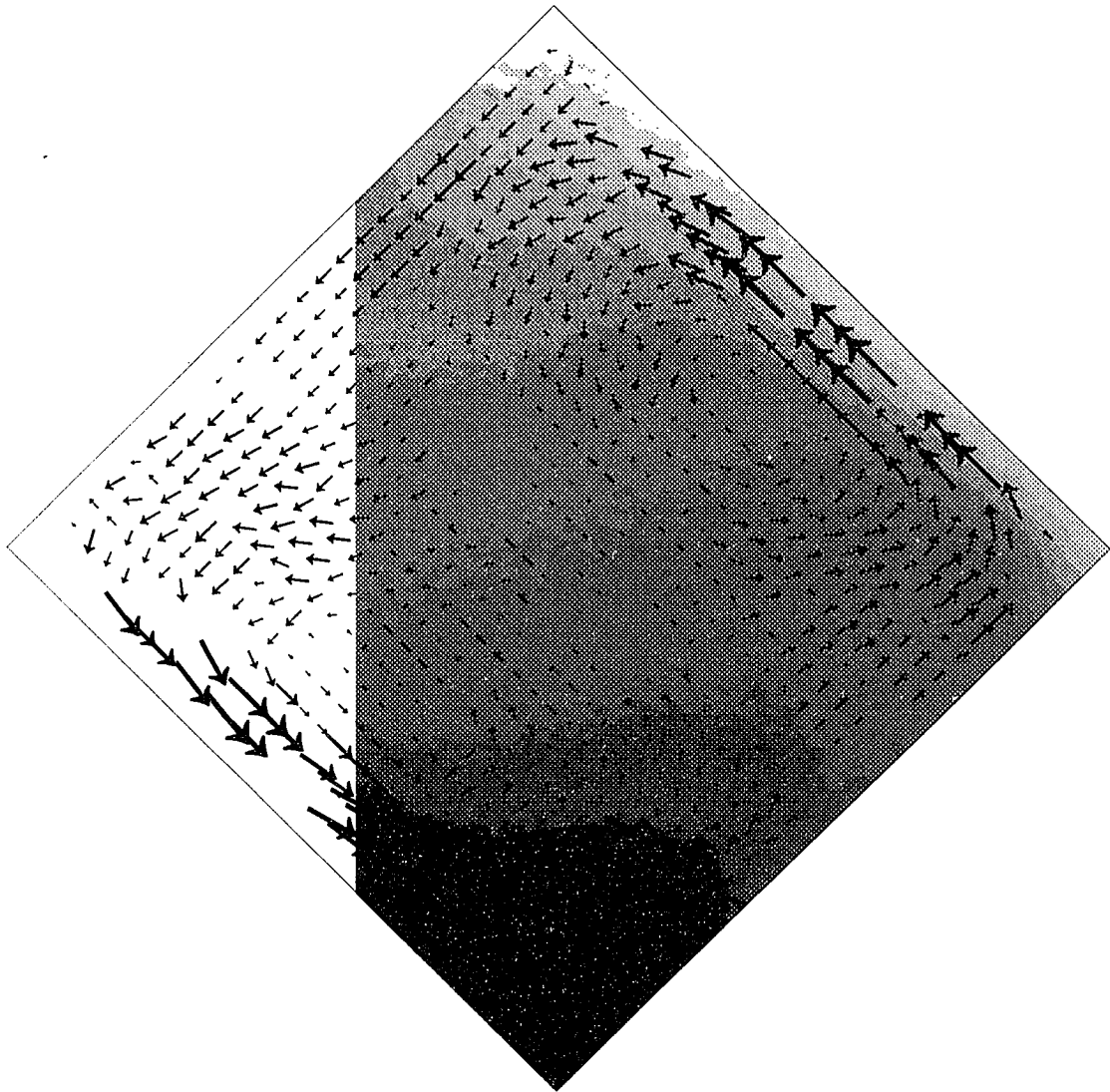
→
0.30 mm/s

(b)

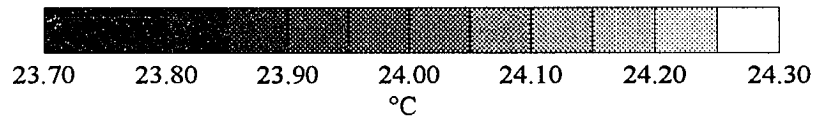
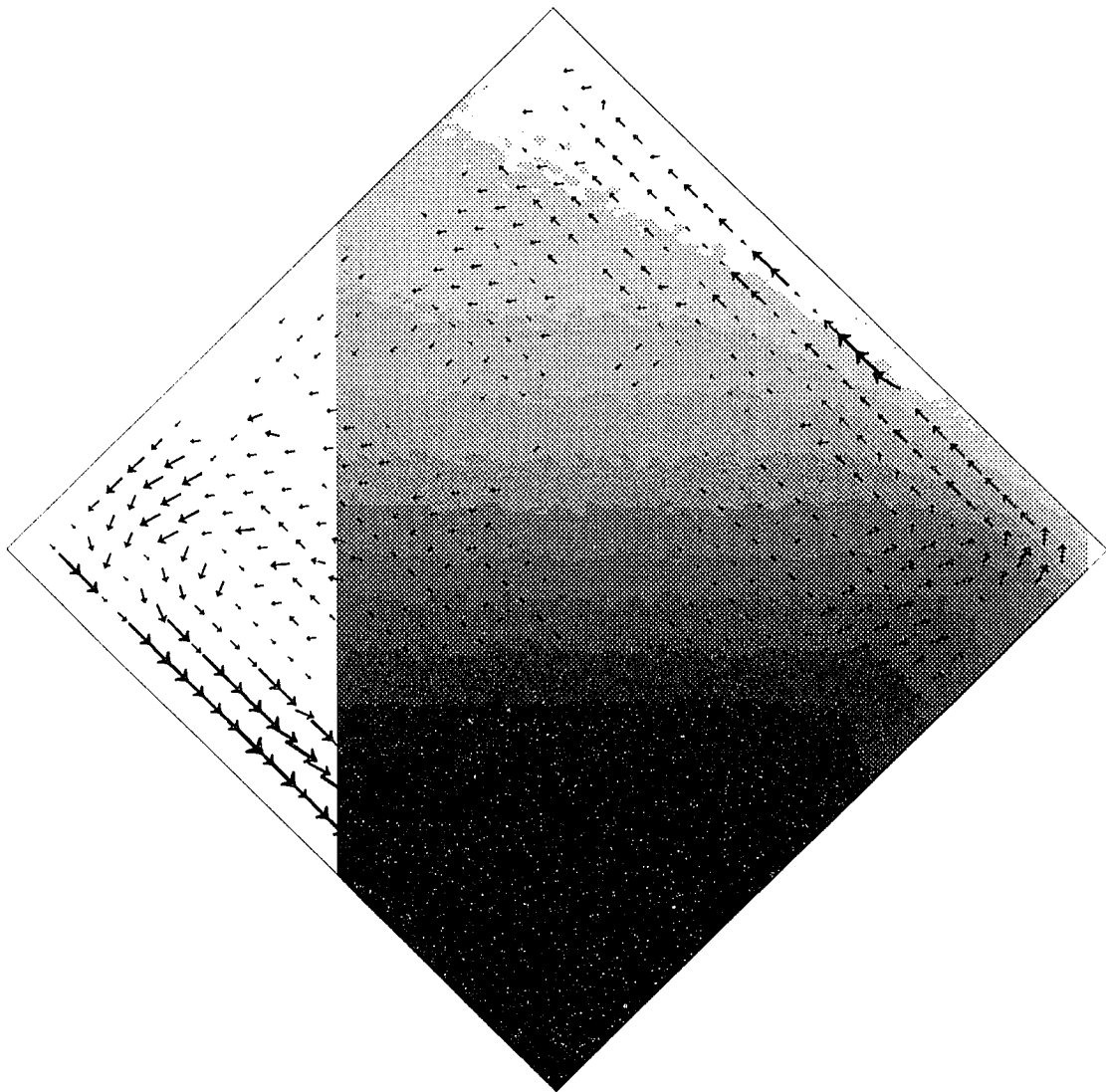


→
0.15 mm/s

(c)



→
0.15 mm/s
(d)



→
0.15 mm/s

(e)

acts along both the heated and insulated walls, there is more work done on the fluid by buoyancy, increasing the velocity. When $\gamma=\pi/2$, the intrusion layer is pushed across by the pressure force due to buoyancy in the boundary layer. When $\gamma=3\pi/4$, buoyancy and pressure oppose each other in the intrusion layer, decreasing the velocity. By 75 s the intrusion layer is well developed. When $\gamma=\pi/4$, buoyancy draws the heated fluid completely across the enclosure as shown in Fig. 4.6(d). When $\gamma=\pi/2$ or $\gamma=3\pi/4$, some of the fluid leaving the boundary layer does not cross the enclosure but instead is entrained back into the boundary layer as shown in Figs. 4.7(d) and 4.8(d). The amount of this entrainment depends on the angle of inclination and is larger for $\gamma=3\pi/4$. Kuyper et al. (1993) stated that for $\gamma \sim \pi$ most of the fluid leaving the heated or cooled wall returns to the same wall, forming a stretched cell along both walls. When $\gamma=\pi/2$ or $\gamma=3\pi/4$, the interior of the enclosure is filled by horizontal layering followed by the establishment of a primarily vertical temperature gradient as noted by Patterson and Imberger (1980).

The steady state temperature and velocity fields are shown in Figs. 4.6(e), 4.7(e), and 4.8(e). When $\gamma=\pi/4$, the interior of the enclosure is well mixed, and the temperature gradients are small. The current results are consistent with the results of Hamady et al. (1989) and Kuyper et al. (1993) who showed for similar angles of inclination a single convection cell. Kuyper et al. (1993) stated that the flow in the interior of the enclosure pushes the flow along the adiabatic walls to the side, breaking up the temperature stratification. When $\gamma=\pi/2$, a stably stratified vertical temperature gradient exists in the interior of the enclosure. The flow is dominated by a single convection cell, with the primary flow parallel to the isotherms. However, a smaller cell exists near each of the

heated and cooled boundaries. The current results agree with those of Hamady et al. (1989) and Kuyper et al. (1993) and show that the cells move to a downstream location in the boundary layer. When $\gamma=3\pi/4$, the flow consists of a double convection cell. Similar to when $\gamma=\pi/2$, a stably stratified vertical temperature gradient exists in the interior of the enclosure. Both Hamady et al. (1989) and Kuyper et al. (1993) state that this is a conduction dominated flow. This is apparent from the fact that the flow is confined to the boundary layers with the heated and cooled fluid positioned in the upper and lower corners of the enclosure, respectively. When $\gamma=\pi/4$, the velocity at steady state is nearly the maximum velocity. However, for $\gamma=\pi/2$ or $\gamma=3\pi/4$, the velocity at steady state is much less than the velocity during startup.

The time and length scales estimated from the velocity and temperature data are compared to those found using scale analysis in Table 4.1. The time and length scales

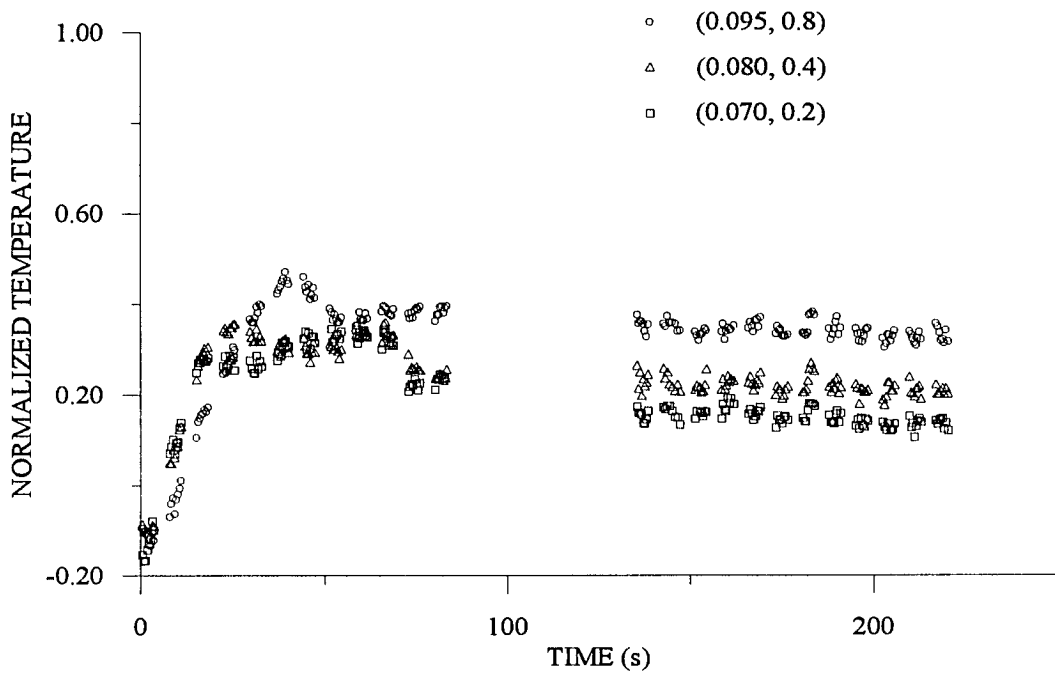
Table 4.1 Time and length scales estimated by scaling and experiment.

ANGLE OF INCLINATION	METHOD	δ_T (mm)	τ (s)	v (mm/s)	δ_v (mm)	Δ_v (mm)	T_v (s)
$\gamma=\pi/4$	SCALING	1.7	19	1.5	4.2	1.7	19
	EXPERIMENT	4.0	22	0.4	6.4	5.8	34
$\gamma=\pi/2$	SCALING	1.5	16	1.8	3.9	3.2	34
	EXPERIMENT	3.9	18	0.6	6.4	9.4	38
$\gamma=3\pi/4$	SCALING	1.7	19	1.5	4.2	1.7	19
	EXPERIMENT	3.7	22	0.4	6.4	12	36

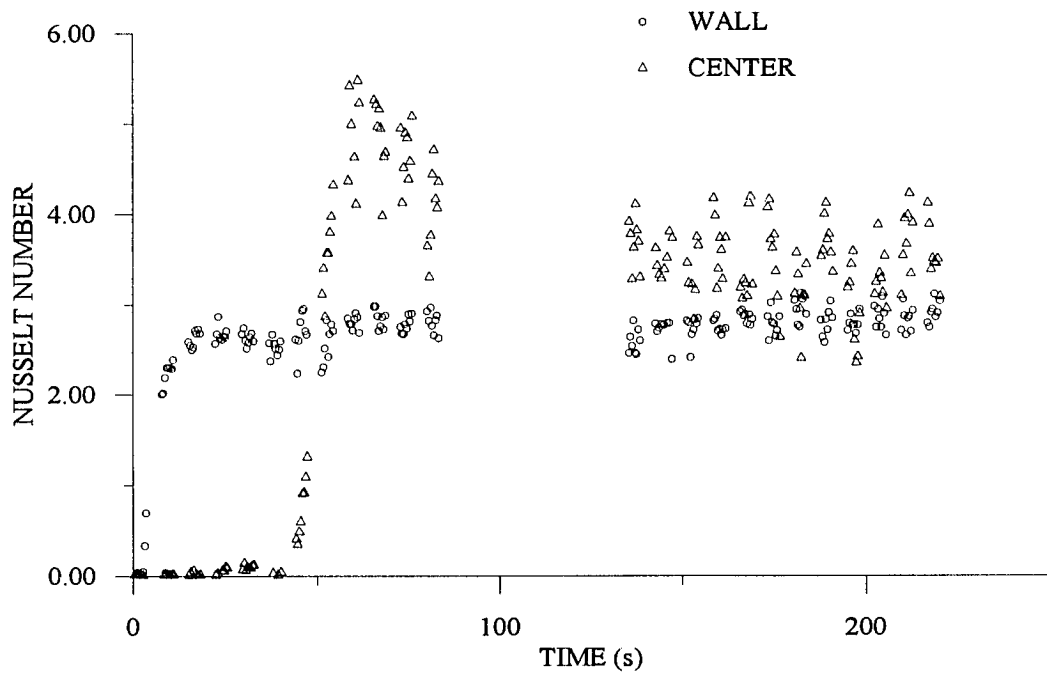
estimated by scaling and experiment exhibit similar trends with the angle of inclination. As

the apparent Rayleigh number decreases, the growth time of the thermal boundary layer increases, and the velocity in the thermal boundary layer decreases. The experimental results for the intrusion layer also exhibit the trends predicted by scale analysis. An exception to this is the thickness scale for a viscous intrusion layer for $\gamma=3\pi/4$. When $\gamma=3\pi/4$, buoyancy and pressure oppose each other in the intrusion layer, and the order of magnitude assumptions made for the intrusion layer are no longer valid, since the pressure force is not small compared to the buoyancy force.

The temperature in the boundary layer and the Nusselt number at the wall and center of the enclosure as a function of time are shown for $\gamma=\pi/4$ in Fig. 4.9, $\gamma=\pi/2$ in Fig. 4.10, and $\gamma=3\pi/4$ in Fig. 4.11. The temperature is normalized by $(T-T_0)/\Delta T$, and the locations in the boundary layer are normalized by $(x/W, y/H)$. The absence of data around 100 s occurs during data storage. The occurrence of either the two boundary layer oscillations or the whole cavity oscillations is not clearly indicated. The period of the two boundary layer oscillations is $T=27$ s, and the period of the whole cavity oscillations is $T\sim 56$ s, so the time resolution is high enough to resolve both transient oscillations. There does appear to be an overshoot in the temperature in the boundary layer and a damped oscillation in the Nusselt number at the center of the enclosure for $\gamma=\pi/4$ as shown in Fig. 4.9, even though the uncertainty in the Nusselt number at the center of the enclosure is on the order of the magnitude of the oscillations (Patterson and Imberger 1980; Schladow 1990; Paterson and Armfield 1990). A slight dip in the Nusselt number at the wall of the enclosure is also observed at the initiation of the damped oscillation. The current results for $\gamma=\pi/4$ are consistent with the numerical results Patterson and Imberger (1980) made

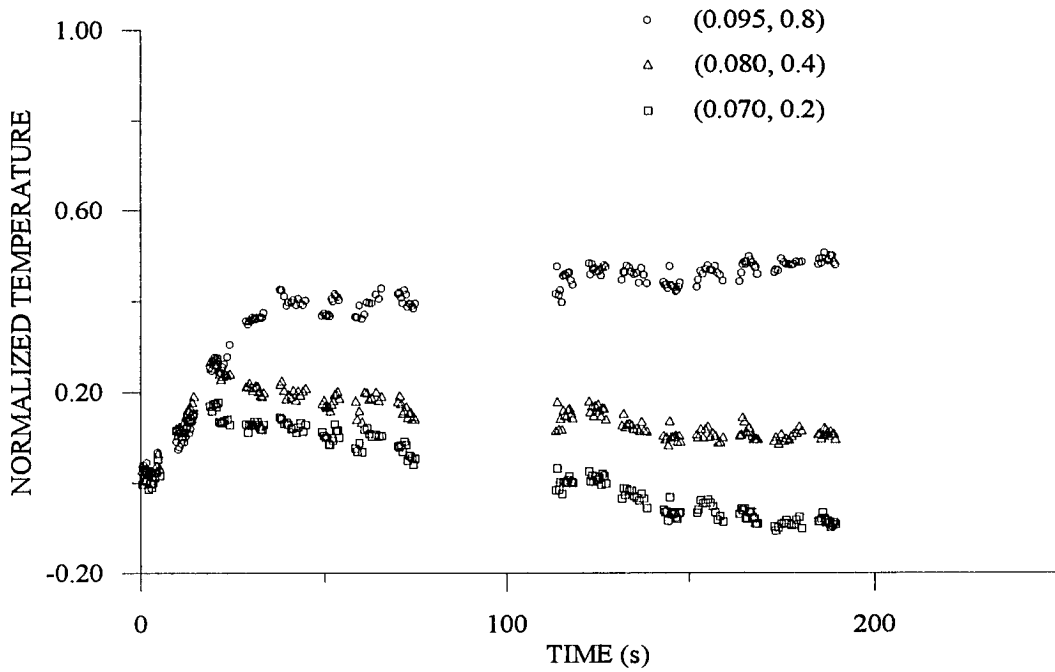


(a)

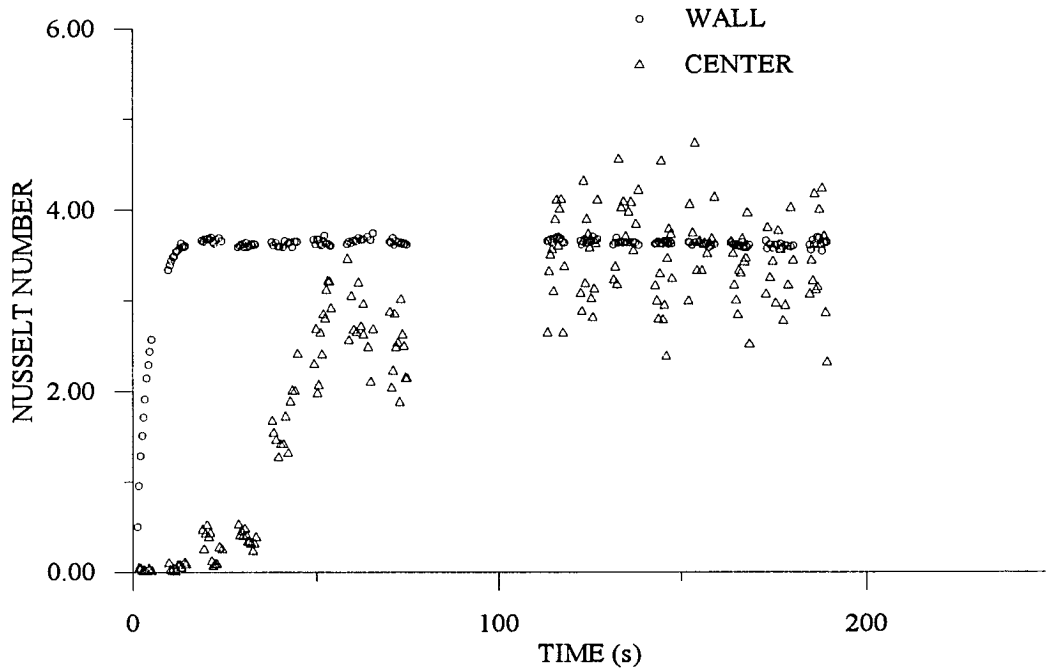


(b)

Fig. 4.9 (a) Temperature in the boundary layer and (b) Nusselt number at the wall and center of the enclosure for $\gamma = \pi/4$.

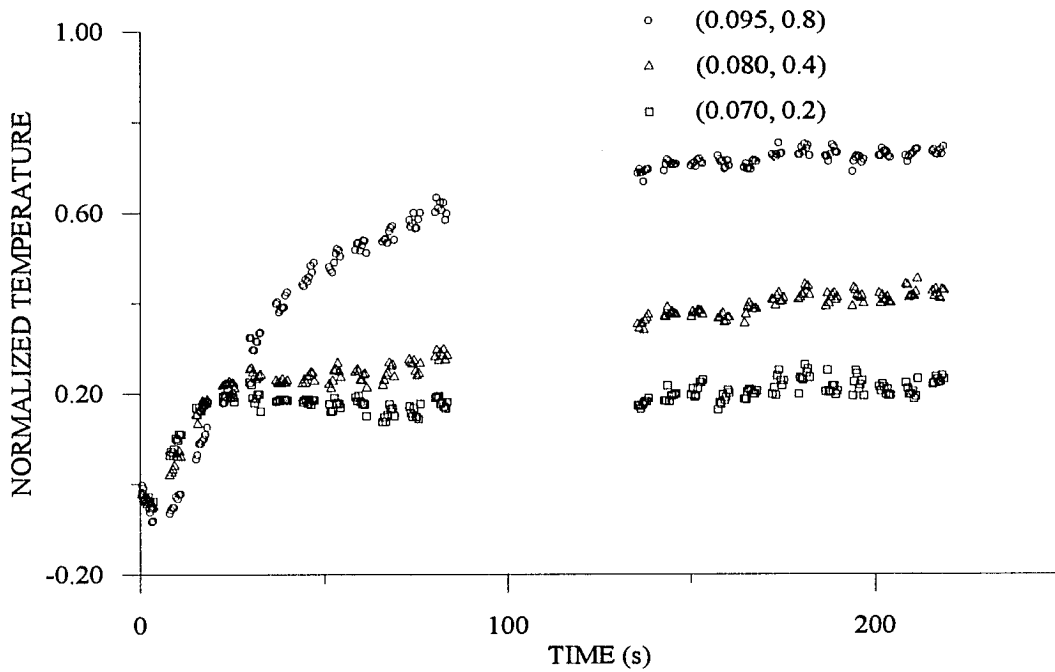


(a)

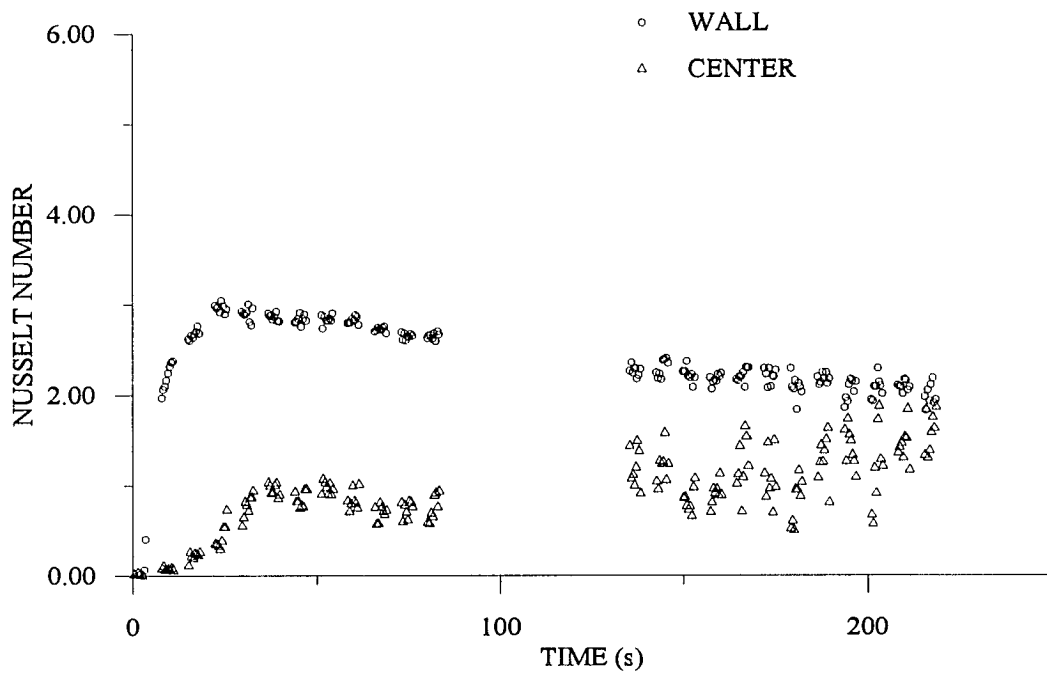


(b)

Fig. 4.10 (a) Temperature in the boundary layer and (b) Nusselt number at the wall and center of the enclosure for $\gamma = \pi/2$.



(a)



(b)

Fig. 4.11 (a) Temperature in the boundary layer and (b) Nusselt number at the wall and center of the enclosure for $\gamma=3\pi/4$.

for a flow with $Pr=7$, $Ra=1.4 \times 10^4$, $A=1.0$, and $\gamma=\pi/2$, in which they show a single damped oscillation. However, the temperature and velocity fields compare better with the results Patterson and Imberger (1980) made for a flow with $Pr=7$, $Ra=1.4 \times 10^5$, $A=1.0$, and $\gamma=\pi/2$. When $\gamma=\pi/4$, there is a rapid growth in the Nusselt number at the center of the enclosure, as the heated fluid crosses the enclosure. When $\gamma=\pi/2$, most of the fluid leaving the heated wall reaches the cooled wall. When $\gamma=3\pi/4$, the flow is confined to the boundary layers and the Nusselt number grows slowly as the heat transfer is diffusion dominated.

Experimental considerations including fluid properties and boundary conditions may have affected the results. Differences in the fluid properties may have resulted from temperature variation and the addition of sodium bicarbonate. The temperature difference was $0.3 \text{ }^\circ\text{C}$, and sodium bicarbonate was added to bring the density to 1.02 kg/m^3 . Differences in the boundary conditions may have resulted from the finite time required to bring the heated and cooled walls to temperature, heat transfer through the adiabatic walls, and the effect of two end walls. The initiation time was 2.0 s , an order of magnitude less than the growth time scale of the boundary layer; the heat transfer through the adiabatic walls was negligible, evident in the temperature gradient normal to the adiabatic walls as shown in Figs. 4.6, 4.7, and 4.8; and the length of enclosure was twice the height. These differences, especially the finite initiation time, may have a stabilizing effect on the flow.

4.3 Conclusions

The angle of inclination was shown to have a significant effect on the flow and heat transfer in natural convection in an enclosure. Buoyancy in the intrusion layer was found to be the main factor determining the character of these flows. The scale analysis for transient natural convection in enclosures was extended to inclined enclosures and compared to the experimental results. The expected transient oscillations were not evident. The results for the temperature in the boundary layer and the Nusselt number at the wall and center of the enclosure have the appearance that they were produced by a lower Rayleigh number flow. This is probably due to differences in the boundary conditions at startup between the current experiments and the numerical simulations.

4.4 Future work

The Rayleigh number is critical in determining the magnitude and frequency of the transient oscillations. It would be extremely desirable to perform the current experiments at $Ra \sim 10^8$. This Rayleigh number is of the same order as that used by Schladow (1990) and Patterson and Armfield (1990). At this Rayleigh number the magnitude of the transient oscillations is significant.

Optical considerations placed a major constraint on the magnitude of the Rayleigh number in the current experiments. Eq. (4.3) indicates that the Rayleigh number is directly proportional to ΔT and H^3 . Increasing either ΔT or H not only increases the Rayleigh

number but also increases refraction errors. Eq. (4.37) indicates that ΔT is inversely proportional to H . If H is increased, ΔT must be decreased to remain in the refractionless limit. In the current experiments the temperature difference was limited to $\Delta T < 0.47$ °C. Temperature differences smaller than this are not practical, since the accuracy of the ΔT measurement is on the order of ± 0.05 °C.

Using air instead of water reduces refraction errors and allows for higher Rayleigh numbers. However, the particle seeding necessary for DPIV is considerably more difficult for air than water. Aerosols are typically used as seed particles for air. These particles work only for high speed flows where drift velocity is not significant. In the low speed flow of the current experiments neutrally buoyant particles are required.

References

- Armfield, S. W.; Patterson, J. C. 1992: Wave properties of natural-convection boundary layers. *J. Fluid Mech.* **239**, 195-211.
- Bejan, A. 1995: *Convection Heat Transfer*. New York: John Wiley and Sons, 18-21, 194-196, 219-267.
- Briggs, D. G.; Jones, D. N. 1985: Two-dimensional periodic natural convection in a rectangular enclosure of aspect ratio one. *J. Heat Trans.* **107**, 850-854.
- Figliola, R. S.; Beasley, D. E. 1995: *Theory and Design for Mechanical Measurements*. New York: John Wiley and Sons, 269-278.
- Fusegi, T.; Hyun, J. M.; Kuwahara, K. 1991: Transient three-dimensional natural convection in a differentially heated cubic enclosure. *Int. J. Heat Mass Trans.* **34**, 1559-1564.

- Gebhart, B.; Mahajan, R. L. 1982: Instability and transition in buoyancy induced flows. *Adv. Appl. Mech.* **22**, 231-315.
- Hall, J. D.; Bejan, A.; Chaddock, J. B. 1988: Transient natural convection in a rectangular enclosure with one heated side wall. *Int. J. Heat Fluid Flow* **9**, 396-404.
- Hamady, F. J.; Lloyd, J. R.; Yang, H. Q.; Yang, K. T. 1989: Study of local natural convection heat transfer in an inclined enclosure. *Int. J. Heat Mass Trans.* **32**, 1697-1708.
- Hiller, W. J.; Koch, St.; Kowalewski, T. A.; Stella, F. 1993: Onset of natural convection in a cube. *Int. J. Heat Mass Trans.* **36**, 3251-3263.
- Holman, J. P. 1989: *Experimental Methods for Engineers*. New York: McGraw-Hill, 41-47.
- Ivey, G. N. 1984: Experiments on transient natural convection in a cavity. *J. Fluid Mech.* **144**, 389-401.
- Kreith, F.; Bohn, M. S. 1993: *Principles of Heat Transfer*. St. Paul: West, 119-148, 264-279.
- Kuyper, R. A.; van der Meer, TH. H.; Hoogendoorn, C. J.; Henkes, R. A. W. M. 1993: Numerical study of laminar and turbulent natural convection in an inclined square cavity. *Int. J. Heat Mass Trans.* **36**, 2899-2911.
- Papanicolaou, E.; Jaluria, Y. 1992: Transition to a periodic regime in mixed convection in a square cavity. *J. Fluid Mech.* **239**, 489-509.
- Patterson, J.; Imberger, J. 1980: Unsteady natural convection in a rectangular cavity. *J. Fluid Mech.* **100**, 65-86.
- Patterson, J. C.; Armfield, S. W. 1990: Transient features of natural convection in a cavity. *J. Fluid Mech.* **219**, 469-497.
- Powell, R. L. 1976: Thermocouple thermometry. In *Measurements in Heat Transfer* (eds. E. R. G. Eckert; R. Goldstein). New York: McGraw-Hill, 105-162.
- Schladow, S. G. 1990: Oscillatory motion in a side-heated cavity. *J. Fluid Mech.* **213**, 589-610.
- Vest, C. M. 1979: *Holographic Interferometry*. New York: John Wiley and Sons, 329-334.

Winters, K. H. 1987: Hopf bifurcation in the double-glazing problem with conducting boundaries. *J. Heat Trans.* **109**, 894-898.

Yamane, T. 1967: *Statistics; An Introductory Analysis*. New York: Harper and Row, 339-344, 368-430.

Yih, C. -S. 1977: *Fluid Mechanics*. Ann Arbor: West River Press, 225-236.

LIST OF REFERENCES

- Adrian, R. J. 1984: Scattering particle characteristics and their effect on pulsed laser measurements of fluid flow: speckle velocimetry vs particle image velocimetry. *Appl. Opt.* **23**, 1690-1691.
- Adrian, R. J.; Yao, C. S. 1985: Pulsed laser technique application to liquid and gaseous flows and the scattering power of seed materials. *Appl. Opt.* **24**, 44-52.
- Adrian, R. J. 1986: Image shifting technique to resolve directional ambiguity in double-pulsed velocimetry. *Appl. Opt.* **25**, 3855-3858.
- Adrian, R. J. 1991a: Particle-imaging techniques for experimental fluid mechanics. *Annu. Rev. Fluid Mech.* **23**, 261-304.
- Adrian, R. J. 1991b: Optical instrumentation for measurement of fluid velocity fields. In *Fluids Engineering* (eds. J. H. Kim; J. M. Hyun; C. -O. Lee). New York: Hemisphere, 311-329.
- Armfield, S. W.; Patterson, J. C. 1992: Wave properties of natural-convection boundary layers. *J. Fluid Mech.* **239**, 195-211.
- Barker, D. B.; Fourney, M. E. 1977: Measuring fluid velocities with speckle patterns. *Opt. Lett.* **1**, 135-137.
- Bejan, A. 1995: *Convection Heat Transfer*. New York: John Wiley and Sons, 18-21, 194-196, 219-267.
- Bracewell, R. 1965: *The Fourier Transform and Its Applications*. New York: McGraw-Hill, 24-48, 241-250.
- Briggs, D. G.; Jones, D. N. 1985: Two-dimensional periodic natural convection in a rectangular enclosure of aspect ratio one. *J. Heat Trans.* **107**, 850-854.
- Brophy, C. P. 1990: Effect of intensity error correlation on the computed phase of phase-shifting interferometry. *J. Opt. Soc. Am. A* **7**, 537-541.

- Creath, K. 1988: Phase-measurement interferometry techniques. *Prog. Opt.* **26**, 349-393.
- Dändliker, R.; Thalmann, R.; Willemin, J. -F. 1982: Fringe interpolation by two-reference-beam holographic interferometry: reducing sensitivity to hologram misalignment. *Opt. Comm.* **42**, 301-306.
- Dändliker, R.; Thalmann, R. 1985: Heterodyne and quasi-heterodyne holographic interferometry. *Opt. Eng.* **24**, 824-831.
- Dudderar, T. D.; Simpkins, P. G. 1977: Laser speckle photography in a fluid medium. *Nature* **270**, 45-47.
- Figliola, R. S.; Beasley, D. E. 1995: *Theory and Design for Mechanical Measurements*. New York: John Wiley and Sons, 269-278.
- Fusegi, T.; Hyun, J. M.; Kuwahara, K. 1991: Transient three-dimensional natural convection in a differentially heated cubic enclosure. *Int. J. Heat Mass Trans.* **34**, 1559-1564.
- Gebhart, B.; Mahajan, R. L. 1982: Instability and transition in buoyancy induced flows. *Adv. Appl. Mech.* **22**, 231-315.
- Goodman, J. W. 1968: *Introduction to Fourier Optics*. New York: McGraw-Hill, 4-25, 90-96.
- Grousseau, R.; Mallick, S. 1977: Study of flow pattern in a fluid by scattered laser light. *Appl. Opt.* **16**, 2334-2336.
- Hall, J. D.; Bejan, A.; Chaddock, J. B. 1988: Transient natural convection in a rectangular enclosure with one heated side wall. *Int. J. Heat Fluid Flow* **9**, 396-404.
- Hamady, F. J.; Lloyd, J. R.; Yang, H. Q.; Yang, K. T. 1989: Study of local natural convection heat transfer in an inclined enclosure. *Int. J. Heat Mass Trans.* **32**, 1697-1708.
- Hariharan, P. 1985: Quasi-heterodyne holographic interferometry. *Opt. Eng.* **24**, 632-638.
- Hecht, E.; Zajac, A. 1974: *Optics*. Reading MA: Addison-Wesley, 109-116, 403-411.
- Hiller, W. J.; Koch, St.; Kowalewski, T. A.; Stella, F. 1993: Onset of natural convection in a cube. *Int. J. Heat Mass Trans.* **36**, 3251-3263.

- Holman, J. P. 1989: *Experimental Methods for Engineers*. New York: McGraw-Hill, 41-49.
- Hornung, H. G.; Willert, C.; Turner, S. 1995: The flow field downstream of a hydraulic jump. *J. Fluid Mech.* **287**, 299-316.
- Ivey, G. N. 1984: Experiments on transient natural convection in a cavity. *J. Fluid Mech.* **144**, 389-401.
- Jüptner, W.; Kreis, T. M.; Kreitlow, H. 1983: Automatic evaluation of holographic interferograms by reference beam phase shifting. In *Industrial Applications of Laser Technology* (ed. W. F. Fagan). *Proc. Soc. Photo-Opt. Instrum. Eng.* **398**, 22-29.
- Kreith, F.; Bohn, M. S. 1993: *Principles of Heat Transfer*. St. Paul: West, 119-148, 264-279.
- Kujawińska, M.; Robinson, D. W. 1988: Multichannel phase-stepped holographic interferometry. *Appl. Opt.* **27**, 312-320.
- Kujawińska, M.; Spik, A.; Robinson, D. W. 1989: Quantitative analysis of transient events by ESPI. In *Interferometry '89* (eds. Z. Jaroszewicz; M. Pluta). *Proc. Soc. Photo-Opt. Instrum. Eng.* **1121**, 416-423.
- Kuyper, R. A.; van der Meer, TH. H.; Hoogendoorn, C. J.; Henkes, R. A. W. M. 1993: Numerical study of laminar and turbulent natural convection in an inclined square cavity. *Int. J. Heat Mass Trans.* **36**, 2899-2911.
- Lanen, T. A. W. M.; Nebbeling, C.; van Ingen, J. L. 1990: Digital phase-stepping holographic interferometry in measuring 2-D density fields. *Exp. Fluids* **9**, 231-235.
- Lecordier, B.; Mouqallid, M.; Vottier, S.; Rouland, E.; Allano, D.; Trinite, M. 1994: CCD recording method for cross-correlation PIV development in unstationary high speed flow. *Exp. Fluids* **17**, 205-208.
- Lourenco, L.; Krothapalli, A. 1987: The role of photographic parameters in laser speckle or particle image displacement velocimetry. *Exp. Fluids* **5**, 29-32.
- Merzkirch, W. 1987: *Flow Visualization*. New York: Academic Press, 115-231.
- Papanicolaou, E.; Jaluria, Y. 1992: Transition to a periodic regime in mixed convection in a square cavity. *J. Fluid Mech.* **239**, 489-509.

- Patterson, J.; Imberger, J. 1980: Unsteady natural convection in a rectangular cavity. *J. Fluid Mech.* **100**, 65-86.
- Patterson, J. C.; Armfield, S. W. 1990: Transient features of natural convection in a cavity. *J. Fluid Mech.* **219**, 469-497.
- Powell, R. L. 1976: Thermocouple thermometry. In *Measurements in Heat Transfer* (eds. E. R. G. Eckert; R. Goldstein). New York: McGraw-Hill, 105-162.
- Raber, R. S. 1991: Electro-optic interferometry with noise tolerant phase unwrapping. M.S. Thesis, Department of Mechanical Engineering, The University of New Hampshire, Durham/NH.
- Schladow, S. G. 1990: Oscillatory motion in a side-heated cavity. *J. Fluid Mech.* **213**, 589-610.
- Schwider, J.; Burow, R.; Elssner, K. -E.; Grzanna, J.; Spolaczyk, R.; Merkel, K. 1983: Digital wave-front measuring interferometry: some systematic error sources. *Appl. Opt.* **22**, 3421-3432.
- Shough, D. M.; Kwon, O. Y. 1987: Phase-shifting pulsed-laser interferometer. In *Phase Conjugation, Beam Combining, and Diagnostics* (eds. I. Abramowitz; R. A. Fisher). *Proc. Soc. Photo-Opt. Instrum. Eng.* **739**, 174-180.
- Snyder, R. 1988: Instantaneous three-dimensional optical tomographic measurements of species concentration in a co-flowing jet. Ph.D. Thesis, Department of Aeronautics and Astronautics, Stanford University, Stanford/CA.
- Stetson, K. A.; Brohinsky, W. R.; Wahid, J.; Bushman, T. 1989: Electro-optic holography system with real-time arithmetic processing. *J. Nondestr. Eval.* **8**, 69-76.
- Takeda, M.; Ina, H.; Kobayashi, S. 1982: Fourier-transform method of fringe-pattern analysis for computer-based tomography and interferometry. *J. Opt. Soc. Am.* **72**, 156-160.
- van de Hulst, H. C. 1981: *Light Scattering by Small Particles*. New York: Dover, 28-36.
- Vest, C. M. 1979: *Holographic Interferometry*. New York: John Wiley and Sons, 264-284, 329-334, 396-413.
- Watt, D. W.; Vest, C. M. 1987: Digital interferometry for flow visualization. *Exp. Fluids* **5**, 401-406.

Willert, C. E.; Gharib, M. 1991: Digital particle image velocimetry. *Exp. Fluids* **10**, 181-193.

Winters, K. H. 1987: Hopf bifurcation in the double-glazing problem with conducting boundaries. *J. Heat Trans.* **109**, 894-898.

Yamane, T. 1967: *Statistics; An Introductory Analysis*. New York: Harper and Row, 339-344, 368-430.

Yih, C. -S. 1977: *Fluid Mechanics*. Ann Arbor: West River Press, 225-236.